

UNIVERSITY OF CALIFORNIA  
RIVERSIDE

Strongly Interacting Electrons and Holes in Ultrathin MoTe<sub>2</sub> Heterostructures

A Dissertation submitted in partial satisfaction  
of the requirements for the degree of

Doctor of Philosophy

in

Materials Science and Engineering

by

Dennis L. Pleskot

March 2019

Dissertation Committee:

Dr. Nathaniel Gabor, Chairperson

Dr. Jing Shi

Dr. Yongtao Cui

Copyright by  
Dennis L. Pleskot  
2019

The Dissertation of Dennis L. Pleskot is approved:

---

---

---

Committee Chairperson

University of California, Riverside

## ACKNOWLEDGMENTS

“And Frodo wouldn’t have got far without Sam, would he, dad?”

“Now, Mr. Frodo,” said Sam, “you shouldn’t make fun. I was serious.”

“So was I,” said Frodo, “and so I am.”

- J.R.R. Tolkien *The Two Towers*

Research is like a grand journey. There is a goal in mind, even if it’s only vaguely defined at first, and the path to that goal is long and arduous, filled with mountains to climb and valleys to traverse. There are difficulties and unexpected situations beset along the way. In some ways, PhD research is a microcosm for the journey of life itself. Yet like Frodo in J.R.R Tolkien’s classic *The Lord of the Rings*, I’ve been blessed with many Sam-like friends along the way, and here I get the chance to mention a few of them.

I want to thank my advisor, Nathaniel Gabor, for his instrumental guidance over my graduate career. He is both a sharply intelligent researcher as well as a down-to-earth normal guy that anyone would appreciate as a friend. These qualities are rare in academia, and rarer still is his insight into unique, challenging problems no one else in the field is thinking about as well as his ability to inspire students to pursue these hard problems for themselves. I also credit Nathan with elevating my standards for writing papers and visually presenting my work. It’s been a benefit to me in many areas of life. For this and everything else you did, Nathan, including welcoming me into the group in the first place after I switched over from another advisor, thank you so much.

There are many other colleagues and fellow graduate students who have walked this journey through graduate school with me, some of whom I had a chance raise up myself, but all of them ultimately had something to teach me. I thank Nate Gilgren, and Petr Stepanov for introducing me to the wild world of dry transfer of ultrathin semiconductors. Thank you Juan Aguilera Servin, Dexter Humphrey, and Dong Yan for mentoring me in cleanroom fabrication techniques. Special thanks to Yongtao Cui and Jing Shi, who served in my dissertation committee and provided significant support in this project. Warm thanks of course go to my fellow QMO lab members, who have provided support and fellowship over the years – Max Grossnickle, Fatemeh Barati, Jed Kistner-Morris, Jacky Wan, Dave Mayes, Farima Farahmand, and of course Trevor Arp, who has been my research colleague and has contributed substantially to the experimental findings of this dissertation.

I thank my family for all their support through all the ups and downs from childhood until now. Thank you Mom, Dad, and Kelly for always being there for me. Someone once said that home is the place where they have to let you in, and throughout my life, whether I was far or near, I always felt loved, accepted, and welcomed home by all of you. Thank you Aunt Diana, Uncle John, Kaitlin for your ever-present humor, love, and fellowship. Thank you Grandma White, Grandpa Nelson, and all my relatives who have passed on from this world. Your presence in my life has been so supportive and encouraging. And to my wife Bernice, thank you for your continued love and commitment to me that I see on display every day I come home from the lab. You are

my confidant, my suitable helper, and I look forward eagerly to the future we have in store together.

In addition to these, my church family has been one of the biggest sources of strength for me these past several years here in Riverside. Thank you Pastor Steve, Pastor Manny, Jammy Yang, Richard Tay, and Abe Yang for being spiritual mentors to me throughout my years in graduate school. Without you, I would have lost sight of what's truly important so many times. You've helped shape me and guide me so much in my larger journey of following Christ, of which graduate school has been a part. Thank you so much for all you've done. I thank my church friends - James Hong, Victor Shia, Ken Yun, and Neil Wang. Thank you all for the fun times, living life together, and your fellowship. Thank you Howard Noz, my closest friend, who has often been a lifeline to me these past 9 years. If anyone has been a Sam-like friend to me in my life, it's you. Thank you Peter Daniel, Tom Chen, David Schiefelbein, Dave Patel, William Sio, and all the rest of your class for allowing me to mentor you during your college days. The same goes for current UCR seniors Peter Tan, Allen Partono, Jeffrey Lee, Marvin De La Cruz, Sam Khong, Jacky Xue, and Ian Bonafede. I hope you will all join me in graduating this year. And thank you to everyone else at church. I will miss you all dearly as I move to North Carolina.

The text of this dissertation, in part, is a reprint of the material as it appears in Nature Photonics (published online on 2/4/2019). The co-author, Nathaniel Gabor, listed in that publication directed and supervised the research which forms the basis for this dissertation. Trevor Arp, another co-author, conducted photoresponse imaging

measurements in this work, while Vivek Aji supported the direction and interpretation of the experiments through theoretical understanding of the data. In this work, we received financial support from the Air Force Office of Scientific Research Young Investigator Program (YIP), U.S. Department of Energy, the National Science Foundation, and the Canadian Institute for Advanced Research (CIFAR).

To my friends, family, and to my wife Bernice

## ABSTRACT OF THE DISSERTATION

Strongly Interacting Electrons and Holes in Ultrathin MoTe<sub>2</sub> Heterostructures

by

Dennis L. Pleskot

Doctor of Philosophy, Graduate Program in Materials Science and Engineering  
University of California, Riverside, March 2019  
Dr. Nathaniel Gabor, Chairperson

Heterostructures composed of atomic layer materials (ALMs) bonded through van der Waals (vdW) interactions have demonstrated great potential for use in next generation optoelectronic devices. However, the role of strong charge carrier interactions in the interlayer photocurrent in such devices is not fully understood. One such ALM, molybdenum ditelluride (MoTe<sub>2</sub>), has a band gap energy near 1.0 eV, suggesting that MoTe<sub>2</sub> is a promising material for ultrasensitive infrared optical photodetectors and next-generation solar photocells. Like other ALMs, the photoresponse in MoTe<sub>2</sub> should give experimental access to strong many-body phenomena. Here, we report on the advanced fabrication and dynamic photoresponse of graphene-MoTe<sub>2</sub>-graphene vdW heterostructure photocells. We find that the power dependence of the interlayer photocurrent is well described by a single power law at low power, where the power law exponent parameterizes the nonlinearity of the photoresponse. We develop a detailed 2-particle Auger recombination model that accounts for careful time integration of the dynamics, resulting in an analytic solution that reproduces the non-linear power

dependence. Additionally, we observed sharp suppression of conventional power law behavior above a critical power threshold, accompanied with a critical phase transition in the spatial expansion of the suppressed photocurrent region. We attribute this transition to the emergence of an electron-hole liquid phase that is remarkably stable at room temperature and moderate operating conditions. Additional measurements of the dynamic photoresponse support the existence of this phase, allowing us to fully explore the evolution of electron-hole pairs with increasing density in MoTe<sub>2</sub>.

## TABLE OF CONTENTS

Acknowledgements	iv
Dedication	viii
Abstract	ix
Forward	xv
Quantum Confinement: There's Not So Much Room at the Bottom	1
Chapter 1: Excitons in the 2-Dimensional Limit	
1.1 Introduction	4
1.2 Excitons and Exciton Gases in Atomic Layer Materials	4
1.3 Exciton-Exciton Interactions in Atomic Layer Materials	8
1.4 Many-Body Interactions in Atomic Layer Materials	12
1.5 The Electron-Hole Liquid	17
1.6 Conclusion	21
Chapter 2: Properties of Ultrathin MoTe <sub>2</sub> Heterostructures	
2.1 Introduction	22
2.2 MoTe <sub>2</sub> Lattice Structure	22
2.3 Electronic Band Structure of MoTe <sub>2</sub>	23
2.4 Charge Carrier Lifetime in MoTe <sub>2</sub>	27
2.5 Van der Waals Heterostructures	29
2.6 Conclusion	33
Chapter 3: Device Fabrication and Measurement	
3.1 Introduction: Device Design	35
3.2 Wafer Preparation	37
3.3 Exfoliation of Atomic Layer Materials	39
3.3.1 Exfoliation: Standard Method	41
3.3.2 Exfoliation: Razor Method	43
3.3.3 Exfoliation: Low Angle Method	45
3.3.4 Exfoliation: Gold Assisted Method	47
3.4 Building a Heterostructure: Dry Transfer Technique	49
3.4.1 Dry Transfer: Standard Method	52
3.4.2 Dry Transfer: Direct Stamp Exfoliation Method	55
3.5 Device Fabrication	56
3.5.1 Standard Fabrication Method	58

3.5.2	Contact Pre-Write Fabrication Method	64
3.6	Chip Carrier Fabrication	65
3.7	Optoelectronic Measurements	67
3.8	Conclusion	69
Chapter 4: Basic Characterization of MoTe <sub>2</sub> Photocells		
4.1	Introduction	71
4.2	Atomic Force Microscopy (AFM)	71
4.3	Raman Spectroscopy	73
4.4	Power Dependent I-V Measurements	75
4.5	Temperature and Wavelength Dependent I-V Measurements	77
4.6	Conclusion	79
Chapter 5: Auger Recombination in the Extreme Electron-Hole Density Limit of a MoTe <sub>2</sub> Photocell		
5.1	Introduction	80
5.2	One-Pulse Measurement: Power Dependence	82
5.3	Two-Pulse Measurement: Temporal Dependence	83
5.4	Model: 2-Particle Auger Recombination	85
5.5	Testing the Model: Bias Dependent Measurements	89
5.6	Conclusion	92
Chapter 6: 2D Condensate of Electrons and Holes in Ultrathin MoTe <sub>2</sub> Photocells		
6.1	Introduction	94
6.2	Multi-Parameter Photocurrent Imaging	95
6.3	Critical Onset of Ring-Like Photoresponse	98
6.4	Model: 2D Electron-Hole Condensate	100
6.5	Evidence for the 2D Condensate	102
6.6	Conclusion	107
Chapter 7: Conclusion		108
References		109

## LIST OF FIGURES

### **Quantum Confinement: There's Not So Much Room at the Bottom**

Figure 0.1	Density of states for increasing quantum confinement	2
Figure 0.2	Examples of 2D materials for investigation	2

### **Chapter 1**

Figure 1.1	Schematic of an exciton and surrounding electric field lines	5
Figure 1.2	Schematic of an exciton in 3D vs. 2D dielectric environments	5
Figure 1.3	Thickness-dependent PL of a terraced MoS <sub>2</sub> flake	7
Figure 1.4	Power-dependent photocurrent in graphene-WSe <sub>2</sub> -graphene	7
Figure 1.5	PL absorbance and exciton dynamics vs. pump fluence	8
Figure 1.6	PL of monolayer MoTe <sub>2</sub>	10
Figure 1.7	Optical absorption of bilayer WS <sub>2</sub> at high carrier density	13
Figure 1.8	Ultrafast reflectance spectroscopy/model of monolayer MoS <sub>2</sub>	15
Figure 1.9	PL spectrum of bulk Ge	18
Figure 1.10	Schematic of an electron-hole liquid	19

### **Chapter 2**

Figure 2.1	Crystal structure of hexagonal MoTe <sub>2</sub>	23
Figure 2.2	PL spectra of MoTe <sub>2</sub> for various layer thicknesses	24
Figure 2.3	Electronic band structure of MoTe <sub>2</sub>	24
Figure 2.4	Spin-orbit coupling in MoTe <sub>2</sub>	25
Figure 2.5	Photocurrent vs. time delay in graphene-WSe <sub>2</sub> -graphene	27
Figure 2.6	Photocurrent vs. time delay in graphene-MoTe <sub>2</sub> -graphene	29
Figure 2.7	Schematic of van der Waals heterostructure assembly	30
Figure 2.8	Graphene-hBN van der Waals heterostructure	31
Figure 2.9	Graphene-MoTe <sub>2</sub> -graphene photodetector	32

### **Chapter 3**

Figure 3.1	Schematic of graphene-MoTe <sub>2</sub> -graphene photocell	35
Figure 3.2	Si wafer preparation	37
Figure 3.3	Exfoliation equipment	39
Figure 3.4	Optical images of each heterostructure layer	40
Figure 3.5	Exfoliation equipment: standard method	41

Figure 3.6	Exfoliation equipment: razor method	43
Figure 3.7	Exfoliation equipment: low angle method	45
Figure 3.8	Exfoliation equipment: gold assisted method	47
Figure 3.9	Optical image of dry transfer microscope	49
Figure 3.10	Optical image of a graphene-MoTe <sub>2</sub> -graphene heterostructure	51
Figure 3.11	Schematic of dry transfer process	52
Figure 3.12	Equipment for device fabrication	57
Figure 3.13	Optical image of a graphene-MoTe <sub>2</sub> -graphene photocell	57
Figure 3.14	Chip carrier fabrication	66
Figure 3.15	Schematic of ultrafast measurement apparatus	67
<b>Chapter 4</b>		
Figure 4.1	AFM of a graphene-MoTe <sub>2</sub> -graphene photocell	72
Figure 4.2	Raman spectroscopy of a graphene-MoTe <sub>2</sub> -graphene photocell	74
Figure 4.3	<i>I-V</i> characteristics of a graphene-MoTe <sub>2</sub> -graphene photocell	76
Figure 4.4	Temperature and wavelength dependent <i>I-V</i> characteristics	77
<b>Chapter 5</b>		
Figure 5.1	One-pulse photocurrent vs. optical power measurement	82
Figure 5.2	Dynamic photoresponse measurements of the vdW photocell	84
Figure 5.3	2-particle Auger recombination model	86
Figure 5.4	Interlayer voltage control of Auger recombination	90
<b>Chapter 6</b>		
Figure 6.1	Spatial photocurrent maps for increasing laser power	95
Figure 6.2	Spatial maps of $\gamma(x, y)$ as a function of $\Delta t$	96
Figure 6.3	Critical onset of ring-like photoresponse	99
Figure 6.4	Evolution of <i>e-h</i> interactions with increasing carrier density	101
Figure 6.5	Schematic energy diagram for photoexcited carriers in MoTe <sub>2</sub>	101
Figure 6.6	Comparison of 2D electron-hole liquid model to experiment	103
Figure 6.7	Interlayer voltage dependence of the 2D electron-hole liquid	104
Figure 6.8	Dynamic photoresponse of the 2D electron-hole liquid	106

## FORWARD: ABOUT THE AUTHOR

“Still round the corner there may wait

A new road or a secret gate

And though I oft have passed them by

A day will come at last when I

Shall take the hidden paths that run

West of the Moon, East of the Sun.”

- J.R.R. Tolkien *The Return of the King*

Dennis L. Pleskot was born in Brea, California but ultimately raised in the quiet, sheltered suburb of Yorba Linda. From his father, Larry, he gained early on a love for the natural world, the physics that undergirds it as well as the way humans engineer things out of it. Growing up, there were also many other interests in Dennis’ life, chief among these being outdoor activities such as running and playing tennis, as well as more contemplative pastimes such as reading numerous science fiction and fantasy novels.

Dennis’ passion for academic studies grew into full form in high school. He found interest not only in the physical sciences but also in literature, history, and even art. All of these academic interests took up a significant portion of his time and efforts. Outside of his intense curiosity for learning as much as he could about the world around him, Dennis also furthered his interests in running by joining the cross-country team, where he would learn the value of persevering through short term pain in order to invest

in long term goals, a mentality that would serve him well in the future, particularly in graduate school.

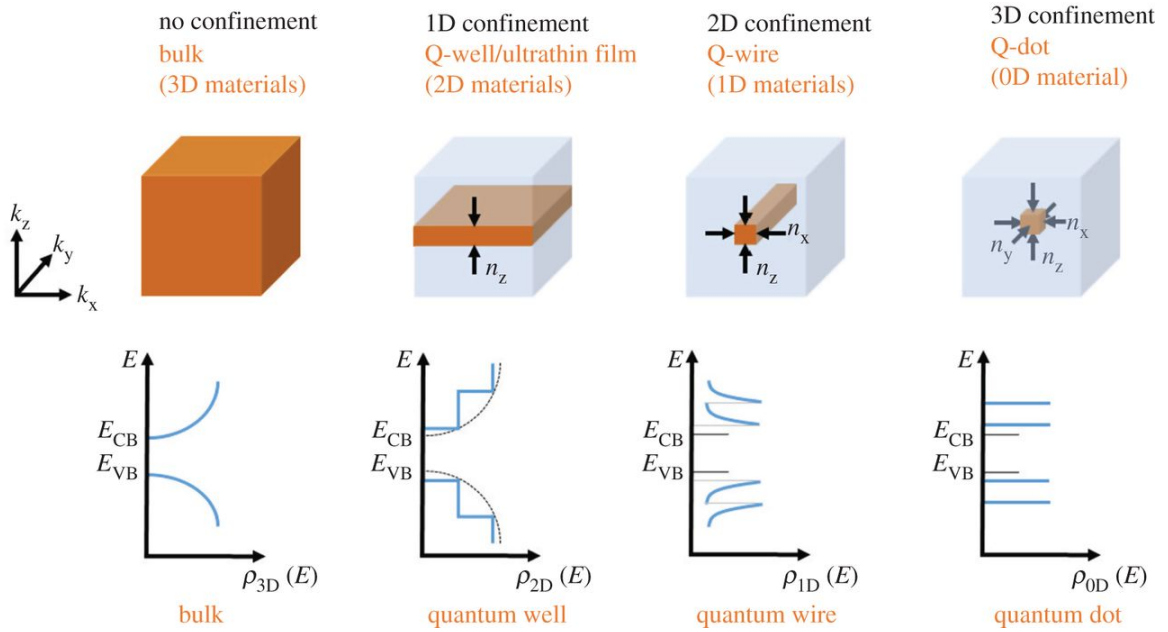
During his time in college at UC Berkeley as well as his graduate studies in both the Masters and PhD program at UC Riverside, Dennis grew to become a full-fledged scientist. However, there was a deeper longing developing in him at the same time. In light of the evidence around him both in the sciences and without, he was not satisfied with the view that this world is solely material. Through his own investigations and his emerging relationships in a vibrant church, Dennis became convinced that there must be a higher power at work in this world. He had become a Christian. And far from weakening his abilities and love of science, this identity brought a far deeper appreciation for his studies and his research, as it continues to do today.

QUANTUM CONFINEMENT:  
THERE'S NOT SO MUCH ROOM AT THE BOTTOM

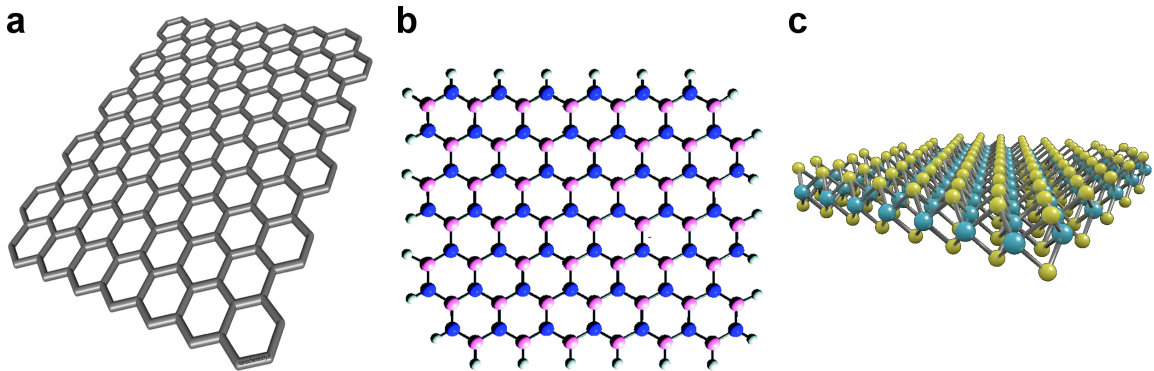
Electricity, the motive force of our modern society, fuels everything from street lamps to phones, and the demand for more versatile and numerous consumer electronics shows no signs of slowing down in the near or far future. The behavior of charge carriers (electrons and holes), the constituent elements of electricity, are therefore of paramount interest to scientists and engineers. In particular, the ability to generate high densities of electrons and holes can potentially lead to a number of novel physical phenomena, opening up the possibilities for next-generation electronic devices. These highly interacting systems of electrons and holes can be best achieved through the process of quantum confinement, in which electronic materials are thinned down to the nanoscale, forcing electrons and holes into higher densities.

Figure 0.1 describes the effects of quantum confinement on the density of states of a material<sup>1</sup>. In the bulk, the parabolic energy dispersion of a typical semiconducting band displays a continuous increase of the density of states that scales as the square root of energy. In the 2D case, the density of states transforms into a step function bounded by the 3D density of states. For 1D materials, the density of states features a series of singular points (called van Hove singularities), while at the limit of 0D structures, these features become discrete, narrow bands. Atomically thin, 2D materials display significant quantum confinement while also containing enough states to generate substantial populations of electrons and holes, making them ideal for creating and

exploring the effects of high charge carrier densities. A wide variety of 2D materials



**Figure 0.1:** Schematic of physical form and density of states for increasing quantum confinement. Adapted from Edvinsson<sup>1</sup>.



**Figure 0.2:** Examples of 2D materials for investigation. **(a)** Atomic structure of graphene, **(b)** hexagonal boron nitride (hBN), and **(c)** a transition metal dichalcogenide.

have been discovered, including graphene, hBN, and transition metal dichalcogenides (TMDs) (Figure 0.2). Thus, a nearly limitless array of structures can be envisioned for examining highly interacting electrons and holes.

In the remainder of this dissertation, we present novel 2D structures and optoelectronic measurements that reveal unique and striking charge carrier interactions. We describe a TMD-based optoelectronic device where we observe highly dominant 2-body Auger recombination that precedes the formation of a room temperature electron-hole liquid as the density of carriers increases. Chapter 1 reviews the evolution of highly interacting electrons and holes in 2D materials, providing suitable background information for our investigation. In Chapter 2, we establish MoTe<sub>2</sub> as the TMD material of choice for the proposed device and highlight the advantages of vdW heterostructures for examining highly interacting charge carriers. Chapter 3 provides details on the fabrication of the specific devices studied in this dissertation and briefly reviews the experimental measurement apparatus. In Chapter 4, we examine standard material and electronic characterization data for these devices. Chapters 5 and 6 present the main optoelectronic measurements and experimental results, providing novel insight into electron-hole interactions in TMD-based optoelectronic devices.

## CHAPTER 1

### EXCITONS IN THE 2-DIMENSIONAL LIMIT

#### *1.1 Introduction*

In this chapter, we review the existing framework on electron-hole interactions in 2D materials, highlighting significant phenomena. We show that photoexcited charge carriers quickly form into excitons in these materials, and that an exciton gas phase is rapidly established. At higher densities, excitons have been shown to interact with each other through processes such as exciton-exciton annihilation. Furthermore, at still higher densities, giant bandgap renormalization has been observed, revealing the presence of many-body effects. At the limits of excitonic densities, an electron-hole liquid droplet phase has been observed in traditional bulk semiconductor materials, such as Ge, yet has never been detected in 2D materials. Though the electron-hole liquid has only been observed at liquid He temperatures, we discuss how 2D materials offer the possibility of generating this phase at substantially higher temperature due to their increased quantum confinement and resulting electron-hole interaction strength.

#### *1.2 Excitons and Exciton Gases in Atomic Layer Materials*

A single excited electron-hole pair generated in a semiconductor can form into a complex quasiparticle known as an exciton, as shown in Figure 1.1. Electrons and holes in this state are bound together by Coulomb interactions, and the amount of energy

needed to separate them from this state is known as the exciton binding energy. Excitons in 2D materials exhibit unusually large binding energies, due not only to increased

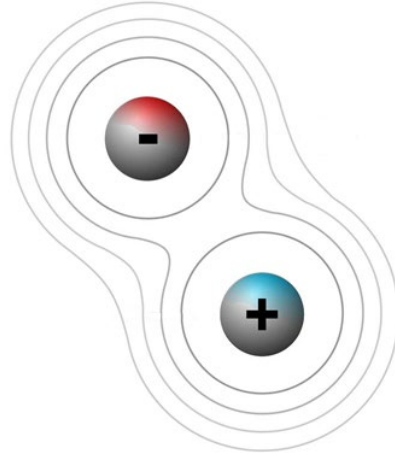


**Figure 1.1:** Schematic of an exciton containing a single electron and hole, with electric field lines extending from each.

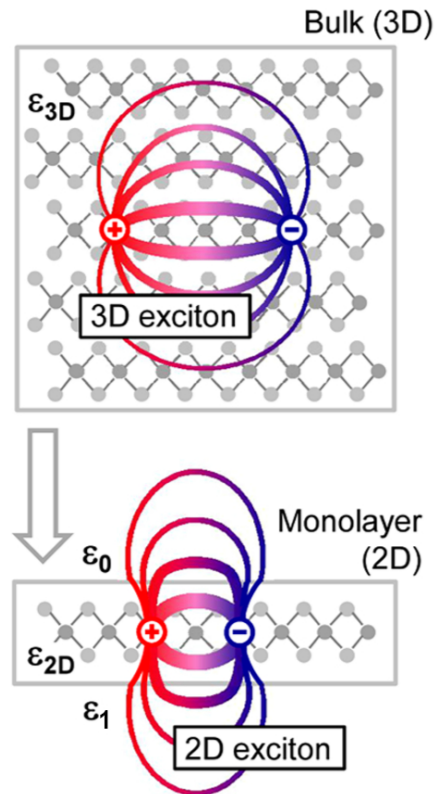


**Figure 1.2:** Schematic of an exciton and associated electric field lines in a bulk 3D material compared to a 2D monolayer.  $\epsilon_{3D}$  is the bulk dielectric constant, whereas  $\epsilon_{2D}$  is the 2D dielectric constant.  $\epsilon_0$  and  $\epsilon_1$  are dielectric constants of a surrounding vacuum medium and underlying substrate, respectively. Adapted from Chernikov *et al.*<sup>2</sup>. quantum confinement of the carriers but also to a sensitive dependence of the binding energy on dielectric environment<sup>2</sup>. Figure 1.2 illustrates the difference between electric field lines emanating from an exciton in a 3D bulk material compared to a 2D material. In the 2D case, electric field lines extend outside the material that contains the exciton, leading to a slight distortion of the field lines and an enhancement of the binding energy. If we assume a 2D material with a dielectric  $\epsilon_{2D}$  on a substrate with dielectric  $\epsilon_1$  and surrounded by a vacuum with permittivity  $\epsilon_0$ , the binding energy  $E$  as a function of material thickness can be expressed as

$$E \approx - \frac{e^2}{\epsilon_{2D}d} \ln \left[ \left( \frac{2\epsilon_{2D}}{\epsilon_0 + \epsilon_1} \right)^2 \frac{d}{a_0} \right] \quad (1)$$

where  $e$  is the charge of an electron,  $d$  is the thickness of the material containing the exciton, and  $a_0$  is the exciton radius in the bulk 3D material<sup>3</sup>. From this expression, the binding energy clearly increases with decreasing material thickness, indicating that excitons should be very strongly bound in ultrathin 2D materials.

In many atomically thin materials, excitons also form in a fast and efficient manner. Splendiani *et al.* showed that few-layer MoS<sub>2</sub>, a TMD, exhibits significant photoluminescence at the absorption peaks of the A1 (670 nm) and B1 (627 nm) direct excitons<sup>4</sup> (Figure 1.3). Figure 1.3a shows the raw photoluminescence data while Figure 1.3b displays the same data normalized by the Raman intensity to approximate the photoluminescence efficiency as a function of material thickness. As the material

approaches the monolayer limit, the photoluminescence intensity of the direct excitons grows dramatically, indicating rapid exciton formation in TMDs.

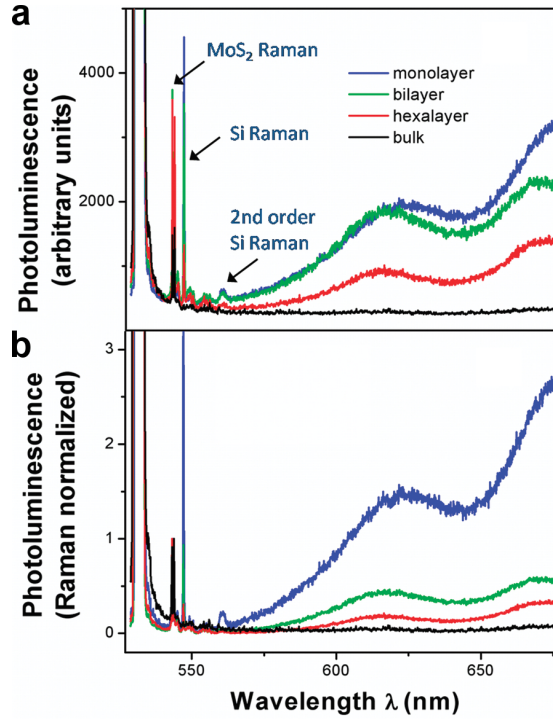


**Figure 1.3:** Thickness-dependent photoluminescence of a terraced MoS<sub>2</sub> flake. **(a)** Raw photoluminescence data. **(b)** Photoluminescence efficiency determined by normalizing the raw photoluminescence data in **(a)** with the Raman intensity. Adapted from Splendiani *et al.*<sup>4</sup>.

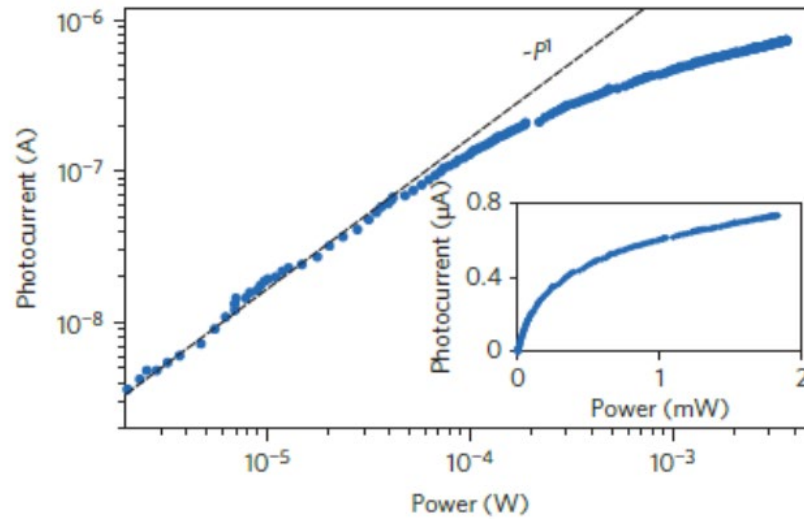


**Figure 1.4:** Power dependence of the interlayer photocurrent in a graphene-WSe<sub>2</sub>-graphene heterostructure. Dashed line indicates linear relationship. Inset, same power dependence data presented on a linear scale. Adapted from Massicotte *et al.*<sup>5</sup>.

The efficient binding of free electrons and holes into excitons in TMDs gives rise to the prevalence of exciton gases in these materials. Massicotte *et al.* examined the power dependence of the interlayer photocurrent in a graphene-WSe<sub>2</sub>-graphene van der Waals heterostructure, as shown in Figure 1.4<sup>5</sup>. For very low values of laser power, on the order of fractions of mW, the photocurrent increases linearly with respect to power, suggesting the presence of a monotonically increasing population of excitons. At higher power, on the order of mW, the power dependence begins to deviate from this linear behavior, indicating that other physical phenomena may emerge as higher power is applied.

### ***1.3 Exciton-Exciton Interactions in Atomic Layer Materials***

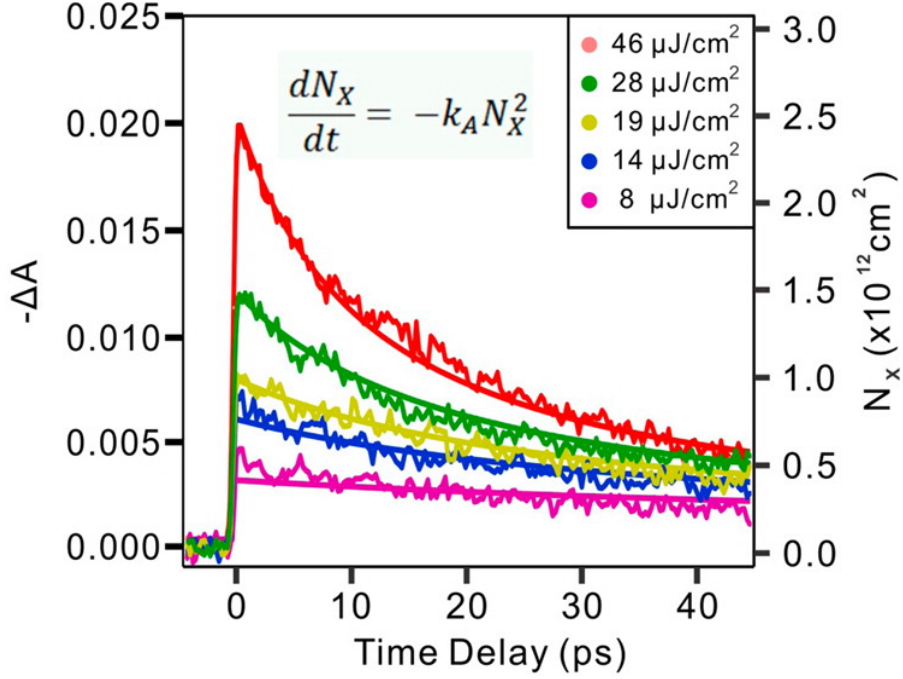


**Figure 1.5:** Change in photoluminescence absorbance and exciton dynamics for various pump fluences. Solid lines represent fits to the raw data (jagged lines) according to top equation, also Equation (1) below. The right axis denotes the scale of photoexcited excitons derived from the model. Adapted from Sun *et al.*<sup>6</sup>.

Along with fast and efficiently forming excitons in TMD materials, exciton-exciton interactions have also been observed as the density of charge carriers increases. Sun *et al.* investigated the photoluminescence absorption of monolayer MoS<sub>2</sub> samples and observed clear exciton-exciton annihilation processes<sup>6</sup>. Their results are summarized in Figure 1.5, where they measure the change in photoluminescence absorption  $\Delta A$  as a function of time delay between pulses in an ultrafast supercontinuum laser. They observed that the raw data exhibits a nearly quadratic decay profile, suggesting the possibility of a 4-body exciton-exciton extinction process. From this, they developed a simple exciton-exciton annihilation model that can be expressed as

$$\frac{dN_x}{dt} = -k_A N_x^2 \quad (2)$$

where  $N_x$  refers to the number of excitons and  $k_A$  represents the rate constant for exciton-exciton annihilation. Solid line fits of this expression to the absorbance profiles are shown in Figure 1.5, displaying good agreement with the experimental data across a wide range of pump fluences. As pump fluence, and hence the density of carriers, increases in the system, the decay behavior becomes increasingly quadratic and better fitted to the model, indicating that exciton-exciton annihilation dominates the physics of photoexcited carriers in TMDs as carrier density is increased through external excitation.

Exciton-exciton interactions have not only been seen in monolayer MoS<sub>2</sub> but also in ultrathin MoTe<sub>2</sub>. Froehlicher *et al.* utilized photoluminescence measurements of MoTe<sub>2</sub> samples to investigate the transition from indirect to direct band gap emission as MoTe<sub>2</sub> is thinned down to the monolayer<sup>7</sup>. They confirmed that monolayer MoTe<sub>2</sub> exhibits substantial PL intensity, and they measured the effect of varying the exciton formation rate,  $W_{\text{abs}}$ , on this strong intensity. The formation rate was estimated by factoring in the size of the laser spot incident to the sample, the absorbance of MoTe<sub>2</sub>, and optical coherence effects. Formation rates are therefore proportional to the laser intensity and were determined to be in the range of  $W_{\text{abs}} \approx 10^{19} - 10^{22} \text{ cm}^{-2} \text{ s}^{-1}$ .

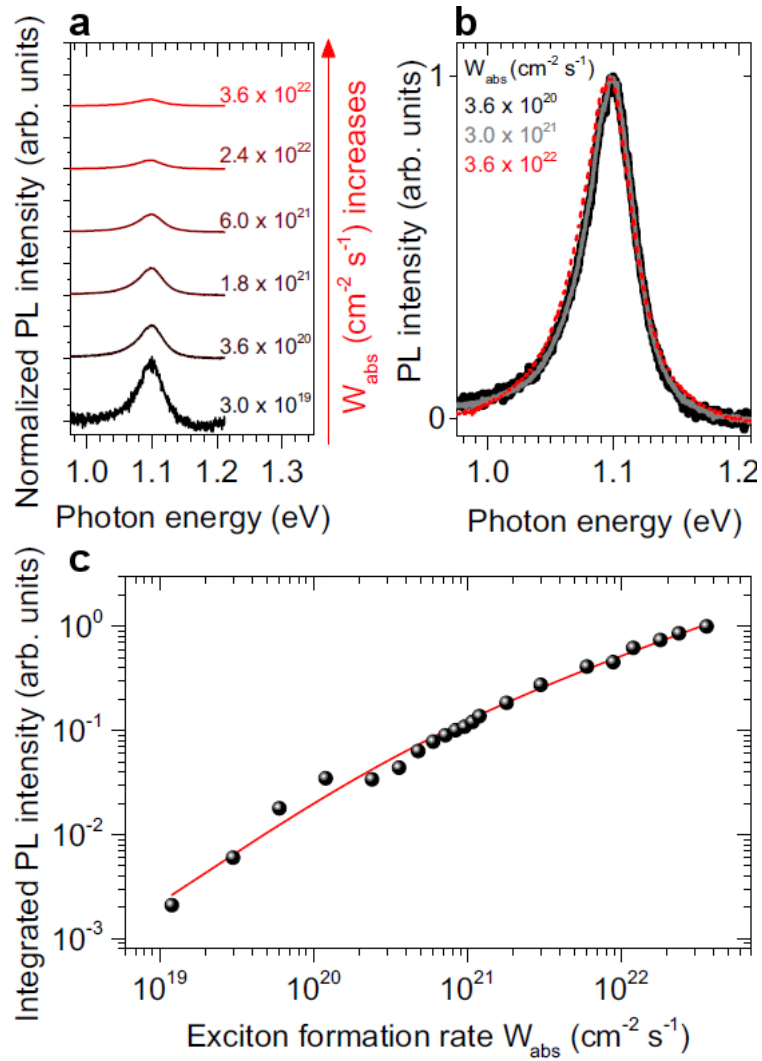


**Figure 1.6:** Photoluminescence of monolayer MoTe<sub>2</sub>. **(a)** MoTe<sub>2</sub> PL for increasing exciton formation rate,  $W_{\text{abs}}$  and also normalized by  $W_{\text{abs}}$ . **(b)** MoTe<sub>2</sub> PL for various exciton formation rates, normalized to unity. **(c)** Integrated MoTe<sub>2</sub> PL as a function of exciton formation rate (black circles). Red solid line indicates fit of exciton-exciton annihilation model to the data. Adapted from Froehlicher *et al.*<sup>7</sup>.

Figure 1.6a displays the PL spectra normalized by  $W_{\text{abs}}$  for a monolayer MoTe<sub>2</sub> sample taken at various exciton formation rates. The normalized PL intensity clearly dissipates as the formation rate is increased. Measuring the PL as a function of  $W_{\text{abs}}$  in Figure 1.6c reveals that the raw PL data begins to saturate at high values of exciton

formation rate. At the same time, Figure 1.6b, which displays the PL spectra normalized to unity, indicates that the linewidth of the PL peak is essentially independent of  $W_{\text{abs}}$ .

Curiously, this sublinear dependence could well be related to the similar phenomenon seen by Massicotte *et al.*<sup>5</sup> in Figure 1.4. Froehlicher *et al.*, however, proposed that this sublinear dependence, where the linewidth is invariant, is due to exciton-exciton annihilation. As with Sun *et al.* above, they suggested a simple rate equation to explain the exciton dynamics

$$\frac{dn_x}{dt} = W_{\text{abs}} - \Gamma_x n_x - \gamma_{\text{eea}} n_x^2 \quad (3)$$

where  $n_x$  is the steady state exciton density,  $\Gamma_x$  is the rate of exciton recombination, and  $\gamma_{\text{eea}}$  is the exciton-exciton annihilation rate, which scales with  $n_x^2$  due to the interaction of two excitons. By solving Equation (3) above for the expected steady state exciton density, they obtained

$$n_x = \frac{\Gamma_x}{2\gamma_{\text{eea}}} \left( \sqrt{1 + \frac{4\gamma_{\text{eea}}}{\Gamma_x^2} W_{\text{abs}}} - 1 \right) \quad (4)$$

This expression was used to fit the data in Figure 1.6c by relating  $n_x$  to the integrated PL intensity, and the result is depicted in the solid red line. The fit agrees well with the data, indicating that exciton-exciton annihilation accurately describes the sublinear PL response.

Along with these works, exciton-exciton interactions have also been observed in a number of other recent studies. Mouri *et al.*<sup>8</sup> observed exciton-exciton annihilation assisted through diffusion processes in ultrathin WSe<sub>2</sub>, while Kumar *et al.*<sup>9</sup> reported

exciton-exciton annihilation in monolayers of MoSe<sub>2</sub>. Additionally, Yu *et al.*<sup>10</sup> probed the limits of exciton-exciton annihilation in atomically thin MoS<sub>2</sub> and WS<sub>2</sub>, and Surrente *et al.*<sup>11</sup> discovered the onset of exciton-exciton annihilation in monolayer black phosphorus. Kulig *et al.*<sup>12</sup> observed other exciton-exciton interaction effects. In particular, they evinced the role of Auger recombination in the diffusion of excitons in monolayer WS<sub>2</sub>. In short, exciton-exciton interactions play a significant role in the optoelectronic response of ultrathin TMD materials yet most evidence is based on purely optical measurement techniques.

#### ***1.4 Many-Body Interactions in Atomic Layer Materials***

At very high charge carrier densities, evidence suggests that photoexcited excitons in TMDs can coalesce into a many-body system of highly interacting electrons and holes, though the details of this many-body system remain unclear. Chernikov *et al.* examined bilayer WS<sub>2</sub> under ultrafast optical pump-probe excitation<sup>13</sup>. They utilized high laser fluences up to several mJ cm<sup>-2</sup> to induce a Mott transition from an insulating excitonic regime to a dense, many-body electron-hole plasma. In Figure 1.7b, the reflectance contrast between the WS<sub>2</sub> flake and the substrate,  $R_c$ , is measured as a function of laser energy. They measured the reflectance both with (light red data) and

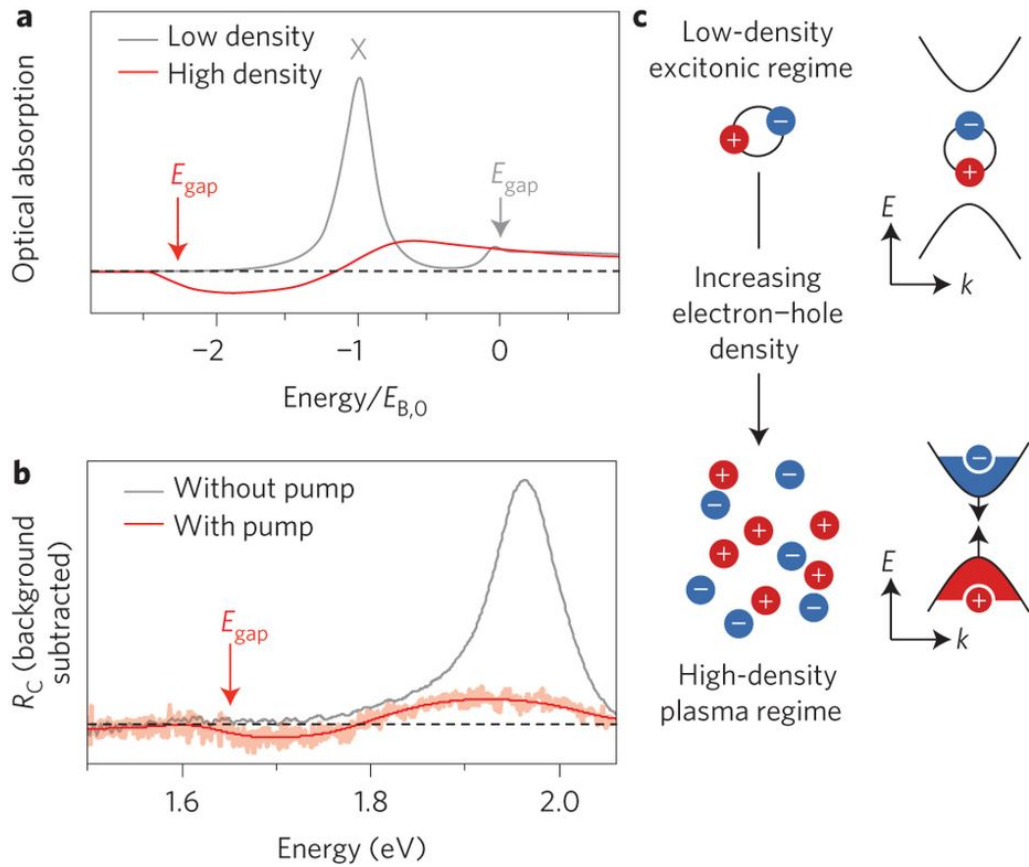


**Figure 1.7:** Optical absorption of bilayer WS<sub>2</sub> at high charge carrier density. **(a)** Predicted absorption vs. energy of an ultrathin TMD derived from many-body theory, where energy is normalized by the exciton binding energy  $E_{B,0}$ . Grey line indicates the predicted absorption at low electron-hole density while the red line represents the predicted absorption at high electron-hole densities.  $E_{gap}$  reflects the renormalized band gap at high carrier densities. **(b)** Experimental reflection contrast between sample and substrate vs. laser energy, with background response subtracted out from the data. Grey line indicates reflectance without pump pulse while light red data represents reflectance with pump pulse. Solid red line is a guide to the eye for the reflectance data in light red, determined by a smoothing function.  $E_{gap}$  denotes the renormalized band gap position. **(c)** Schematic of transition from a low-density excitonic regime to a high-density plasma. Adapted from Chernikov *et al.*<sup>13</sup>.

without (grey line) the pump pulse, with a linear background response subtracted out from the data. They observed the characteristic strong A exciton absorption peak just below 2.0 eV. However, when the pump pulse is turned on, the exciton peak vanishes

and a dip in the reflectance at a lower energy of about 1.6 eV appears. The solid red line in Figure 1.7b is a guide to the eye that helps visualize the trend in the actual data (light red).

In order to understand this change in reflectance, calculations based on many-body theory in 2D materials were performed (Figure 1.7a). At low charge carrier densities (grey line in Figure 1.7a), the carriers are excitonic in nature, and the primary absorption peaks occur at the exciton absorption and at the band gap. However, at high charge carrier densities (red line in Figure 1.7a), screening effects become prominent, and the Coulomb interaction between carriers is reduced. With enough screening, a Mott transition from an excitonic regime to an electron-hole plasma can be induced. Excitons are thus no longer bound, leading to a disappearance of the excitonic peak. At the same time, the quasi-particle energy of the carriers becomes reduced, lowering the band gap energy. This band gap renormalization is denoted by  $E_{\text{gap}}$  in Figure 1.7a. The calculated absorbance spectra for high-density and low-density electron-hole pairs agree qualitatively with the experimental reflectance with and without the pump pulse, respectively. Accordingly, a many-body electron-hole plasma emerges from typical excitonic behavior in bilayer WS<sub>2</sub> at high charge carrier densities, as shown schematically in Figure 1.7c.

Additionally, other measurements of unusual behavior at high pump fluence have been attributed to many-body states in other TMD materials. Aivazian *et al.* utilized ultrafast degenerate pump-probe spectroscopy in order to investigate optically inactive

states in monolayer WSe<sub>2</sub><sup>14</sup>. They measured the reflectance spectrum of the sample for various time delays (Figure 1.8a), and they observed a clear peak at the primary A

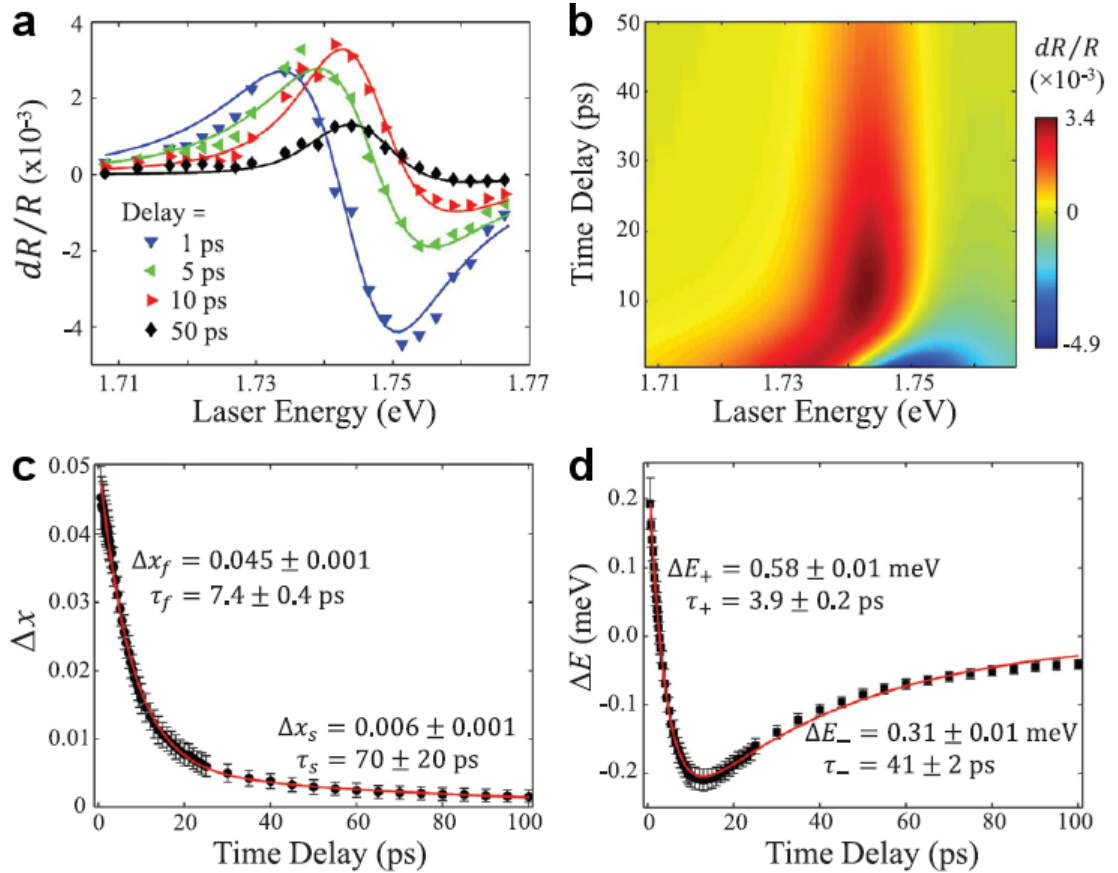


**Figure 1.8:** Ultrafast reflectance spectroscopy and exciton optical susceptibility model of monolayer WSe<sub>2</sub>. **(a)** Experimental  $dR/R$  spectra (symbols) for various time delays. Solid lines represent fits of model derived from Equation (4) to data. **(b)** Calculated  $dR/R$  from the model as a function of both time delay and laser energy. **(c)** and **(d)** are plots of fit parameters  $\Delta x$  and  $\Delta E$  from the model (symbols) as a function of time delay, respectively. Solid red lines indicate biexponential fits according to Equation (5). Adapted from Aivazian *et al.*<sup>14</sup>.

exciton absorption band of  $E_0 = 1.745$  eV, revealing the predominance of excitonic species once again in TMDs. At short time delays, the excitonic peak is antisymmetric, yet as time delay increases, the negative side of the peak diminishes, leaving behind only

a symmetric positive peak. Also, the excitonic peak experiences a clear blue shift with increasing time delay as well.

These observations rule out any influence from photo-induced bleaching, since such bleaching would not result in a resonance shift or transformation of the peak from an antisymmetric to a symmetric shape. Instead, the authors proposed an exciton optical susceptibility model which can be represented as

$$\Delta\chi(\omega, \tau) = \frac{1 - L(\omega)\Delta\chi(\tau)}{\omega - E_0 - L(\omega)\Delta E(\tau) + i\gamma} - \chi_0 \quad (5)$$

where  $\Delta\chi(\omega, \tau)$  is the exciton optical susceptibility,  $\omega$  is the laser energy,  $\tau$  is the time delay,  $\chi_0$  is the susceptibility when the pump pulse is blocked,  $\Delta\chi(\tau)$  is the oscillator strength reduction,  $\Delta E(\tau)$  is the exciton resonance shift, and  $\gamma$  is the resonance width. A standard Lorentzian profile,  $L(\omega)$ , is also applied to represent the excitation population. By fitting this model with the data in Figure 1.8a (solid lines), strong agreement between the model and experiment was observed. Figure 1.8b represents calculations based on this model in a 2D map spanning the parameter-space of time delay and excitation laser energy. This map was used to extract the time delay dependence of fit parameters  $\Delta\chi(\tau)$  and  $\Delta E(\tau)$ , displayed in black symbols in Figure 1.8c,d. The behavior of these parameters can be well-described by biexponential expressions given by

$$\begin{aligned} \Delta\chi(\tau) &= \Delta\chi_f e^{-\frac{\tau}{\tau_f}} + \Delta\chi_s e^{-\frac{\tau}{\tau_s}}, \\ \Delta E(\tau) &= \Delta E_+ e^{-\frac{\tau}{\tau_+}} + \Delta E_- e^{-\frac{\tau}{\tau_-}}, \end{aligned} \quad (6)$$

where  $\Delta x_f$  and  $\Delta x_s$  are the fast and slow components of the  $\Delta x(\tau)$  fit, with characteristic timescales  $\tau_f$  and  $\tau_s$ , respectively.  $\Delta E_+$  and  $\Delta E_-$  are the fast and slow components of the  $\Delta E(\tau)$  fit, with characteristic timescales  $\tau_+$  and  $\tau_-$ , respectively. The result of the fits from Equation (6) are depicted by the solid red lines in Figure 1.8c,d.

The calculation of these parameters elucidates the underlying physics of the excitons in the system. The authors attributed the fast  $\Delta E_+$  component to an exciton-exciton interaction induced blue shift in the resonance, while the slow component,  $\Delta E_-$ , was assigned to band gap renormalization resulting from interactions between excitons and free carriers generated in the sample. Also, the fast  $\Delta x_f$  component was designated as the result of phase space filling and spectral broadening from excitons, whereas the slow  $\Delta x_s$  component relates to the effect of phase space filling, screening, and spectral broadening resulting from free carriers. From this model, both exciton-exciton interactions as well as higher order many-body interactions were observed, showing that many-body physics can indeed be generated among highly dense populations of charge carriers in TMD materials.

### ***1.5 The Electron-Hole Liquid***

Beyond the densities needed to generate many-body phenomena, novel electron-hole interactions may be seen. In traditional semiconducting materials such as Ge and GaAs, a highly dense electron-hole condensate has been observed in a number of experiments<sup>15</sup>. Asnine *et al.* measured significant photoconductivity in bulk Ge at liquid He temperatures for very high exciton densities on the order of  $10^{16} \text{ cm}^{-3}$ <sup>16</sup>, which they

attributed to an exciton Mott transition. However, Keldysh proposed that the conductivity of normally electrically neutral excitons at such high densities was due to the formation of a liquid condensate from an exciton gas. Electrons and holes in this liquid state are released from their bound exciton configurations, allowing for the possibility of observable conductivity<sup>17</sup>.

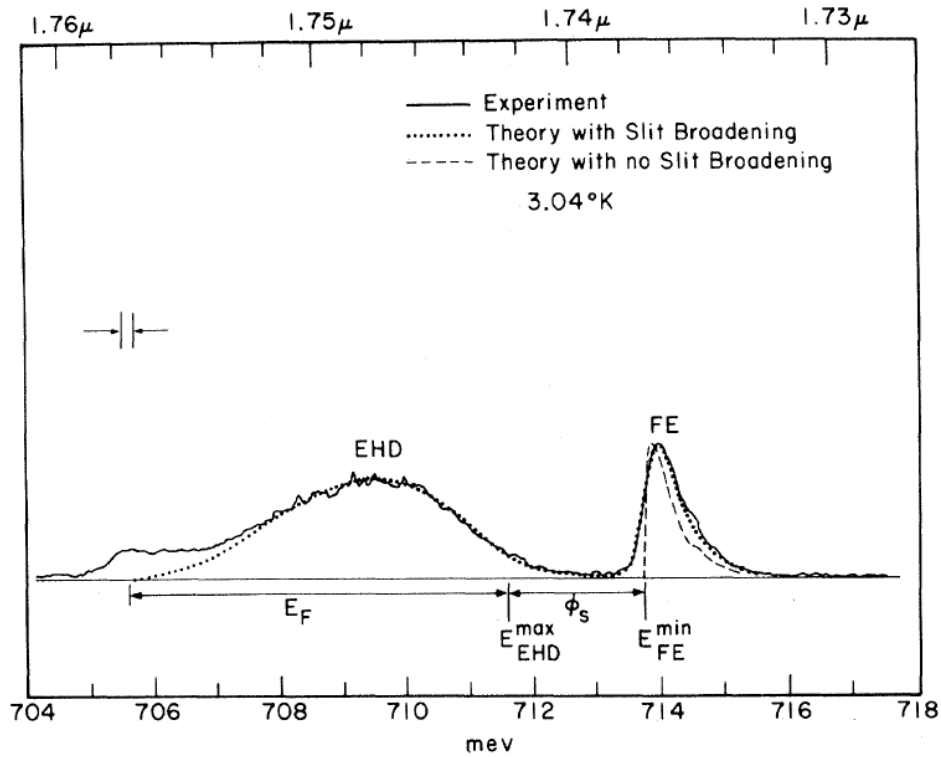


**Figure 1.9:** Photoluminescence spectrum of free electrons (FE) and electron-hole droplets (EHD) for bulk Ge as a function of laser energy (bottom scale) and wavelength (top scale). Solid line, small dashed line, and large dashed line represent experimental data, calculations based on electron-hole droplet theory with slit broadening, and calculations based on electron-hole droplet theory without slit broadening, respectively.  $E_F$  is the Fermi energy of the liquid,  $\phi_s$  is the condensation energy,  $E_{EHD}^{max}$  and  $E_{FE}^{min}$  are the maximum EHD energy and minimum FE energy, respectively. Measurements were performed at 3.04K. Adapted from Lo *et al.*<sup>18</sup>.

As evidence for the electron-hole liquid, Lo and colleagues measured the PL spectrum of bulk Ge and observed unique signatures at high exciton densities<sup>18</sup>. Figure 1.9 displays the results of these experiments. They observed two distinct peaks, where the higher peak at 714 meV corresponds to the established free exciton (FE) peak in Ge. The lower peak was attributed to the formation of electron-hole liquid droplets with a finite energy of condensation,  $\phi_s$ , separating the two peaks. By comparing these results to calculations from electron-hole liquid theory and factoring in slit broadening from the spectrometer (large dashed line in Figure 1.9), the data matches well with theory, suggesting that the lower energy peak is indeed the result of electron-hole liquid droplet formation.

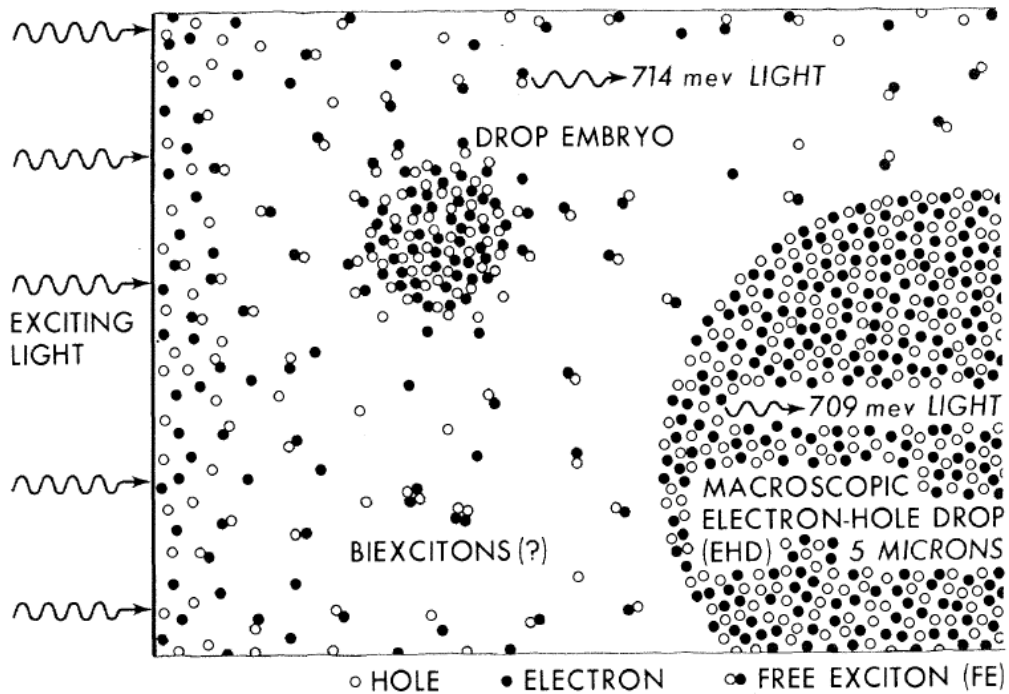


**Figure 1.10:** Schematic of electron-hole liquid droplet formation out of a gas of photoexcited excitons and free electrons and holes. Adapted from Jeffries<sup>15</sup>.

The observations of this study along with many others mentioned by Jeffries<sup>15</sup> advance the following picture of electron-hole liquid formation portrayed in Figure 1.10. At the left edge, excitation light strikes the surface of a semiconductor, generating photoexcited free electrons and holes. At high enough excitation power, the density of charge carriers increases and they form into an exciton gas. As excitons diffuse into the material, they encounter crystal defects or other imperfections that result in the accumulation of excitons in a dense liquid drop embryo. This liquid phase, then, tends to form deeper in the material, away from the surface. When the density of excitons at these local sites becomes high enough, drop embryos can grow into conductive electron-hole liquid droplets, where individual excitons dissociate into the liquid phase. The possibility of intermediate states between excitons and the liquid phase was also suggested, such as the formation of biexcitons.

With the discovery of electron-hole liquid droplet formation in bulk semiconductors such as Ge, Jeffries identified several criteria needed to characterize a condensate of charge carriers. The generation of the liquid phase is determined by a first order phase transition, and the liquid phase should display a distinct boundary. Additionally, an electron-hole liquid contains a constant density of charge carriers and is polarizable, meaning that an external voltage can be applied to evaporate the liquid droplet. Finally, the nonlinearity of the photoresponse should increase in the presence of a condensate, and the liquid phase should also disappear over time as electrons and holes within the phase recombine, recovering a typical electron-hole gas state.

Invariably, electron-hole liquid droplets like those investigated by Jeffries have only been observed at very low, liquid He temperatures and only in bulk semiconductors. With the increased quantum confinement of 2D materials such as TMDs, it becomes possible to create very high densities of charge carriers even at room temperature. In this dissertation, we propose a 2D optoelectronic device that is able to generate a stable, room temperature electron-hole liquid.

## ***1.6 Conclusion***

The work presented in this chapter describes the evolution of charge carrier interactions in 2D materials, and in TMDs in particular. We reviewed existing literature showing that photoexcited electrons and holes rapidly form into excitons in TMDs, and that these excitons quickly form into an exciton gas. As the density of carriers increases, exciton-exciton interactions occur, particularly in the form of exciton-exciton annihilation. At very high densities, band-gap renormalization indicates the presence of many-body interactions beyond that of two interacting excitons in TMDs. Interactions of charge carriers at even higher densities has not been reported in TMDs, yet in traditional bulk semiconductors, highly dense and interacting electron-hole liquid droplets have been repeatedly observed, but only at liquid He temperatures. This invites the possibility of generating an electron-hole liquid phase in TMD materials as well, which may also be present at higher temperatures.

## CHAPTER 2

### PROPERTIES OF ULTRATHIN MoTe<sub>2</sub> HETEROSTRUCTURES

#### ***2.1 Introduction***

To investigate highly confined, interacting electrons and holes, we consider a specific TMD material known as MoTe<sub>2</sub>. This chapter outlines the significant physical and electronic properties of MoTe<sub>2</sub> that have been established in the literature and highlights the advantages that result from these properties in observing interacting charge carriers. We present several properties that are common to all TMDs, yet as discussed in this chapter as well as in Chapter 3, we explain how MoTe<sub>2</sub> is chosen for its compatibility with our measurement techniques.

At the end of this chapter, we also briefly review the development of van der Waals heterostructures for optoelectronic devices. We examine the advantages of these structures for studying interacting charge carriers and discuss the existing literature of MoTe<sub>2</sub>-based heterostructures. This discussion forms a framework for our experimental device design, detailed in Chapter 3, as well as for subsequent measurements of this device described in the rest of this dissertation.

#### ***2.2 MoTe<sub>2</sub> Lattice Structure***

Figure 2.1 displays the basic lattice structure of  $\alpha$ -MoTe<sub>2</sub>, while Figure 2.1a portrays a side view of the lattice and Figure 2.1b shows a top-down view. A single

monolayer of MoTe<sub>2</sub> consists of a hexagonal lattice composed of both Mo and Te atoms in a trigonal prismatic (2H) structure, similar to other TMD materials<sup>19</sup>. Within a

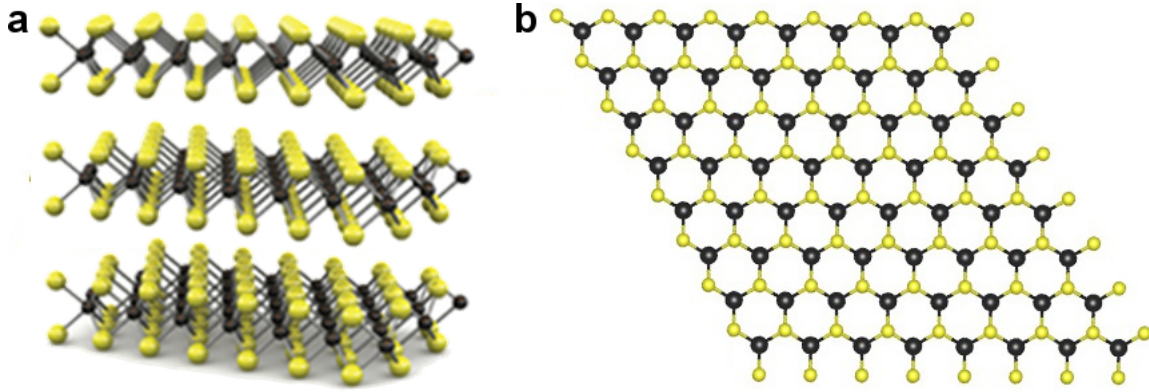


**Figure 2.1:** Crystal structure of hexagonal MoTe<sub>2</sub>. Mo atoms in black and Te atoms in yellow. **(a)** Side profile, revealing several atomic layers. **(b)** Top-down profile.

monolayer, the Mo and Te atoms are tightly held together through covalent bonding, yet the layers themselves are held together weakly by van der Waals interactions. Such a structure allows for the possibility of thinning down bulk MoTe<sub>2</sub> into ultrathin, 2D sheets of material by breaking the van der Waals interactions between atomic layers. A single monolayer of MoTe<sub>2</sub> is only  $\approx 0.7$  nm thick<sup>20</sup>. Because of this structure, 2D sheets of MoTe<sub>2</sub> useful for examining charge carrier interactions can be obtained using straightforward exfoliation techniques, as described in the next Chapter.

### ***2.3 Electronic Band Structure of MoTe<sub>2</sub>***

Compared to other TMDs, the electronic band structure of MoTe<sub>2</sub> is unique. Typical TMD materials such as MoS<sub>2</sub> and MoSe<sub>2</sub> have monolayer bandgaps in the visible spectrum, at energies of 1.85 eV<sup>4</sup> and 1.55 eV<sup>21</sup>, respectively. In contrast, the monolayer

bandgap of MoTe<sub>2</sub> is much smaller, at about 1.0 eV<sup>22</sup>. Ruppert *et al.* described the transition in the MoTe<sub>2</sub> bandgap energy as a function of layer thickness, displayed below in Figure 2.2. Bulk MoTe<sub>2</sub> shows very weak photoluminescence at around 0.8 eV – 0.9

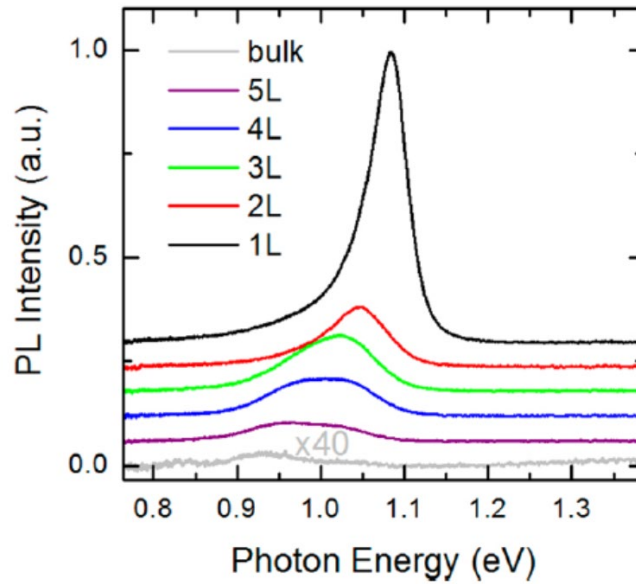


**Figure 2.2:** Photoluminescence spectra of MoTe<sub>2</sub> for various layer thicknesses ranging from monolayer (1L) to 5 atomic layers (5L), as well as bulk material. Spectra are shifted vertically for clarity. Adapted from Ruppert *et al.*<sup>22</sup>.

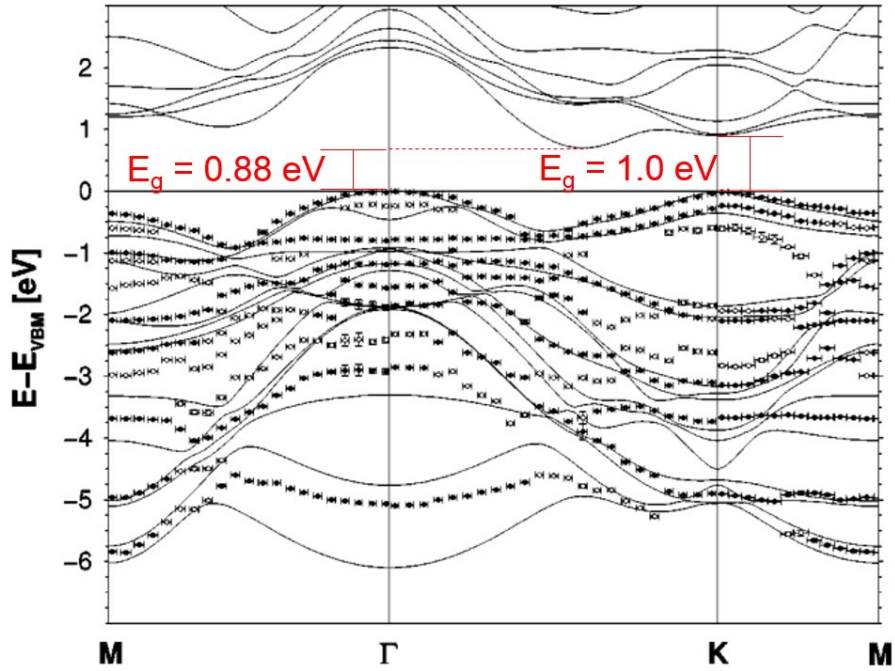


**Figure 2.3:** Calculations of MoTe<sub>2</sub> electronic band structure (solid lines) and experimental ARPES measurements of the valence band structure in MoTe<sub>2</sub> (symbols). Adapted from Boker *et al.*<sup>23</sup>.

eV, yet as the material becomes thinner, the bandgap redshifts to a value of 1.0 eV, and the photoluminescence significantly increases. This indicates a transition from an indirect to a direct bandgap as the thickness of MoTe<sub>2</sub> decreases.

These results corroborate the theoretical band structure of MoTe<sub>2</sub> described by Boker *et al.*<sup>23</sup> (Figure 2.3). They determined an indirect bandgap in MoTe<sub>2</sub> of  $\approx 0.88$  eV and a direct bandgap of  $\approx 1.0$  eV. The indirect gap in bulk MoTe<sub>2</sub> corresponds to a transition between the conduction band minimum halfway between the  $\Gamma$  and  $K$  Brillouin points and the valence band maximum at the  $\Gamma$  point. As the material becomes thinner, the direct gap becomes dominant and is defined as the transition between the conduction and valence bands at the  $K$  point.

This band structure evinces numerous interesting properties of MoTe<sub>2</sub> that are not present in other TMDs. The smaller direct bandgap of 1.0 eV is similar to Si, allowing

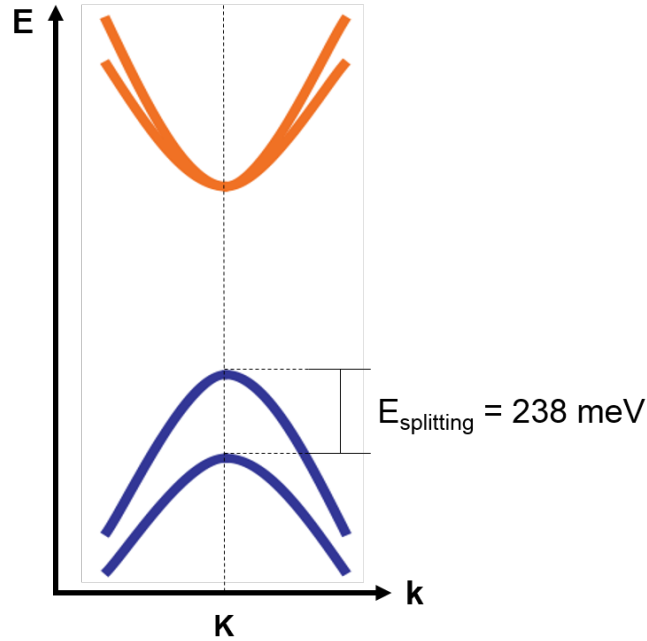


**Figure 2.4:** Schematic of MoTe<sub>2</sub> band structure at the K Brillouin point, highlighting the splitting of the valence band and high spin-orbit coupling. Adapted from Mak *et al.*<sup>24</sup>. MoTe<sub>2</sub> to be a potential ultrathin substitute for this commonly used semiconducting material. This bandgap value also indicates that MoTe<sub>2</sub> is active in the near-infrared regime, accessing a region of the optical spectrum that other TMDs cannot. Additionally, MoTe<sub>2</sub> displays unusually large spin-orbit coupling relative to other TMDs. This is represented schematically in Figure 2.4, where the spin-orbit coupling is determined by the splitting of the valence band. MoTe<sub>2</sub> exhibits a spin-orbit coupling of 238 meV, significantly higher than in MoS<sub>2</sub> or MoSe<sub>2</sub>, two other common TMDs, where the spin-orbit coupling values are 161 meV and 175 meV, respectively<sup>23</sup>. Spin-orbit coupling is a phenomenon that allows electrons of a given spin to selectively occupy a particular valence band level. The high spin-orbit coupling of MoTe<sub>2</sub>, then, makes it possible to

excite electrons of one particular spin, without exciting electrons of the opposite spin. Thus, MoTe<sub>2</sub> is a uniquely useful TMD for application in the emerging field of spintronics.

Clearly, the band structure of MoTe<sub>2</sub> is unique among TMDs and leads to unique properties and applications. For this reason, MoTe<sub>2</sub> is a significant material in which to study the effects of highly interacting charge carriers, as interactions may have a strong impact on performance. However, as will be described in greater detail in Chapter 3 of this dissertation, our ultrafast laser measurement apparatus was designed to explore optoelectronics in the near-infrared regime of the optical spectrum, and because of this, MoTe<sub>2</sub> was a natural choice of material for examining the physics of highly dense charge carriers.

#### ***2.4 Charge Carrier Lifetime in MoTe<sub>2</sub>***

Along with a layered lattice structure that allows for strong quantum confinement and a unique electronic band structure resulting in a number of useful properties and applications, MoTe<sub>2</sub> also exhibits unusually long charge carrier lifetimes. In fact, long carrier lifetimes have been demonstrated for a variety of TMD materials. Massicotte *et al.* utilized an ultrafast pulsed laser to measure the interlayer photocurrent as a function of time delay of a graphene-WSe<sub>2</sub>-graphene heterostructure photocell, displayed in Figure

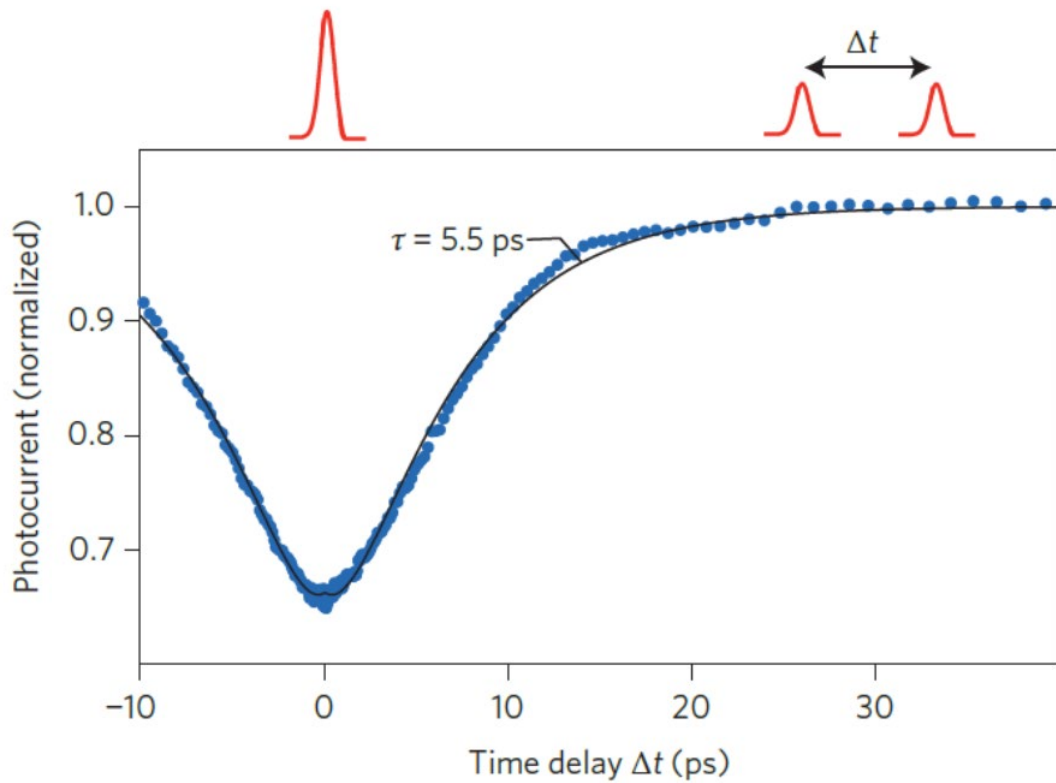


**Figure 2.5:** Photocurrent as a function of time delay in a graphene-WSe<sub>2</sub>-graphene photocell at a laser power  $P = 300 \mu\text{W}$  and an interlayer bias potential applied across the top and bottom layers of graphene  $V_B = 1.2 \text{ V}$ . Blue dots indicate experimental data and black solid line represents biexponential fit to the data. The laser profile is displayed above the plot both at short and long time delays. At short time delay, the two pulses overlap to generate a single intense pulse. At long time delay, the two smaller pulses are separated by  $\Delta t$ . Adapted from Massicotte *et al.*<sup>5</sup>.

2.5<sup>5</sup>. Their experimental data, shown in blue, indicated a clear dip in the photocurrent as the time delay approaches  $\Delta t = 0$ . By fitting this data to a biexponential function (black solid line in Figure 2.5), good agreement with the experimental data was achieved. A characteristic timescale of  $\tau = 5.5 \text{ ps}$  was extracted from this fit, which the authors identified as the charge carrier lifetime. A lifetime on the order of  $\approx 10 \text{ ps}$  is unusually long, as one would expect carriers moving vertically through an atomically thin heterostructure to escape or recombine on the order of a femtosecond timescale.

However, this long carrier lifetime in TMDs implies that an increasing density of carriers can be generated with little loss due to carriers leaving the system. This ability to create highly dense charge carriers further encourages the use of TMDs in studying the effects of charge carrier interactions.

Similar to other TMDs, MoTe<sub>2</sub> demonstrates long charge carrier lifetimes. Figure 2.6 portrays the interlayer photoresponse of a graphene-MoTe<sub>2</sub>-graphene heterostructure measured using an ultrafast pulsed laser. The characteristics of both the device and the laser will be discussed in greater detail in later chapters of this dissertation. In agreement with the work of Massicotte *et al.* described above, our experimental data (orange symbols in Figure 2.6) display a dip in observed photocurrent as the time delay  $\Delta t$  approaches 0. By fitting this data to a simple biexponential function, we observe good agreement with the data and extract a characteristic time constant  $\tau = 42.4$  ps. MoTe<sub>2</sub>, therefore, exhibits a carrier lifetime roughly similar to that of other TMDs, on the order of tens of ps, supporting the use of MoTe<sub>2</sub> as a material of study for examining the effects of highly interacting charge carriers.

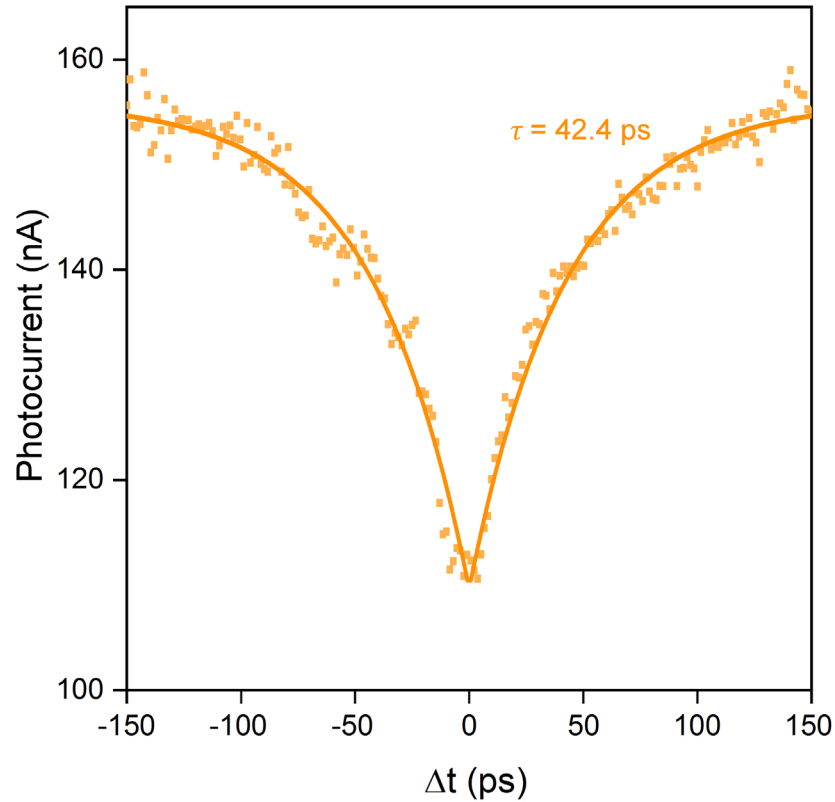


**Figure 2.6:** Photocurrent as a function of time delay in a graphene-MoTe<sub>2</sub>-graphene photocell at a laser power of 4.3 mW and no interlayer bias potential applied across the top and bottom layers of graphene. Orange symbols represent experimental data, and the orange solid line indicates a biexponential fit to the data.

### ***2.5 Van der Waals Heterostructures***

Along with a wide range of useful properties in MoTe<sub>2</sub> and other TMDs for optoelectronic applications in general and for examining interacting charge carriers specifically, further advancements have been observed in vdW heterostructures composed of a variety of 2D materials. Because of the weak van der Waals interactions between layers in TMDs and other 2D materials, it becomes possible not only to separate individual layers from the bulk, but also to reassemble them into composite heterostructures of one's choosing. This process, therefore, allows a high degree of

control in the construction of these heterostructures since they can be stacked one monolayer at a time. With this level of control, the process can be analogized to the assembly of lego structures<sup>25</sup> (Figure 2.7), where it becomes possible to tailor-make composite structures that combine the beneficial properties of their individual constituents, leading to the creation of high-performance devices.

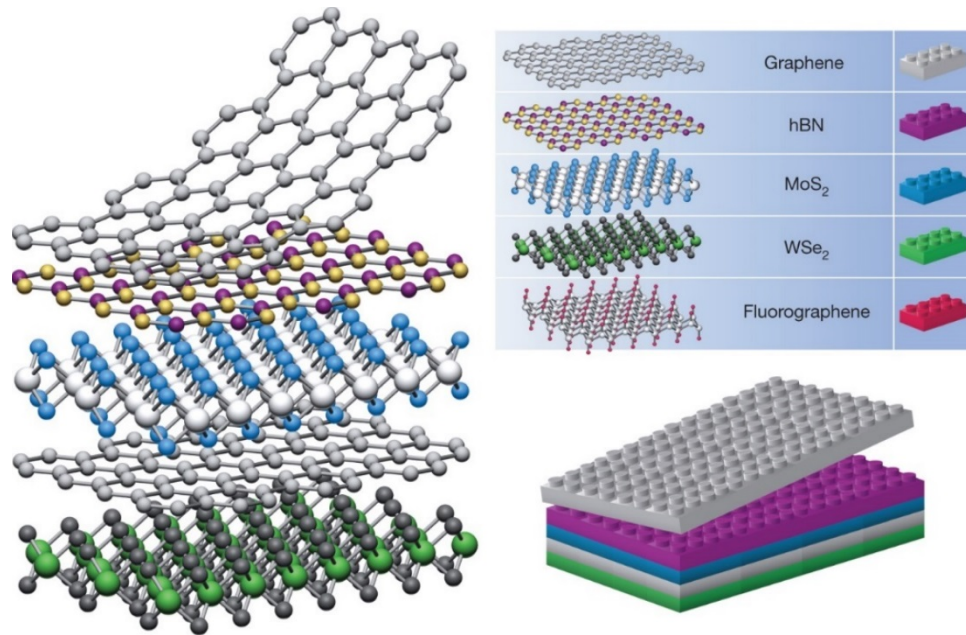


**Figure 2.7:** Schematic of van der Waals heterostructure assembly with a variety of 2D material constituents. Adapted from Geim *et al.*<sup>25</sup>.

Several devices utilizing this strategy have already been designed and created. The earliest of such heterostructures consisted of graphene-hBN structures to improve the performance of graphene devices<sup>26</sup>. Since then, a number of more complicated van der Waals heterostructure devices have been examined. Haigh *et al.* constructed a heterostructure containing dozens of reassembled layers of hBN and bilayer graphene<sup>27</sup>

(Figure 2.8). This structure was able to achieve a high density of states by utilizing the hBN layers as spacers and bilayer graphene as layers to facilitate intercalation.

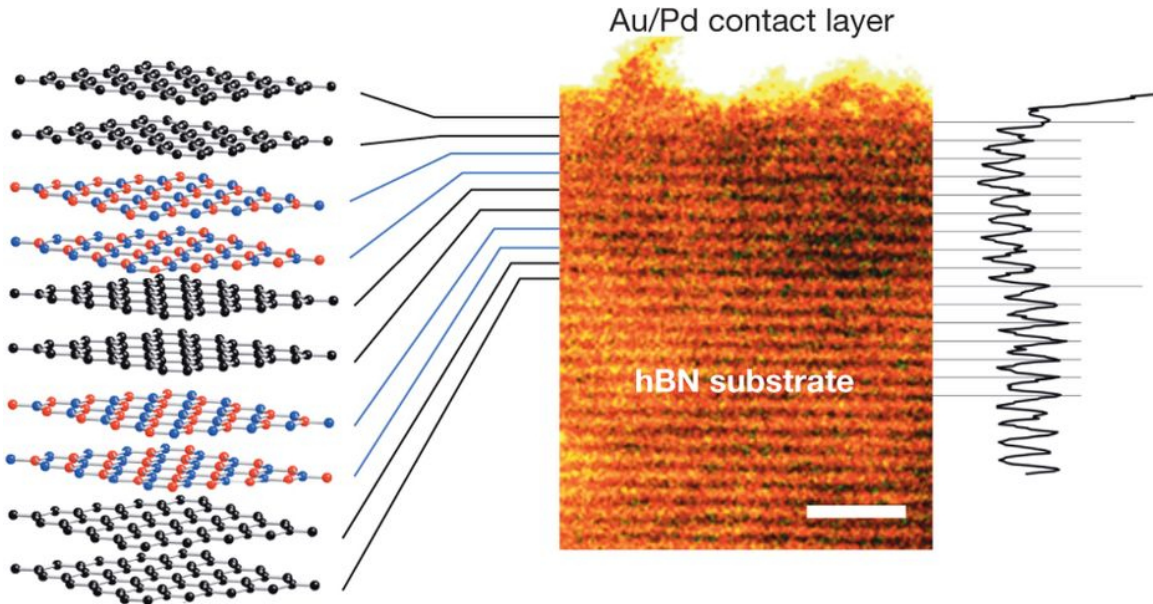


**Figure 2.8:** Graphene-hBN van der Waals heterostructure consisting of six stacked bilayers of graphene and hBN. Schematic of device shown on the left, and STEM cross-section and profile shown on the right. Scale bar is 2 nm. Adapted from Haigh *et al.*<sup>27</sup>.

Furthermore, Steinleitner *et al.* assembled a heterostructure composed of hBN and WSe<sub>2</sub> on a diamond substrate<sup>28</sup>. They showed that the additional hBN layer renormalizes the excitons in the WSe<sub>2</sub>, demonstrating that heterostructures can be used for dielectric engineering.

In addition to these developments, vdW heterostructures containing MoTe<sub>2</sub> have also been recently examined. In the work of Zhang *et al.*, a graphene-MoTe<sub>2</sub>-graphene heterostructure photodetector was fabricated utilizing a bulk flake of MoTe<sub>2</sub> as the middle layer<sup>29</sup> (Figure 2.9). Electrical contacts were attached on the top and bottom layers of graphene and used to measure the interlayer photocurrent generated from a  $\lambda =$

1064 nm infrared laser (Figure 2.9c). With this system, they determined that their graphene-MoTe<sub>2</sub>-graphene device displayed superior performance compared to van der Waals devices composed of other TMDs. They calculated a high responsivity of 110 mA

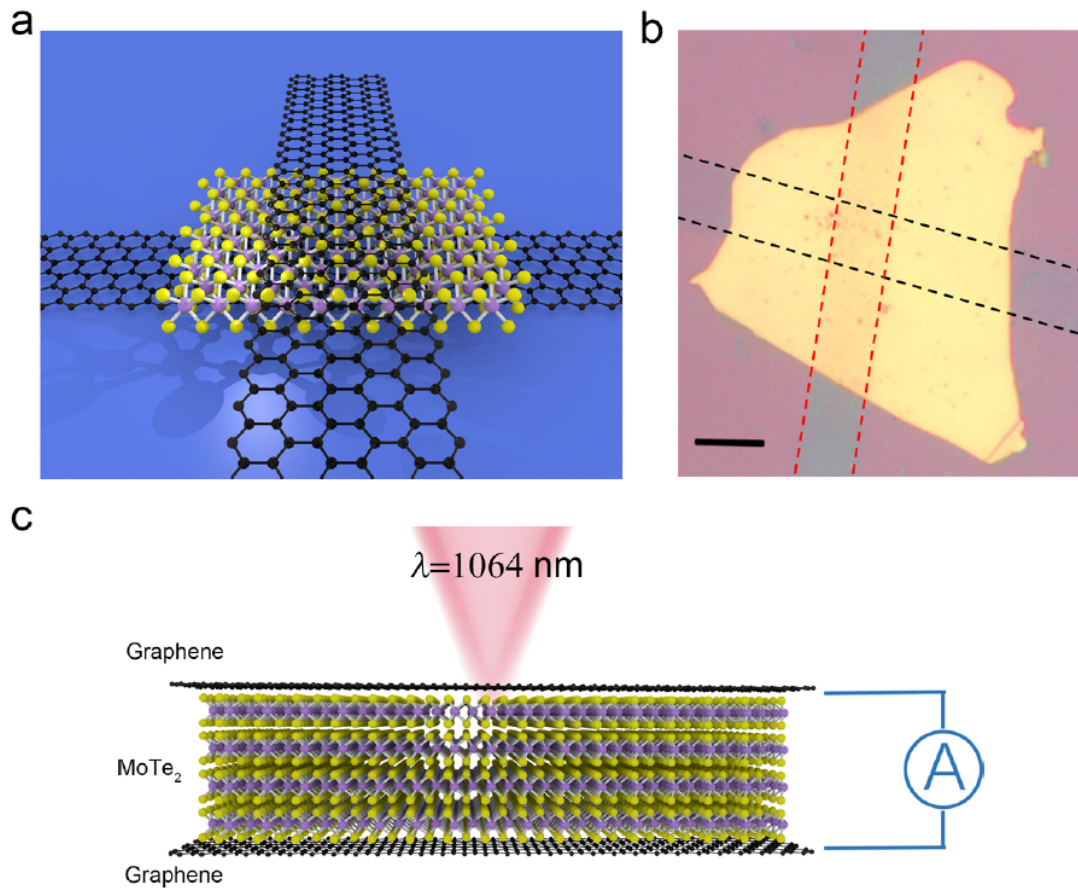


**Figure 2.9:** Graphene-MoTe<sub>2</sub>-graphene photodetector. **(a)** Schematic representation of the device. **(b)** Optical image of the device. Scale bar is 10  $\mu\text{m}$ . **(c)** Side profile schematic of device showing laser illumination at  $\lambda = 1064 \text{ nm}$  and interlayer contacts attached to the top and bottom layers of graphene. Adapted from Zhang *et al.*<sup>29</sup>.

$\text{W}^{-1}$  at 1064 nm illumination, high external quantum efficiency of 12.9% at 1064 nm, and rapid rise and fall times of 24  $\mu\text{s}$  and 46  $\mu\text{s}$ , respectively at 1064 nm. Thus, MoTe<sub>2</sub>-based heterostructures appear to show great potential for optoelectronic device applications.

Van der Waals heterostructures composed of TMDs may also contribute to the study of highly interacting charge carriers. Instead of using traditional metal contacts attached to a TMD material like MoTe<sub>2</sub> to examine interacting electrons and holes, ultrathin sheets of graphene can be attached to the MoTe<sub>2</sub> in a heterostructure and used as highly efficient contacts for measuring the photoresponse. Additionally, the interlayer photocurrent can be measured across the vertical interface of a MoTe<sub>2</sub> based heterostructure. This allows the charge carriers to undergo less scattering compared to measuring the photocurrent laterally through the device. Due to this, faster and more efficient photoresponse results and losses due to scattering are minimized. This leads to better measurement of highly interacting phenomena in ultrathin TMDs like MoTe<sub>2</sub>.

## ***2.6 Conclusion***

In this chapter, we introduced MoTe<sub>2</sub> as a material well suited for studying the effects of highly interacting charge carriers. We examined the physical lattice structure of this material and how this structure contributes to easily generating highly confined, 2D sheets of MoTe<sub>2</sub>. In addition, the electronic band structure of MoTe<sub>2</sub> was also investigated. We showed that MoTe<sub>2</sub> exhibits a number of unique properties, such as small direct and indirect bandgaps in the near-infrared regime, a direct bandgap approximating the value of Si, and large spin-orbit coupling that makes MoTe<sub>2</sub> promising for the emerging field of spintronics. For a material with such potential, the effects of interacting carriers could play a significant role in its properties and performance. Furthermore, photoexcited carriers in MoTe<sub>2</sub> display long lifetimes, on the order of 10s

of picoseconds, allowing higher densities of carriers to be generated in this material. At the end of the chapter, we explored the development of van der Waals heterostructures and how these structures open many doors for novel optoelectronic devices. These structures were also shown to be directly beneficial to examining interacting charge carriers by improving the efficiency of the observed photoresponse. MoTe<sub>2</sub> based heterostructures, therefore, prove to be highly promising for studying the effects of highly interacting electrons and holes.

## CHAPTER 3

### DEVICE FABRICATION AND MEASUREMENT

#### 3.1 Introduction: Device Design

To probe the behavior of highly interacting charge carriers, we consider a graphene-MoTe<sub>2</sub>-graphene heterostructure photocell, shown schematically in Figure 3.1.

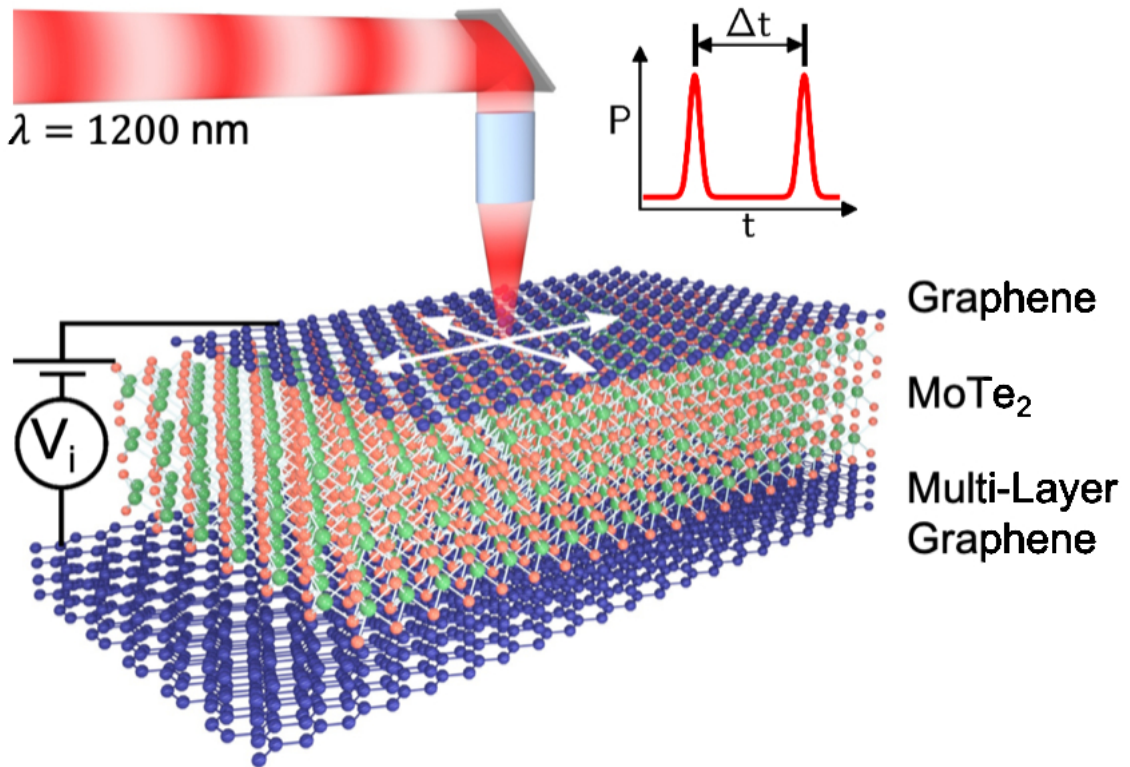


**Figure 3.1:** Schematic of graphene-MoTe<sub>2</sub>-graphene photocell with graphene layers labelled in blue and MoTe<sub>2</sub> layer labelled in green and orange. An ultrafast pulsed laser with  $\lambda = 1200 \text{ nm}$  photoexcites the device. White arrows indicate the spatial scanning capability of the laser. An interlayer bias potential,  $V_i$ , is applied vertically across the structure. Upper right inset, laser power  $P$  vs. time  $t$ , showing pulses separated by time delay  $\Delta t$ .

A thin top layer of mono- or few-layer graphene and a thick bottom layer of graphene sandwich a thicker, yet still ultrathin, layer of MoTe<sub>2</sub>. A thin top layer is chosen to ensure that most optical absorption occurs in the MoTe<sub>2</sub> layer. Electrical contacts are attached to the top and bottom layers of graphene in order to measure the interlayer photocurrent across the device and apply an interlayer bias potential,  $V_i$ . An ultrafast pulsed laser with time delay  $\Delta t$  between pulses and  $\lambda = 1200$  nm is spatially scanned across the surface of the sample, exciting electrons and holes in the MoTe<sub>2</sub> layer.

In this chapter, we describe in detail the procedures used to fabricate such a device, and provide a basic understanding of the laser measurement apparatus used to explore the optoelectronics of this device and investigate the effects of interacting charge carriers. First, we explain the methods used to prepare Si chips for the fabrication process. Next, mechanical exfoliation of bulk material is performed to generate each ultrathin layer of the heterostructure. We explore a wide range of exfoliation techniques and compare their effectiveness. After obtaining each layer, we utilize a modified dry transfer technique to stack these layers into a completed heterostructure, and present a few strategies used to improve the assembly process. We then expound on the methods used to fabricate devices out of these heterostructures using cleanroom fabrication techniques. We present the specific steps that were implemented in the fabrication process, as well as alternative procedures used to improve device performance. Lastly, we discuss the details of the optoelectronic measurements of these devices.

### 3.2 Wafer Preparation

Graphene-MoTe<sub>2</sub>-graphene heterostructures are fabricated on standard Si substrates. We utilize 2-inch Si/SiO<sub>2</sub> wafers with a 290 nm oxide layer (Figure 3.2a), which provide a thick enough oxide layer to observe clear optical contrast between ultrathin flakes and the substrate. Because individual flakes are usually only a few microns long on a side, it becomes challenging to locate these flakes on a Si chip. In order to make the process of finding usable flakes easier, Si wafers are pre-fabricated with a series of identifying markers (Figure 3.2b). To do this, we perform standard

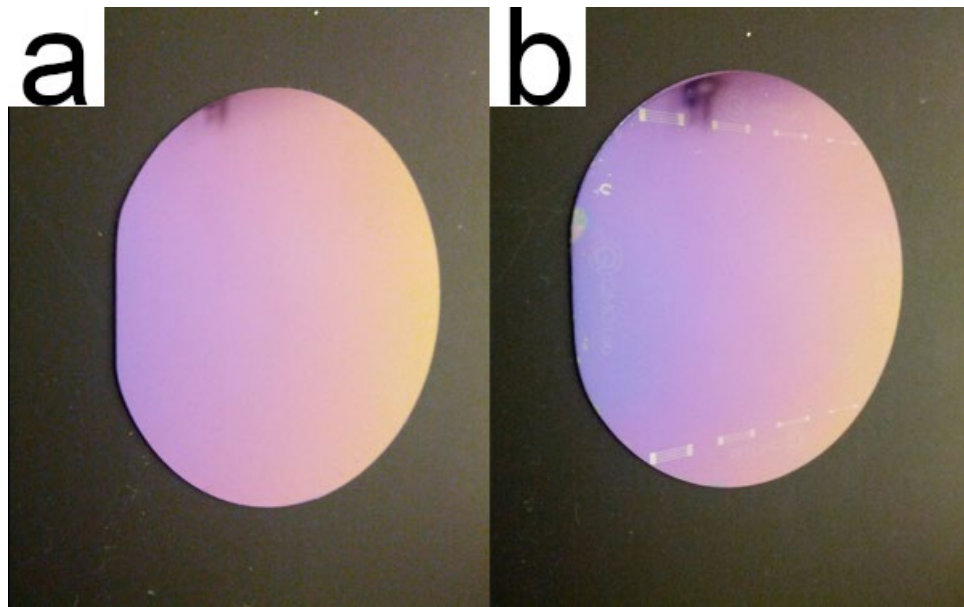


**Figure 3.2:** Si wafers used as substrates for graphene-MoTe<sub>2</sub>-graphene heterostructures. **(a)** Commercial 2-inch diameter Si/SiO<sub>2</sub> wafer with a 290 nm oxide. **(b)** Same Si wafer with etched identifying markers used to locate ultrathin flakes or devices.

photolithography techniques using a Karl Suss mask aligner in a cleanroom environment.

First, we spin-coat a layer of 5214 resist onto the wafer at 4000 rpm for 40 s with a ramp

of 1000 rpm/s. Next, a layer of HMDS polymer is also spin-coated onto the wafer under the same conditions. We then heat the wafer on a hotplate at 110°C for 5 min in order to let the resist set. Afterwards, we transfer the wafer to the Karl Suss machine and align it with a customized mask. We then expose the resist to  $\approx 15$  s of ultraviolet radiation. The sample is developed in AZ 400K developer for 1 min and rinsed with DI water. Lastly, the wafer is transferred to a reactive ion etching (RIE) station where it is etched using standard  $\text{CH}_4$  and  $\text{CH}_3\text{F}$  gasses for 2 min. The resist is then washed away in an acetone solution, leaving behind the patterned Si wafer.

Since commercial Si wafers exhibit a variety of surface defects and contaminants, cleaning procedures must also be performed in order to prepare them for device fabrication. After patterning the wafers, they are cut into square chips about half a centimeter on a side using a diamond scribe. These chips then undergo a rough cleaning step using sonication. Several chips are placed in a beaker filled with acetone, which is sonicated for 15 min. Afterward, each chip is removed from the beaker and rinsed in acetone and IPA before being dried with  $\text{N}_2$  gas. Because contamination may occur at a micro- or nanoscale, more sophisticated cleaning requirements are also performed. We utilize the RIE station to perform  $\text{O}_2$  plasma on Si chips for 30 s in order to ensure atomic-scale cleanliness of the chips.

Usually, both the sonication and  $\text{O}_2$  plasma steps are not performed in conjunction since the  $\text{O}_2$  plasma procedure is generally sufficient to clean substrates. However, though  $\text{O}_2$  plasma generates cleaner Si chips, this method also makes it harder to transfer atomic layer flakes from one Si substrate to another. The reason for this is unknown, yet

because of this, there is a balance and trade-off in using these two cleaning procedures. Sonication leads to dirtier substrates, yet allows for easier transfer. O<sub>2</sub> plasma, on the other hand, creates cleaner substrates but makes transfer more difficult. The choice of which procedure to use depends on the specific needs of the device to be made. We successfully generated graphene-MoTe<sub>2</sub>-graphene heterostructure devices using each substrate cleaning method.

### ***3.3 Exfoliation of Atomic Layer Materials***

With cleaned and prepared substrates, we utilize mechanical exfoliation of bulk material onto these substrates to generate each atomically thin layer of the heterostructure. We use a wide range of equipment, shown in Figure 3.3, to carry out the

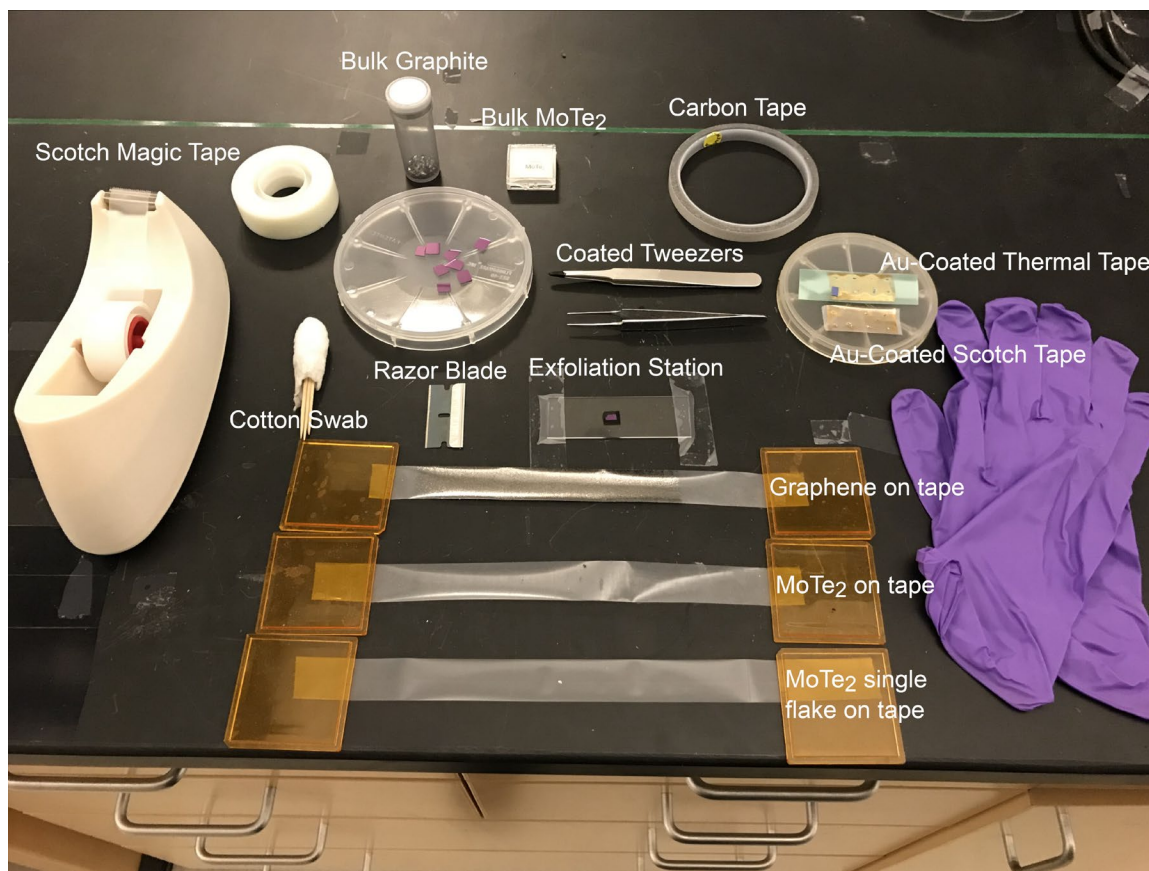


**Figure 3.3:** Equipment and materials used for various methods of exfoliating atomically thin graphene and MoTe<sub>2</sub>. exfoliation process. Along with patterned Si chips, we obtain bulk Kish graphite from Covalent Materials and bulk MoTe<sub>2</sub> flakes from 2D Semiconductor. Gloves are used throughout the exfoliation process to prevent contamination due to hand oils and other contaminants. Scotch tape is utilized to perform the exfoliation, using both original Scotch tape as well as the Scotch Magic brand of tape. For all exfoliation methods, a common exfoliation station is created that consists of a standard glass slide attached to the lab bench with tape. A small piece of carbon tape is placed in the middle of the glass slide, and a Si chip is then affixed to the carbon tape during the exfoliation process. The other elements in Figure 3.3 are used for particular exfoliation techniques. By using

these materials and equipment, ultrathin top and bottom layers of graphene as well as MoTe<sub>2</sub> can be produced, as shown in Figure 3.4.

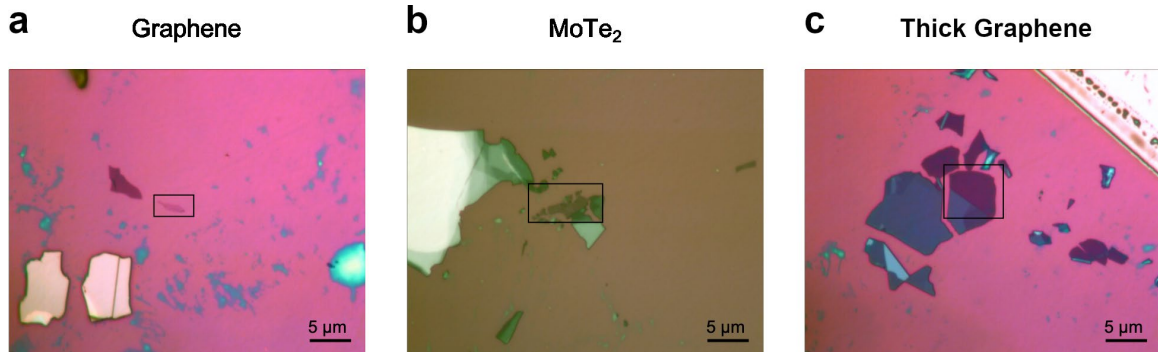


**Figure 3.4:** Optical images of (a) top graphene, (b) MoTe<sub>2</sub>, and (c) bottom graphene layers of a graphene-MoTe<sub>2</sub>-graphene heterostructure obtained from mechanical exfoliation. Top and bottom graphene were generated using the standard exfoliation technique while the MoTe<sub>2</sub> was generated using the low angle method. Black boxes highlight ultrathin regions used to construct a heterostructure.

In this section, we describe a variety of exfoliation methods to produce these flakes, highlighting the advantages of each technique for exfoliating certain materials. In Section 3.3.1, we present a standard exfoliation procedure adapted from techniques in the literature. Section 3.3.2 describes a razor blade exfoliation method that improves upon the standard method for exfoliating TMDs. In Section 3.3.3, we explain a third technique for exfoliation known as the low-angle method, which significantly improves the ability to exfoliate MoTe<sub>2</sub> in particular. Finally, Section 3.3.4 describes a novel exfoliation technique adapted from recent literature, known here as the gold exfoliation method, which can substantially improve MoTe<sub>2</sub> exfoliation, facilitating the creation of graphene-MoTe<sub>2</sub>-graphene heterostructures.

### 3.3.1 Exfoliation: Standard Method

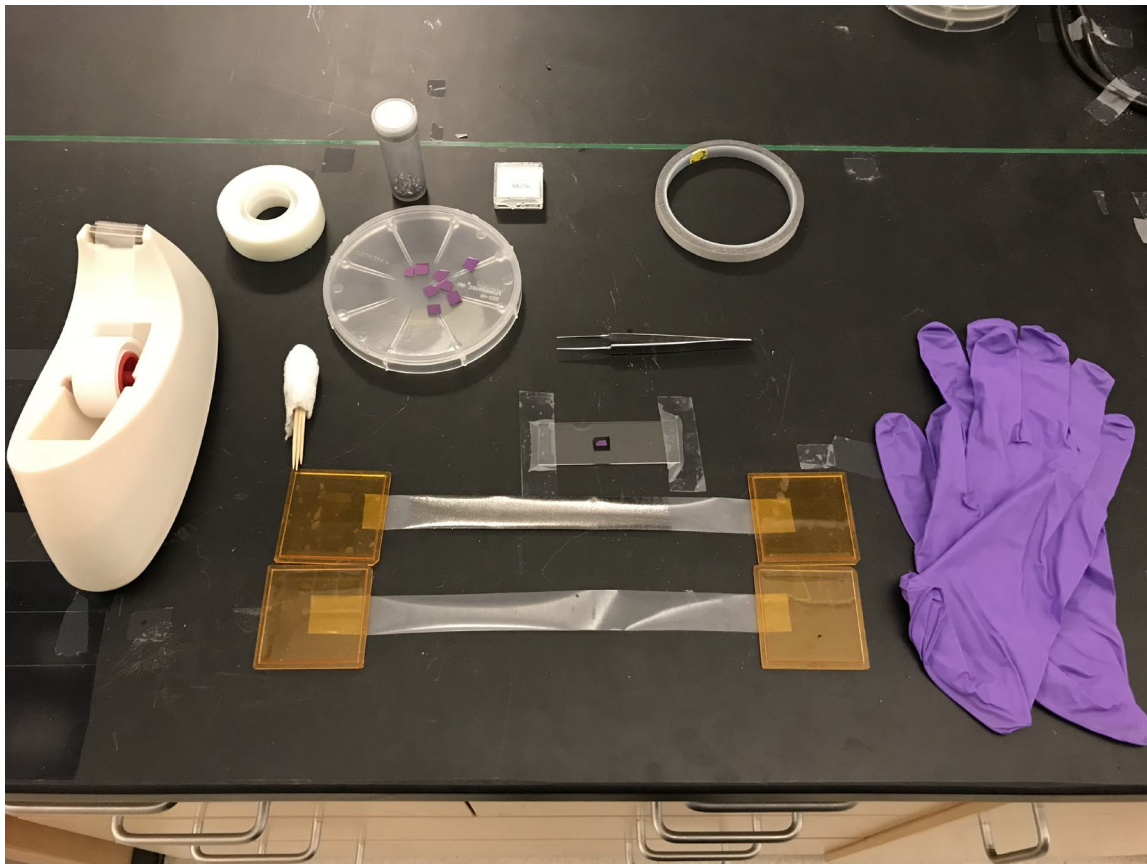


**Figure 3.5:** Equipment and materials used for the standard method of exfoliating atomic layer materials.

Our standard method of exfoliating 2D materials involves repeated peeling of bulk flakes with Scotch tape, similar to previous reports in literature<sup>30</sup>. The materials and equipment used in this method are shown in Figure 3.5 as a subset of the equipment shown in Figure 3.3. We obtain a large piece of either Scotch clear tape or Magic brand tape, and place a few flakes of bulk material in the center of the tape. By repeatedly sticking and unsticking the tape to itself, we peel off layers of the bulk flakes and spread them throughout the surface of the tape, ideally producing a uniformly thin layer of either graphene or MoTe<sub>2</sub>. Examples of this are labelled “Graphene on tape” and “MoTe<sub>2</sub> on

tape” in Figure 3.3 and also shown in Figure 3.5. As seen in these figures, graphene on tape is distinguished by a darker color compared to MoTe<sub>2</sub>. Next, we attach a Si chip to an exfoliation station and set the prepared tape sticky side down on top of the chip. The tape is then pressed into the Si using a cotton swab, shown in Figures 3.3 and 3.5, in order to improve contact between the tape and the substrate. A cotton swab is preferred for this process rather than simply using finger strength since the cotton proves more gentle than other methods, which we believe helps preserve flake integrity and produce larger thin flakes for heterostructure construction. We then slowly peel off the tape from the Si chip, leaving behind ultrathin flakes of material on the substrate. After exfoliation, suitable flakes for a heterostructure are found by searching the Si chip using an inspection microscope.

This method proves highly effective for generating graphene flakes of various thicknesses, allowing us to obtain the top and bottom layers of our desired heterostructure. In addition, we found this method also works well in creating ultrathin flakes of hBN, another 2D material. However, the standard method is generally not effective for producing atomic layer TMDs, as the bulk material tends to break apart into small, unusable chunks rather than separate along the van der Waals bonds into thin sheets. This creates a problem in generating the middle layer of our desired heterostructure, ultrathin MoTe<sub>2</sub>, which is the active material in which we plan to explore the effects of highly interacting charge carriers. Because of this, alternative methods of exfoliation that specifically improve the results for TMDs are necessary.

### 3.3.2 Exfoliation: Razor Method

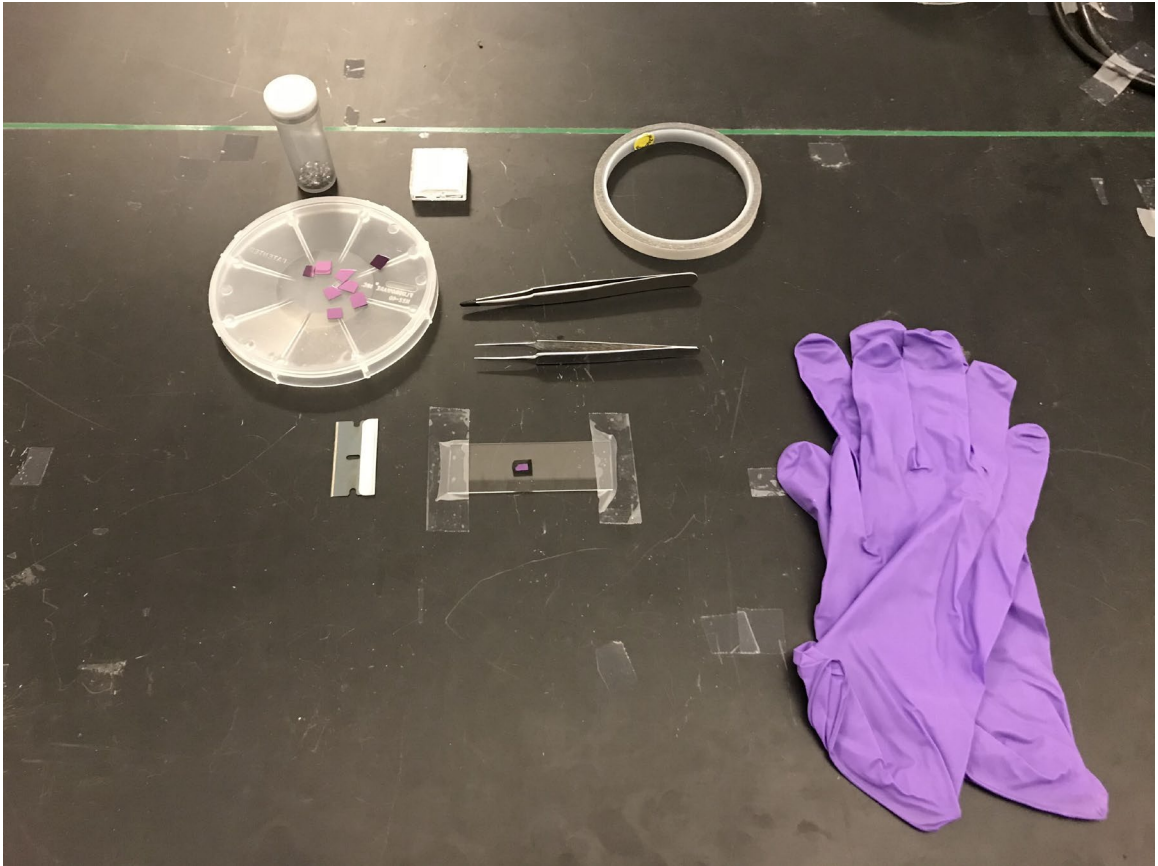


**Figure 3.6:** Equipment and materials used for the razor method of exfoliating atomic layer materials.

Another exfoliation technique that improves upon the standard method for exfoliating TMDs is known as the razor method. The materials and equipment needed to perform this process are shown in Figure 3.6. In this procedure, we once again construct an exfoliation station and attach a Si chip on top of the carbon tape. This technique, however, doesn't involve the use of Scotch tape. Instead, a bulk flake of material is placed directly onto the Si substrate. Another piece of carbon tape is then wrapped around the tip of a pair of tweezers, labelled "Coated Tweezers" in Figure 3.3 and also

shown in Figure 3.6. A second large flake of the same material as the flake placed on the substrate is then coated over the carbon tape on the tweezers, making sure that none of the tape is exposed. The coated tweezers are then used to press the into the flake on the substrate, ensuring good contact between the two. With this bulk flake now relatively secured to the substrate so that it won't slide around easily, a razor blade is used to carefully cleave layers off of the bulk flake. After several iterations of cleaving, pieces of ultrathin material may appear at the edges of the bulk flake or separately on another part of the Si chip.

We find this technique improves on the exfoliation of TMDs, and works particularly well for MoS<sub>2</sub>, MoSe<sub>2</sub>, WS<sub>2</sub>, and WSe<sub>2</sub>. However, this method only moderately improves the effectiveness of generating ultrathin flakes of MoTe<sub>2</sub>. This may be due to the large lattice mismatch between Mo and Te, which makes the material less physically stable and harder to exfoliate. Due to this, additional methods are needed for producing atomically thin MoTe<sub>2</sub>.

### ***3.3.3 Exfoliation: Low Angle Method***

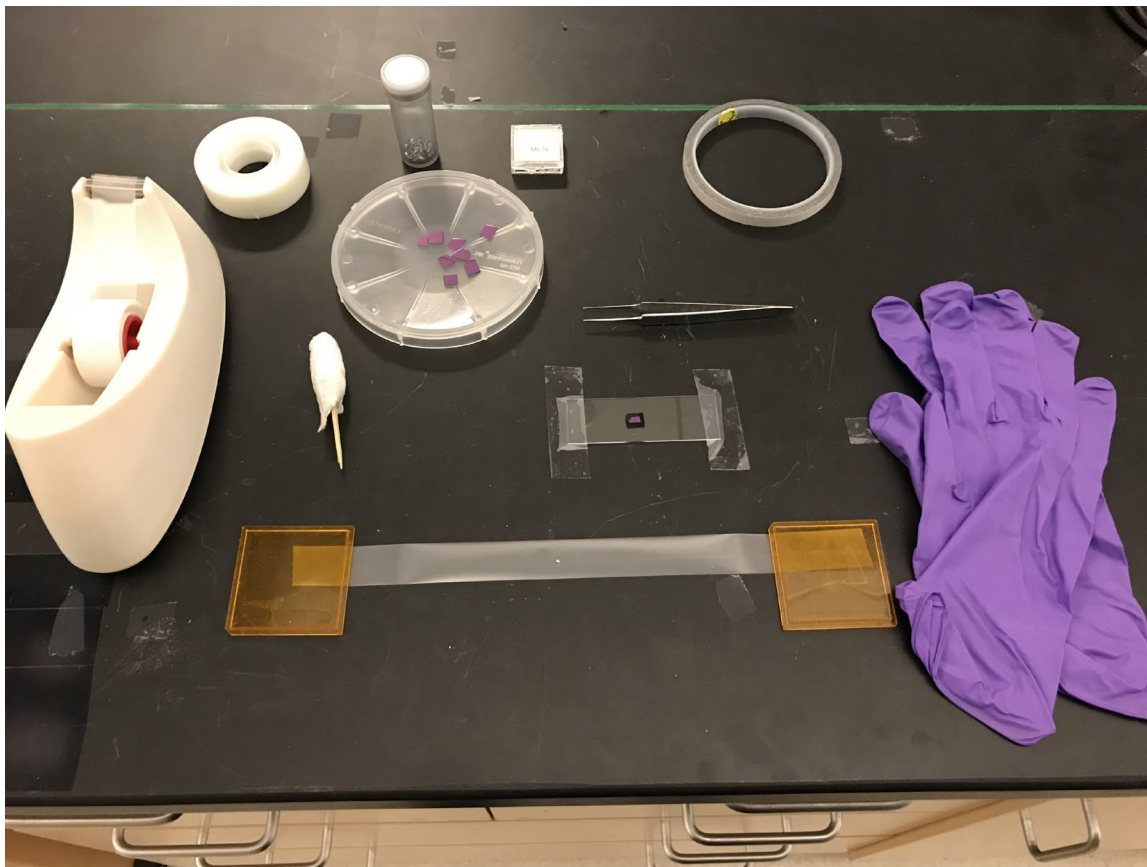


**Figure 3.7:** Equipment and materials used in the low angle method of exfoliating atomically thin materials.

The low angle exfoliation technique provides a reasonably reliable method of generating sufficiently large 2D flakes of  $\text{MoTe}_2$ . The equipment and materials needed for this procedure as shown in Figure 3.7. This method is a variation of the standard exfoliation technique where the aim is to more gently separate atomically thin layers from bulk material. Scotch Magic tape is preferred for this technique, as we consistently found a marked improvement in the number and size of ultrathin  $\text{MoTe}_2$  flakes using Magic brand tape compared to the standard variety.

In this process, we obtain a large piece of Scotch Magic tape, similar to the standard method, and place a single bulk flake of material in the center of the tape. An example of this can be seen labelled “MoTe<sub>2</sub> single flake on tape” in Figure 3.3, and is also shown in Figure 3.7. We affix the tape to the side of the lab bench using smaller pieces of tape, and then we obtain a second large piece of tape, which we set sticky side down on the first piece of tape. We use a cotton swab to enhance contact between the two pieces of tape, and then we carefully peel the pieces of tape apart. The method of peeling the tape has a significant impact on the resulting quality of ultrathin layer exfoliated. We peel the two pieces of tape in such a way as to minimize the angle between them and keep the tension on the tape as high as possible. We also peel them apart as slowly as possible, on the order of 0.1 mm/s or slower, which requires substantial concentration on the process. Afterward, the second piece of tape contains a single thinner flake at the center. A third large piece of tape is then obtained, and this process of sticking the two pieces of tape together and peeling them apart is repeated at least two more times but potentially more, generating thinner and thinner flakes at the center of the tape.

Afterward, the final piece of tape is used for direct exfoliation onto a Si substrate. An exfoliation station is created, and a Si chip is attached to it. The tape is then placed sticky side down on top of the substrate, and a cotton swab is used to improve the contact between the tape and the Si chip. The tape is then peeled off the substrate using the same low angle, high tension, and slow peeling technique, leaving behind an atomically thin flake on the Si. This technique is the main procedure we utilize to generate ultrathin

MoTe<sub>2</sub>, allowing us to effectively produce the middle layer of our desired graphene-MoTe<sub>2</sub>-graphene heterostructure.

### 3.3.4 Exfoliation: Gold Assisted Method



**Figure 3.8:** Equipment and materials used in the gold assisted method of exfoliating atomically thin materials.

Another reliable method of creating 2D flakes of MoTe<sub>2</sub> is known as the gold assisted technique, which has been adapted from a procedure developed by Desai *et al.*<sup>31</sup>. Since van der Waals interactions between Au and TMDs are stronger than the interactions between individual layers of a TMD, then by coating bulk TMDs with gold,

it becomes possible to peel off the gold layer, taking an ultrathin flake of TMD material with it. This gold layer can be etched away, revealing the atomically thin TMD.

The equipment and materials to carry out this process are shown in Figure 3.8. First, a piece of clear Scotch tape is obtained, and several bulk flakes of material are placed on the sticky side of the tape. This piece of tape is then taken to an electron beam evaporator to deposit a thin layer of 1-2 nm of gold onto the sticky side of the tape. An example of the resulting tape after evaporation is labelled “Au-Coated Scotch Tape” in Figure 3.3, and is also shown in Figure 3.8. At this point, a piece of thermal tape is attached to the Scotch tape, and the two are quickly peeled apart, leaving gold residue and thin flakes of material on the thermal tape. An image of this is labelled “Au-Coated Thermal Tape” in Figure 3.3, and is also seen in Figure 3.8. Si chips are then stuck to the thermal tape, polished side down. The tape with Si substrates attached is then taken to a hotplate and heated to 120°C, which melts off the adhesive on the tape and releases the Si chips. An example of the thermal tape on the hotplate can be seen in Figure 3.8. The Si substrates, which now contain ultrathin flakes of material coated with gold on their surfaces, are etched in a commercial gold etchant solution for 30 s to remove the gold layer, leaving behind atomically thin material.

This method is slightly more effective in generating ultrathin MoTe<sub>2</sub> compared to the low angle technique, but is also more time and labor intensive. For this reason, the low angle method is generally preferred for creating 2D MoTe<sub>2</sub>, yet the gold assisted procedure is still useful when large-area, thin flakes of MoTe<sub>2</sub> are absolutely necessary. In short, the standard exfoliation method proves effective in generating ultrathin graphene

layers while either the low angle or gold assisted technique is sufficient to produce atomically thin MoTe<sub>2</sub>. With these methods, we can successfully obtain the building blocks needed to construct a graphene-MoTe<sub>2</sub>-graphene heterostructure to investigate highly interacting charge carriers.

### 3.4 Building a Heterostructure: Dry Transfer Technique

Once ultrathin samples of graphene and MoTe<sub>2</sub> have been isolated, we assemble them into a graphene-MoTe<sub>2</sub>-graphene heterostructure using a dry transfer technique adapted from Gomez *et al.*<sup>32</sup>. We utilize a custom-built transfer microscope, shown in

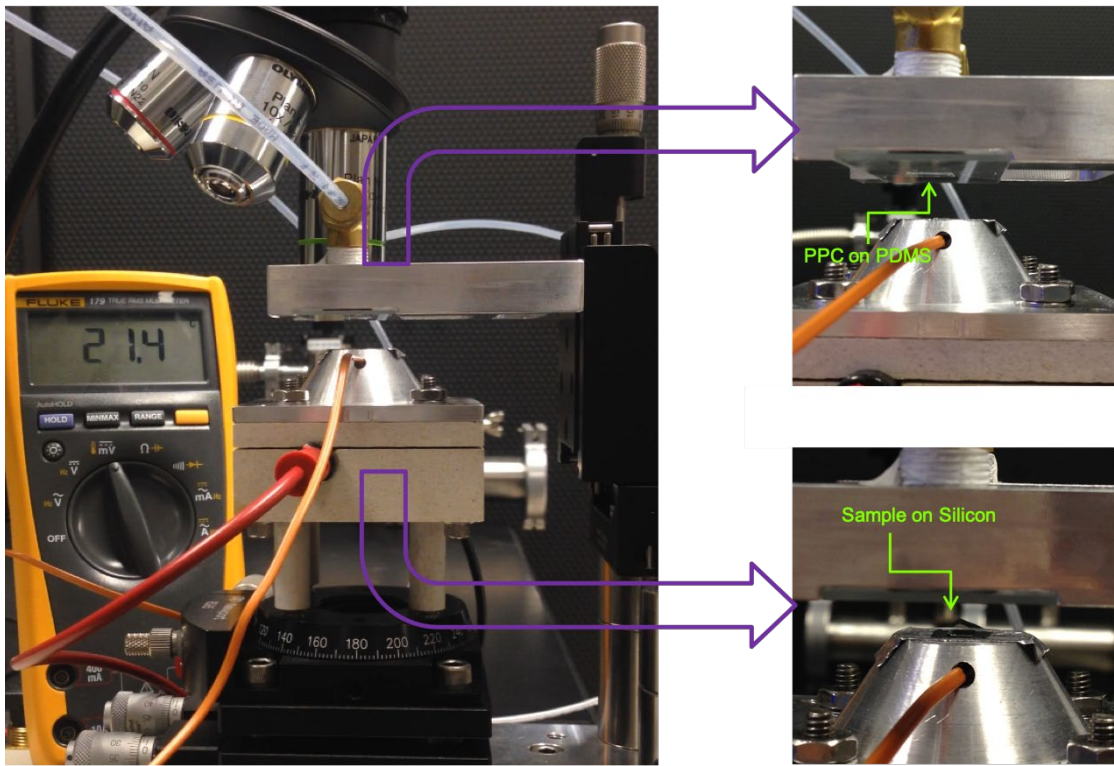


**Figure 3.9:** Optical image of a customized microscope system used in the dry transfer process of assembling graphene-MoTe<sub>2</sub>-graphene heterostructures. Left image, side profile of the microscope, showing all components. Upper right image, zoomed-in

profile of the cantilever with stamp attached. Lower right image, zoomed-in profile of bottom sample stage.

Figure 3.9, to carry out this procedure. The microscope consists of two essential components, an upper cantilever (upper right image in Figure 3.9) and a bottom sample stage (lower right image in Figure 3.9). The sample stage is composed of a machined aluminum surface with aluminum tape and carbon tape, respectively, attached to the surface. The aluminum tape improves adhesion of the carbon tape to the stage while the carbon tape itself holds the sample. A small hole, visible in the lower right image of Figure 3.9, is drilled into the sample stage and provides access for a thermocouple wire to be placed about 4 mm below the surface of the sample. This allows for accurate temperature readouts during the transfer process through a multimeter attached to the thermocouple. The temperature of the sample stage is controlled through a resistive heating wire attached to the bottom of the stage. The stage can move freely in the x- and y-directions and rotate in the xy-plane through the use of controllable knobs.

The cantilever is also constructed from machined aluminum and contains two slots that hold a stamp used to pick up atomically thin flakes in the transfer process. As shown in Figure 3.9, the stamp consists of a base made out of a standard glass slide. On top of this, we place a small square section of polydimethylsiloxane (PDMS) polymer, about 0.75 in long on a side, in the center of the glass slide. With this complete, we spin-coat a thin layer of polypropylene carbonate (PPC) polymer onto the stamp at 6000 rpm for 40 s with a 1000 rpm/s ramp. We then heat the stamp at 180°C for 5 min on a hotplate in order to let the PPC set. The cantilever can also move freely in the z-direction by using another set of tunable knobs. An objective lens, seen in left image in Figure 3.9,

is placed above the cantilever and also moves freely in the z-direction to allow focusing on both the stamp and the sample during the transfer process. We utilize commercial 5x,

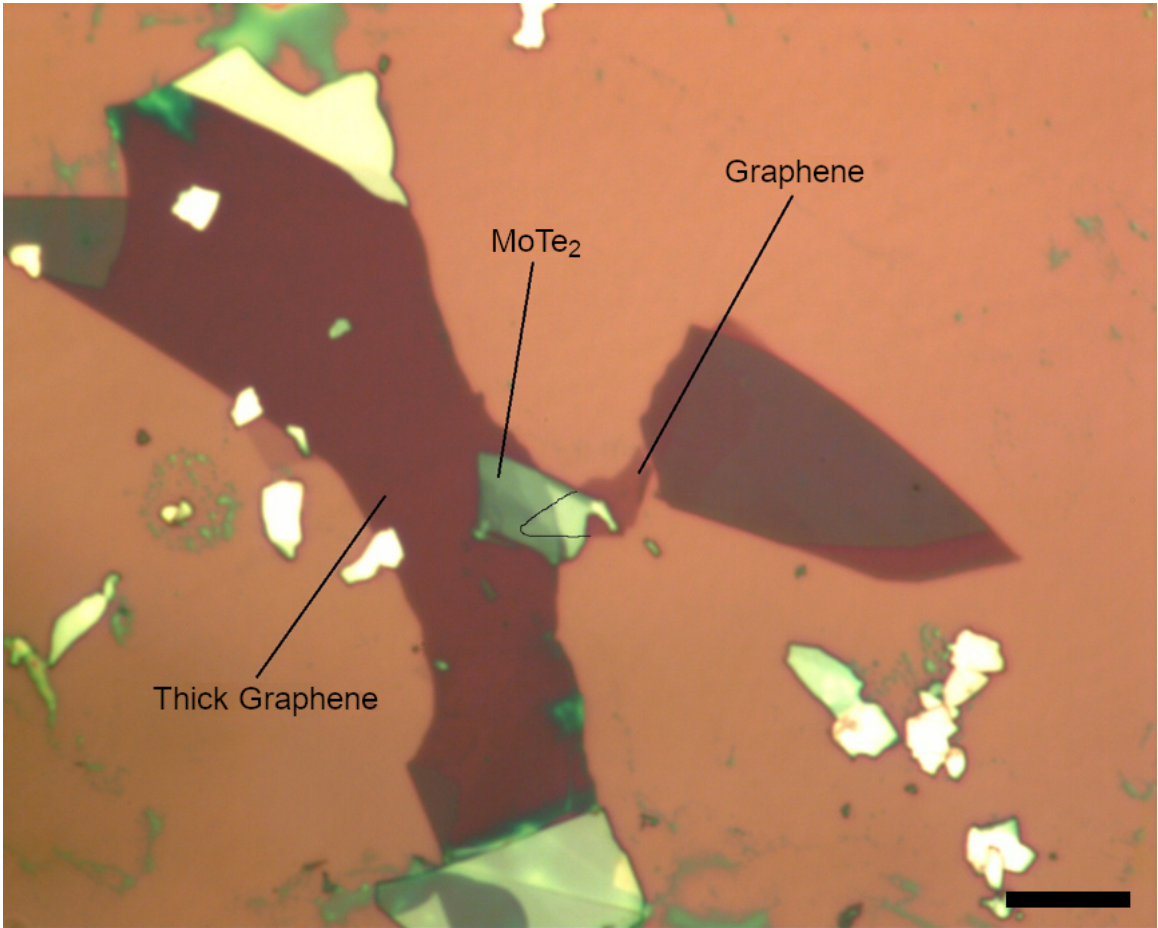


**Figure 3.10:** Optical image of a graphene-MoTe<sub>2</sub>-graphene heterostructure produced by dry transfer using a custom-built transfer microscope, with each layer labelled. Scale bar is 10  $\mu\text{m}$ .

10x, and 20x Olympus objectives. Using this microscope system, we successfully construct graphene-MoTe<sub>2</sub>-graphene heterostructures, as shown in Figure 3.10.

In this section, we illustrate the standard transfer process modified from Gomez *et al.* to construct graphene-MoTe<sub>2</sub>-graphene heterostructures, which is described in detail in Section 3.4.1. We present challenges inherent to this process when creating these

structures and methods to overcome them. In Section 3.4.2, we explain a useful variation to the standard transfer method known as the direct stamp exfoliation technique. We expound on the advantages and limitations of this process relative to the standard method.

### 3.4.1 Dry Transfer: Standard Method

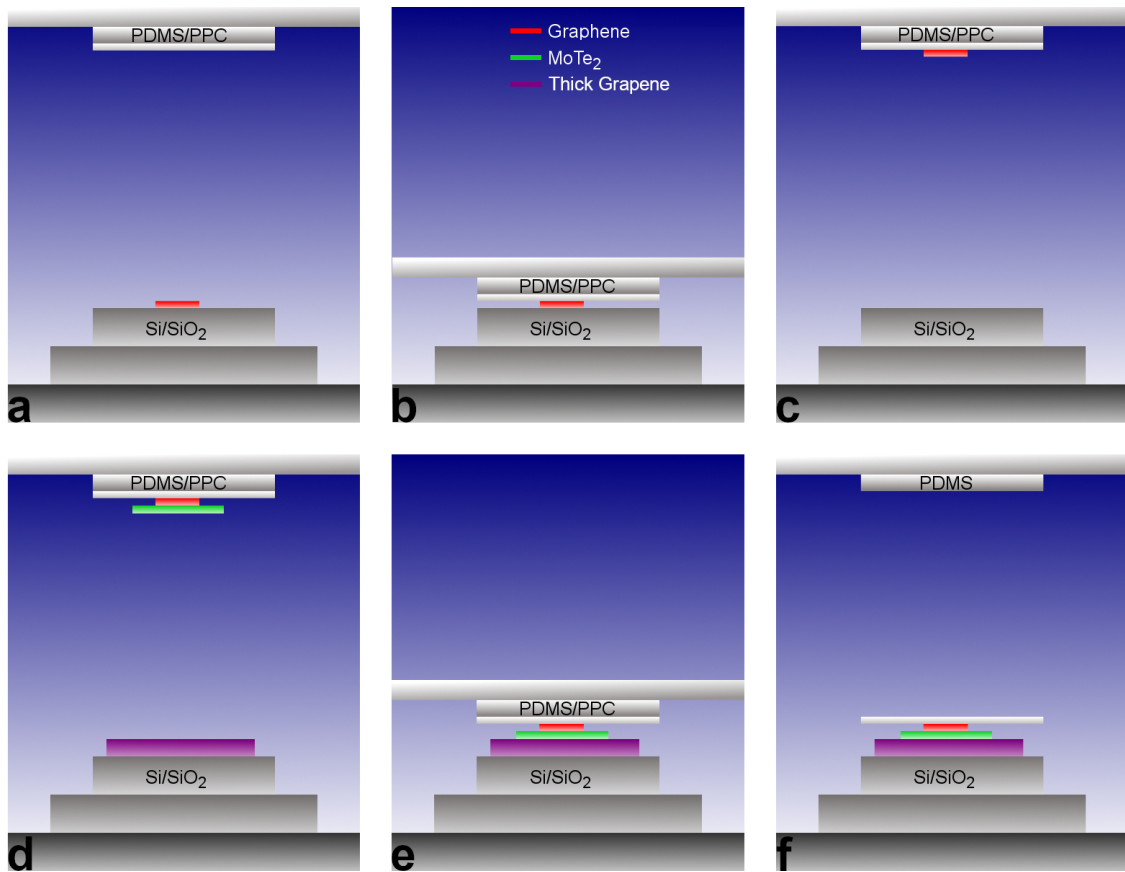


**Figure 3.11:** Schematic of standard method of dry transfer assembly of graphene-MoTe<sub>2</sub>-graphene heterostructures. **(a)** Initially, a graphene flake is placed on the sample stage and a stamp is made consisting of a glass slide, PDMS, and PPC. **(b)** The stamp is lowered until it encounters the graphene on the sample stage. **(c)** After heating the stage to 40°C and allowing it to cool back to room temperature, the stamp is quickly removed from the stage, picking up the graphene flake. **(d)** The same procedure is used to pick up the next layer of MoTe<sub>2</sub>, and then the final layer of graphene is placed on the sample stage. **(e)** The flakes are aligned on top of each other and the stamp is lowered until it contacts the stage. **(f)** The stage is heated to 80°C to melt the PPC layer, and the stamp is

raised slowly to allow the PPC to separate from the PDMS, leaving the completed heterostructure on the desired substrate. The PPC layer is then removed in an acetone bath.

Utilizing our transfer microscope, we assemble graphene-MoTe<sub>2</sub>-graphene heterostructures by successively picking up ultrathin flakes of material and stacking them onto a desired substrate. The step-by-step procedures for carrying this out are depicted schematically in Figure 3.11. As seen in Figure 3.11a, we begin by attaching the PPC/PDMS stamp to the cantilever, and placing a Si/SiO<sub>2</sub> substrate containing a few-layer graphene flake onto the sample stage. We then lower the cantilever such that the stamp fully contacts the graphene flake (Figure 3.11b). By heating the sample stage to 40°C, adhesion between the PPC and the graphene flake is enhanced, such that the graphene preferentially binds to the PPC over the Si substrate underneath. Next, we cool the stage back down to 34°C or below in order to harden the PPC layer. We then rapidly lift up the stamp, picking up the graphene flake with it (Figure 3.11c).

We find this step in the transfer process to be the most difficult practically, since single- or few-layer graphene appears to have poor adhesion to the PPC stamp. Also, when a graphene flake is picked up, there is a high chance it will tear due to its fragile thin structure. Due of these concerns, an alternate method, known as the direct stamp exfoliation method, was devised to improve the transfer of the top graphene flake specifically. We explain this process in greater detail in the next section.

After successful pickup of a few-layer graphene flake, we place another Si/SiO<sub>2</sub> substrate containing an ultrathin flake of MoTe<sub>2</sub> on the sample stage. We then slowly lower the cantilever, aligning the graphene flake on the stamp with the MoTe<sub>2</sub> before bringing the two into contact. After applying the same heating and cooling procedures as

before, we pick up the MoTe<sub>2</sub> flake underneath the graphene by once again rapidly lifting up the stamp (Figure 3.11d). At this point, we place the final substrate containing the bottom thicker graphene layer onto the sample stage, as shown in Figure 3.11d, and prepare to transfer the partially formed structure on the stamp onto this substrate. Once again, we lower the cantilever, aligning the graphene/MoTe<sub>2</sub> structure with the bottom graphene, and we bring the stamp and substrate into contact (Figure 3.11e). For this final transfer step, we heat the sample stage to 80°C, which passes the glass transition temperature of the PPC, causing it to melt. We then raise the stamp very slowly, such that the liquified PPC peels off the PDMS and stays on the substrate (Figure 3.11f). The sample is then washed in an acetone bath for 30 min to 1 hour in order to ensure complete removal of the PPC, leaving behind the completed graphene-MoTe<sub>2</sub>-graphene heterostructure.

Additional challenges occur in the later steps of this process. This include some difficulty in transferring the MoTe<sub>2</sub> layer. As mentioned before, the lattice mismatch between Mo and Te atoms may lead to some structural instability, and we observe that MoTe<sub>2</sub> easily breaks during the transfer process, though it seems to not be as fragile as the top graphene layer. This problem can be ameliorated by selecting MoTe<sub>2</sub> flakes for transfer that don't display any cracks or wrinkles on the surface. Also, during the final transfer stage, slipping of the layers relative to each other can occur, which will change the geometry of the device and potentially make it unusable. This tends to be the result of a slanted interface between the stamp and the substrate, which can be resolved by adjusting the tilt control such that there is no tilt between the two. Even with these

difficulties resolved, the success of the transfer process is highly statistical, requiring many attempts to be made before a suitable structure is obtained.

### ***3.4.2 Dry Transfer: Direct Stamp Exfoliation Method***

Due to the high level of difficulty in transferring the top graphene layer in a graphene-MoTe<sub>2</sub>-graphene heterostructure using the standard method, we developed a new transfer technique known as the direct stamp exfoliation method, which attempts to make transfer of few-layer graphene easier. In this procedure, we utilize the same custom-built transfer microscope, and we construct a stamp in the same manner as in the standard method. We attach the stamp to the cantilever, but this time we initially place a Si/SiO<sub>2</sub> substrate containing a MoTe<sub>2</sub> flake onto the sample stage. We use the same procedures described in the previous section to pick up the MoTe<sub>2</sub> flake and set it down onto another Si/SiO<sub>2</sub> substrate containing a thick bottom graphene layer, removing the PPC layer in acetone once again. The result is a MoTe<sub>2</sub>-graphene heterostructure on the substrate.

A second stamp is then created, consisting of only the glass slide and the PDMS layer. Tape is then used to affix the stamp to the lab bench, with the PDMS side facing up. Using the standard exfoliation technique explained in Section 3.3.1, we exfoliate few-layer graphene directly onto the surface of the PDMS. Afterward, we attach this new stamp to the cantilever in the transfer microscope, and we slowly lower the stamp to align a few-layer graphene flake on the stamp with the MoTe<sub>2</sub>-graphene structure on the sample stage. Then, we simply bring the two into contact and quickly lift up the

cantilever. The graphene flake, without needing any heating step, seamlessly transfers from the stamp to the substrate, completing the graphene-MoTe<sub>2</sub>-graphene heterostructure.

We determine a number of advantages of this technique over the standard transfer method, as well as significant limitations. Few-layer graphene seems to strongly prefer to bind with Si/SiO<sub>2</sub> rather than PDMS. Thus, by excluding the PPC layer on the stamp and using PDMS to directly transfer few-layer graphene, no heat is needed to induce the transfer of graphene from the stamp to the substrate, making graphene transfer much simpler and more reliable. However, the transfer process under this method becomes more time-intensive, requiring an intermediate step of rinsing off a PPC layer, and two stamps must be constructed as opposed to a single stamp in the standard method. Also, the standard method may generate cleaner samples than the direct stamp exfoliation technique. Under the direct stamp exfoliation procedure, the MoTe<sub>2</sub> layer is directly exposed to PPC contaminants, and the top graphene layer is exposed to contamination from bare PDMS. Yet the standard method only exposes the top graphene layer to contamination, leaving the interfaces between layers relatively clean. Because of these considerations, the direct stamp exfoliation transfer method is not clearly superior to the standard technique, and both procedures are used in equal measure to generate graphene-MoTe<sub>2</sub>-graphene heterostructures for the purposes of examining the behavior of highly interacting charge carriers.

### ***3.5 Device Fabrication***

We fabricate optoelectronic devices out of completed graphene-MoTe<sub>2</sub>-graphene heterostructures in order to investigate the properties of highly interacting electrons and holes. We utilize electron beam lithography (EBL) tools in a cleanroom environment to transform a just-transferred heterostructure into a device suitable for measurement. The key procedures and equipment are shown in Figure 3.12. Using DesignCAD 2000 and Nanometer Pattern Generation System (NPGS) software developed by JC Nability Lithography Systems, we design patterns necessary for the lithography process (Figure 3.12a). We then feed these designs into a Leo XB1540 focused ion beam (FIB) milling system, which writes the patterns onto a layer of resist coated on a desired heterostructure



**Figure 3.12:** Essential procedures and equipment for producing graphene-MoTe<sub>2</sub>-graphene optoelectronic devices through EBL. **(a)** DesignCAD 2000 and NPGS design for electrical contacts on a heterostructure device. **(b)** Leo XB1540 focused ion beam milling system, used for pattern writing. **(c)** Temescal BJD 1800 e-beam evaporator, used for metal deposition.

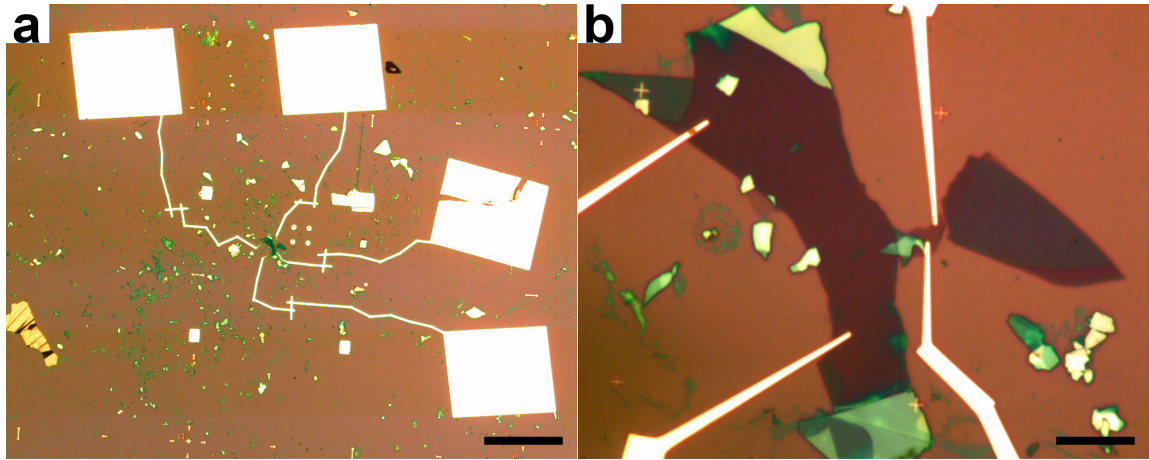


**Figure 3.13:** Optical images of a graphene-MoTe<sub>2</sub>-graphene optoelectronic device under (a) 5x (scale bar is 200  $\mu\text{m}$ ) and (b) 100x (scale bar is 10  $\mu\text{m}$ ) magnification. sample (Figure 3.12b). Afterward, the sample is brought to a Temescal BJD 1800

electron beam (e-beam) evaporator, which deposits metal to fill in the patterns created by the FIB (Figure 3.12c). Through the use of this lithography system, we successfully produce graphene-MoTe<sub>2</sub>-graphene optoelectronic devices, as shown in Figure 3.13.

In this section, we explain the detailed procedures for generating desired heterostructure devices using EBL. In Section 3.5.1, we propose a standard fabrication method that successfully produced the majority of our devices. Despite this, we identify a significant disadvantage of this technique that lead to setbacks in both the fabrication process as well as device performance. In Section 3.5.2, we elucidate an alternative fabrication approach, known as the contact pre-write method, and expound on the ways this method helps overcome the setbacks of the standard fabrication technique.

### ***3.5.1 Standard Fabrication Method***

We utilize two major steps in the standard fabrication procedure of heterostructure devices. First, we write alignment markers onto the sample near the heterostructure, which allows for precise writing of electrical contacts in the subsequent step. To carry out the fabrication of alignment markers, we first take a series of optical images of the heterostructure at 5x magnification. We take a montage of images starting from a corner of the Si chip and moving toward the location of the heterostructure, making sure to keep one side of the corner perfectly straight. We then load these images into a DesignCAD 2000 workspace, aligning each image with the others until we reconstruct a visual map of the sample from the corner to the heterostructure. This allows us to determine the precise distance between the chosen corner and the heterostructure, which will become important later in the process. We then construct a square array of alignment markers consisting of small crosses a few microns long on a side separated from each other by a distance of 40  $\mu\text{m}$ . Every tenth cross in the pattern, however, is a larger cross that is  $\approx 10 \mu\text{m}$  on a side, including the cross at the center of the pattern. Thus, our array consists of a series of both large and small alignment markers, which we use for rough and fine alignment, respectively, of our desired contact pattern. We overlay this alignment pattern onto the optical image of the heterostructure in the CAD file, and note the distance between the corner of the substrate and a small cross near the central large cross. We then set this small cross to be the origin point of the pattern. Since the origin point tends to get overexposed during writing, we choose a small cross for this point rather than the central large cross itself, as this allows us to use this large

cross for actual alignment. We load the completed alignment file into the NPGS software on the FIB machine.

Next, we spin-coat a suitable resist onto the sample in preparation for writing the alignment markers. We first spin-coat a layer of methyl methacrylate (MMA) onto the surface of the sample at 4000 rpm for 40 s with a 1000 rpm/s ramp. Afterward, we heat the sample at 180°C for 10 min to let the polymer set. We then spin-coat a second layer of poly-methyl methacrylate (PMMA) onto the sample using the same parameters, and we heat the sample under the same conditions as well. We utilize a double-layered resist since exposure to the electron beam and developer will cause the MMA layer to undercut relative to the PMMA, leading to more structurally stable contacts. The estimated thickness of both layers is  $\approx 180$  nm.

After coating the sample with resist, we utilize the FIB to write the alignment markers. The use of this machine involves a series of specific steps. First, a small incision is made along one edge of the substrate, cutting through the resist and scratching off part of the SiO<sub>2</sub> layer, which exposes conductive surfaces needed to focus the electron beam. We then load the sample into the main chamber and evacuate it. After sufficient vacuum has been reached, at roughing pump levels, we engage the electron beam in secondary electron mode. We locate the corner of the sample that was used in the design file and rotate the sample such that it's in the proper orientation. We also ensure that one side of the corner is perfectly straight, the same side as in the earlier optical image. Next, we find the scratch mark, and focus the electron beam on a small fleck of unearthed material about 1  $\mu\text{m}$  in size. With the beam focused, we reposition it over the chosen

corner and navigate to the origin point of the alignment pattern. Immediately, we initiate the writing of the markers through the NPGS software in order to minimize overexposure at the origin point.

We then remove the sample from the FIB and develop it using a combination of solutions. We place the sample in a solution consisting of a quarter of isopropyl alcohol (IPA) and three-quarters of methyl isobutyl ketone (MIBK) developer for 70 s, and then quickly transfer it to a solution of IPA for 20 s followed by de-ionized (DI) water for another 20 s. The sample is then dried in N<sub>2</sub> gas. An inspection microscope is used to successful writing of the alignment markers.

As the last step in the fabrication of alignment markers, we bring the sample to an e-beam evaporator for metal deposition. We load the sample into the chamber, and pump down to a pressure less than  $6.5 \times 10^{-6}$  torr. We then deposit successively 10 nm of Ti followed by 70 nm of Au. The Ti forms an adhesion layer to the surface of the Si substrate. Though any material could be used for the alignment markers since they make no contribution to the electrical contact of the device, we utilize Au for its high visibility under an electron beam, and we use Ti simply because this is the adhesion layer used when writing the actual contacts. Ti is preferred for contacts since its work function matches well with that of both graphene and MoTe<sub>2</sub>. After evaporation, we place the sample in an acetone bath for several hours to allow the remaining resist to dissolve. Finally, we rinse the sample to lift off excess Au, leaving behind our completed alignment markers, which we again confirm by inspection under an optical microscope.

Once the alignment markers are produced, we then turn our attention to fabricating the actual contacts of the device. As in the case with the alignment step, we begin by taking a series of optical images of the sample. We take a single large-area, low resolution image at 5x magnification that captures the heterostructure as well as all the alignment markers. We then choose 4 large alignment markers to use for rough alignment, and we take 50x magnification images of these 4 large crosses. Similarly, we choose 4 small markers for fine alignment. We utilize 4 small crosses adjacent to each other that are located next to the heterostructure, in order to maximize alignment fidelity. We take a single 100x magnification image that includes both the heterostructure and the 4 chosen small crosses. In order to make sure all these images are in the same orientation, we initially zoom in to the central large cross and a small cross on its right or left and rotate the image such that these crosses are connected by a straight line. We take all the optical images only after this step.

With these optical images, we load them into another DesignCAD 2000 workspace and align all the images relative to each other. We take samples of large and small cross designs from the alignment CAD file and overlay them carefully onto the chosen large and small crosses in our optical images. We then design the actual contacts to be written onto the heterostructure. Our general design consists of writing four contacts on the top and bottom layers of graphene (two on the top layer and two on the bottom layer). This allows us to measure the interlayer photocurrent across the device, as well as to gain some redundancy in case some contacts prove faulty. We utilize narrow, tapered contacts closest to the heterostructure which are only 200 nm wide at the

narrowest portion (as seen in Figure 3.13b). Each contact terminates at a large square contact pad used for wire-bonding to a chip carrier. After completion of contact design, we choose an origin point for the contact file, typically the central large cross or one of the other large crosses. Since the portion of the contacts closer to the heterostructure needs to be written much more precisely than the large contact pads far away, we break up the CAD file into several files that can be written at various resolutions. Three files are composed from the contact design, and a separate file contains the alignment markers. We then load all of these files into the FIB machine.

After spin-coating resist onto the sample for a second time using the same procedures described earlier, we write contacts using the FIB. We utilize all of the same procedures used in writing the alignment markers up to navigating to the origin point of the alignment markers. At this point, we ensure proper orientation of the sample with our design files by rotating the sample such that the large central cross connects with an adjacent small cross in a straight line, which is exactly the same step we performed to orient the optical images of the sample in the first place. After this, we navigate to the origin point of the contact files, and we run the NPGS software, which performs both rough and fine alignment of the sample before finally writing the contacts.

Once the contacts have been written, we develop them in the same way as for the alignment markers, and we once again bring the sample to the evaporator for metal deposition. We perform the same steps in the evaporator as before, except this time we deposit 4 nm of Ti and 120 nm of Au in order to create thick, strong contacts as well as minimize the amount of Ti to reduce contact resistance. Afterward, we lift off excess

metal in the same manner as before, leaving behind a completed graphene-MoTe<sub>2</sub>-graphene optoelectronic device. Finally, we perform rapid thermal annealing on the device using a RTP-600S annealing system from Modular Process Technology Corp. We anneal samples for 30 min at 250°C in an Ar environment.

This process proves to be largely successful in creating desired heterostructure devices, yet there is a significant drawback, as well. Because of the need for multiple writing steps involving both alignment markers and contacts, significant amounts of solution-based processing of samples is required. We find that under such conditions, the MoTe<sub>2</sub> layer of the heterostructure slowly disintegrates over time. The level of disintegration varies with each sample, and the exact cause of this effect is unknown. This degradation of the MoTe<sub>2</sub> could have unknown negative effects on device performance. Also, in some samples the MoTe<sub>2</sub> dissolves sufficiently enough to render the device unusable by the end of the fabrication process. For these reasons, a novel process known as the contact pre-write method was developed, which alters both the procedures for heterostructure dry transfer as well as device fabrication.

### ***3.5.2 Contact Pre-Write Fabrication Method***

In order to mitigate the effects of MoTe<sub>2</sub> degradation, we devised the contact pre-write fabrication method. In this technique, we first exfoliate ultrathin flakes of graphene and MoTe<sub>2</sub> according to the methods described in Section 3.3. However, in this case, we select a sample containing a suitable bottom graphene layer and write electrical contacts to it before we transfer the remaining layers and construct the heterostructure. This allows all the solution processing of the fabrication process to affect only the bottom

graphene layer. The MoTe<sub>2</sub> layer, then, remains pristine, potentially improving device performance and preventing wasteful fabrication of devices that break down at the end of processing due to extensive MoTe<sub>2</sub> degradation.

To carry out this technique, we first take high resolution optical images of each separated layer of the heterostructure, typically at 50x magnification. We then load these images into a DesignCAD 2000 workspace, and draw line traces around the outlines of the MoTe<sub>2</sub> and top graphene layers. By orienting these traces in a specific manner and overlaying them onto the optical image of the bottom graphene layer, we construct a virtual image of what our desired heterostructure will look like. With this virtual heterostructure, we then proceed to perform all of the same fabrication steps laid out in the standard fabrication method to first write alignment markers onto the sample followed by the electrical contacts. At this point, we then utilize either of the methods mentioned in Section 3.4 to transfer the MoTe<sub>2</sub> and top graphene layers onto the sample, completing the heterostructure and thus the device as a whole. Lastly, we perform the same thermal annealing step as in the standard method. The main additional difficulty of this technique is the extra care needed to precisely align transferred flakes such that they not only overlap the with each other but also with the pre-written contacts. Despite this slight challenge, we find this technique to be both practical and effective in overcoming the MoTe<sub>2</sub> degradation problem inherent to the standard fabrication method. Consequently, the contact pre-write fabrication technique is the main method we use to generate graphene-MoTe<sub>2</sub>-graphene optoelectronic devices for the purpose of studying highly interacting charge carriers.

### ***3.6 Chip Carrier Fabrication***

After obtaining a graphene-MoTe<sub>2</sub>-graphene device, we complete the fabrication process by generating patterned chip carriers that allow connection between the device and the probe arms of our optoelectronic measurement apparatus. We use sapphire as the chip carrier material due of its high thermal conductivity and low electrical conductivity. This unique blend of properties proves particularly useful in our measurement system, described in greater detail in the following section, where we have the ability to cool the sample down to very low temperatures. Because of this, choosing a substrate for chip carriers that can transmit thermal energy efficiently without shorting the system electrically is highly desirable, making sapphire an ideal material for these substrates. Due to geometrical constraints in our measurement system, we use  $\frac{3}{4}$  in square single-side polished sapphire wafers, shown in Figure 3.14a.

We fabricate chip carriers from these sapphire wafers by utilizing standard photolithography techniques. We perform exactly the same photolithography steps with the same parameters as in the fabrication of identifying markers on Si wafers described in Section 3.2. However, after development of the resist, we utilize e-beam evaporation

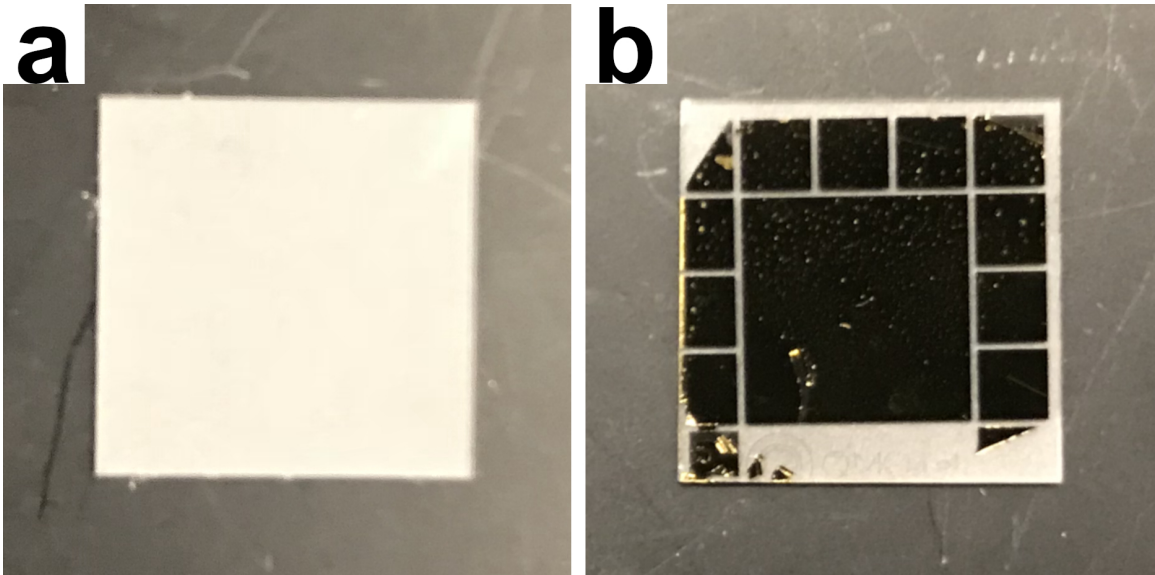


**Figure 3.14:** Optical images of a sapphire wafer **(a)** before and **(b)** after fabrication into a chip carrier for graphene-MoTe<sub>2</sub>-graphene optoelectronic devices.

instead of etching to generate the desired pattern. We execute the same procedures for e-beam evaporation as those described in Section 3.5 to deposit metal onto patterned heterostructure devices. In this case, though, we deposit 10 nm of Ti and 500 nm of Au to provide a thick conductive layer to which contacts may attach. We then perform the same liftoff procedures in acetone, as well.

We design chip carriers to consist of a central square Au pad surrounded by a series of smaller pads, as seen in Figure 3.14b. We place a completed heterostructure device onto the central pad and wire-bond contacts from the surrounding smaller pads to the contacts pads of the device itself. Afterward, the device is ready for measurement, and the probe arms of our measurement apparatus attach to the outer small pads on the chip carrier, completing the circuit from the heterostructure device to our measurement diagnostics. Thus, we generate a device in which we are capable of performing advanced

optoelectronic measurements to investigate the effects of highly interacting charge carriers.

### 3.7 Optoelectronic Measurements

Once we fabricate suitable graphene-MoTe<sub>2</sub>-graphene devices, we measure the optoelectronics of these systems in order to observe the behavior of highly interacting electrons and holes. To accomplish this, we employ a MIRA 900 OPO Ti:Sapphire ultrafast pulsed laser which generates 150 fs pulses with controllable wavelength  $\lambda$  from 1150 nm to 1550 nm at a 75 MHz repetition rate. A schematic of the measurement apparatus and beam paths is shown in Figure 3.15. After the near-infrared beam leaves

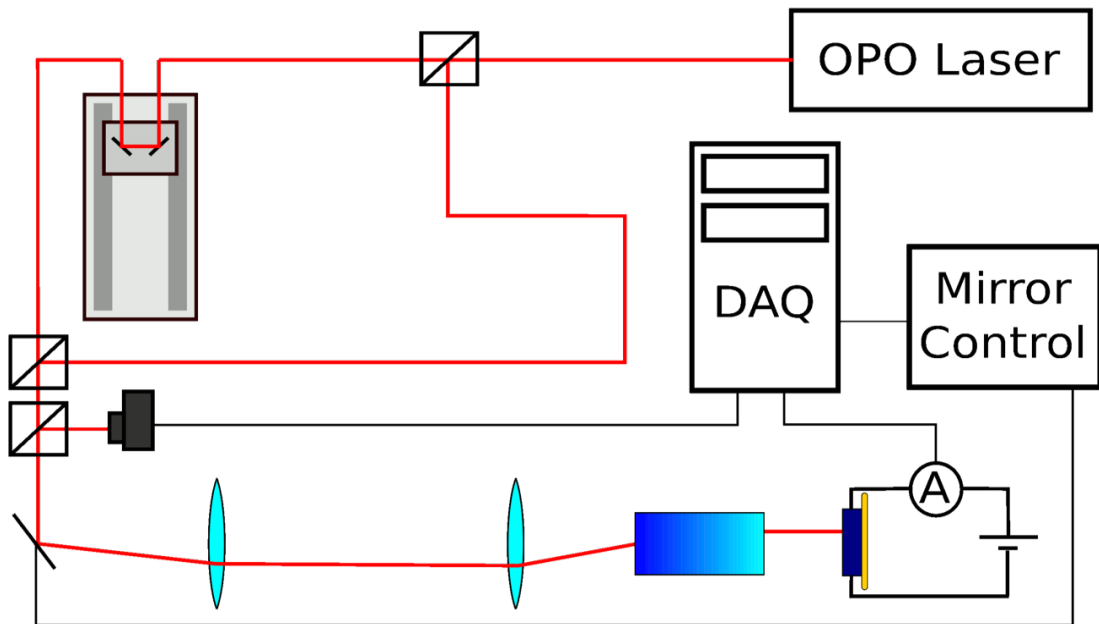


**Figure 3.15:** Schematic of ultrafast pulsed laser system and measurement apparatus.

the OPO, we pass it through a 50/50 beamsplitter, which separates the beam into two distinct branches. One branch of the beam path remains fixed in length while the other passes through a controllable delay stage. Thus, by tuning the delay stage, we produce a controllable time delay  $\Delta t$  between pulses coming from one branch relative to the other. These two branches then recombine at a second 50/50 beamsplitter.

The recombined beam is then fed into scanning beam optics which consist of rotating mirrors and a system of two lenses that focus the beam onto the back of an objective lens. The objective lens is set at the focal length of the second lens such that, as the scanning mirror rotates the beam is still focused onto the same position on the back of the objective, but arriving at a different angle. The objective lens focuses the light down into a diffraction limited beamspot on the sample, where the position of the beamspot depends on the incident angle. As the scanning mirror rotates, the beamspot moves over a wide range of the sample without aberration, allowing for quick high-resolution scanning. We use a gradient index of refraction (GRIN) lens as the objective. A GRIN lens is a single small cylinder of glass in which the index of refraction is continuously varied along the radial and axial directions. Since it lacks the many interfaces of a conventional objective, a GRIN lens does not disperse the laser pulses as dramatically as a traditional objective lens, which makes possible a diffraction limited beamspot.

The sample sits in vacuum on a sample stage inside a customized Janis Research ST-3T-2 optical cryostat, which can vary the temperature from 4 K to 420 K. The sample stage is in the center of a 3 Tesla superconducting magnet, and devices are electronically probed using four probe needles to apply an interlayer bias  $V_i$ . We amplify the electrical

signal and measure the resulting photocurrent. Though we primarily consider the observed photocurrent, we also have the capability to measure the reflectance of the sample by measuring the intensity of the light that is reflected from the sample with a near-infrared photodiode. A data acquisition system (DAQ) both recovers data from our measurements and tunes experimental parameters for further measurements.

With this measurement system, we can explore a wide range of parameter space to examine the optoelectronics of heterostructure devices. By setting a long time delay between pulses such that they don't interact, we are able to perform one-pulse photocurrent measurements. Similarly, we conduct two-pulse photocurrent measurements by setting a short time delay such that the two pulses do indeed interact. Overall, our measurement apparatus allows us to measure the interlayer photocurrent of graphene-MoTe<sub>2</sub>-graphene devices as a function of two dimensions of space, time, interlayer bias potential, temperature, and magnetic field. Therefore, this system provides access to a wide range of experimental knobs relevant to the study of highly interacting charge carriers in ultrathin devices.

### ***3.8 Conclusion***

In this chapter, we discussed a variety of procedures used to successfully fabricate graphene-MoTe<sub>2</sub>-graphene photocells and measure their optoelectronic response. We first explained the process of preparing Si substrates by patterning identifying markers on to the substrate surface to help locate ultrathin flakes of material and performing extensive cleaning procedures. We then described the techniques used to mechanically

exfoliate ultrathin flakes of graphene and MoTe<sub>2</sub>, including the standard exfoliation method, razor method, low angle method, and gold assisted method. The standard method was found to be effective in producing few-layer graphene flakes for the top heterostructure layer as well as thicker graphene flakes for the bottom layer. The razor method was more effective in generating ultrathin TMDs than the standard procedure, yet the low angle and gold assisted methods yielded the best results for ultrathin MoTe<sub>2</sub>.

With the exfoliation of suitable flakes, we described the process of dry transfer to construct a heterostructure using a custom-built microscope system. We presented the standard transfer method as well as the direct stamp exfoliation method for carrying out the transfer process, and showed that they have comparable advantages and disadvantages relative to each other. We then explained the fabrication of optoelectronic devices out of these heterostructures using both the standard method as well as the contact pre-write method, and the contact pre-write method was found to be generally superior to the standard method. The fabrication of chip carriers to connect heterostructure devices to our measurement system was then described in detail. Lastly, we presented our ultrafast pulsed laser system and measurement apparatus, showing that we are able to measure devices across a wide range of parameter space and gain a comprehensive understanding of the device optoelectronics. Through these various techniques, we successfully produce graphene-MoTe<sub>2</sub>-graphene photocell devices and effectively measure their photoresponse, allowing us to probe the behavior of highly interacting electrons and holes.

## CHAPTER 4

### BASIC CHARACTERIZATION OF MoTe<sub>2</sub> PHOTOCELLS

#### **4.1 Introduction**

After fabrication of graphene-MoTe<sub>2</sub>-graphene photocells, we conduct a series of characterization measurements to gain a comprehensive understanding of basic material and device properties before exploring the behavior of highly interacting charge carriers in these devices. In this chapter, we present a variety of characterization data on a specific photocell device, shown in Figures 3.10 and 3.13, used to subsequently investigate interacting carriers in Chapters 5 and 6. We perform atomic force microscopy (AFM) to determine approximate thicknesses of each layer of the photocell as well as confirm device uniformity. We then utilize Raman spectroscopy to provide further characterization of the device, demonstrating consistency with the AFM measurements. Basic  $I$ - $V$  characteristics of the device are also examined. We present laser power dependent  $I$ - $V$  behavior and demonstrate a strong sensitivity in the observed  $I$ - $V$  characteristics to temperature and wavelength. These results are shown to corroborate expected behavior in literature. The results of this work were published in the supplement of Arp, Pleskot *et al.*<sup>33</sup>.

#### **4.2 Atomic Force Microscopy (AFM)**

One technique we employ to understand the material properties of a graphene-MoTe<sub>2</sub>-graphene photocell is AFM. We utilize a Digital Instruments Nanoscope IV

AFM machine that uses a silicon cantilever in tapping mode to determine height profiles of each layer of the device. Figure 4.1b,c,d displays AFM images of portions of the device enclosed by corresponding black-outlined boxes in Figure 4.1a as well as step height profiles along the white solid lines and between the blue crosses in each of the AFM images. From this, we observe that the top graphene, MoTe<sub>2</sub>, and bottom graphene layers display characteristic thicknesses of 5.88 nm, 8.96 nm, and 13.8 nm, respectively. This confirms a top graphene layer that is  $\approx 8$  layers thick, which is thin enough to allow

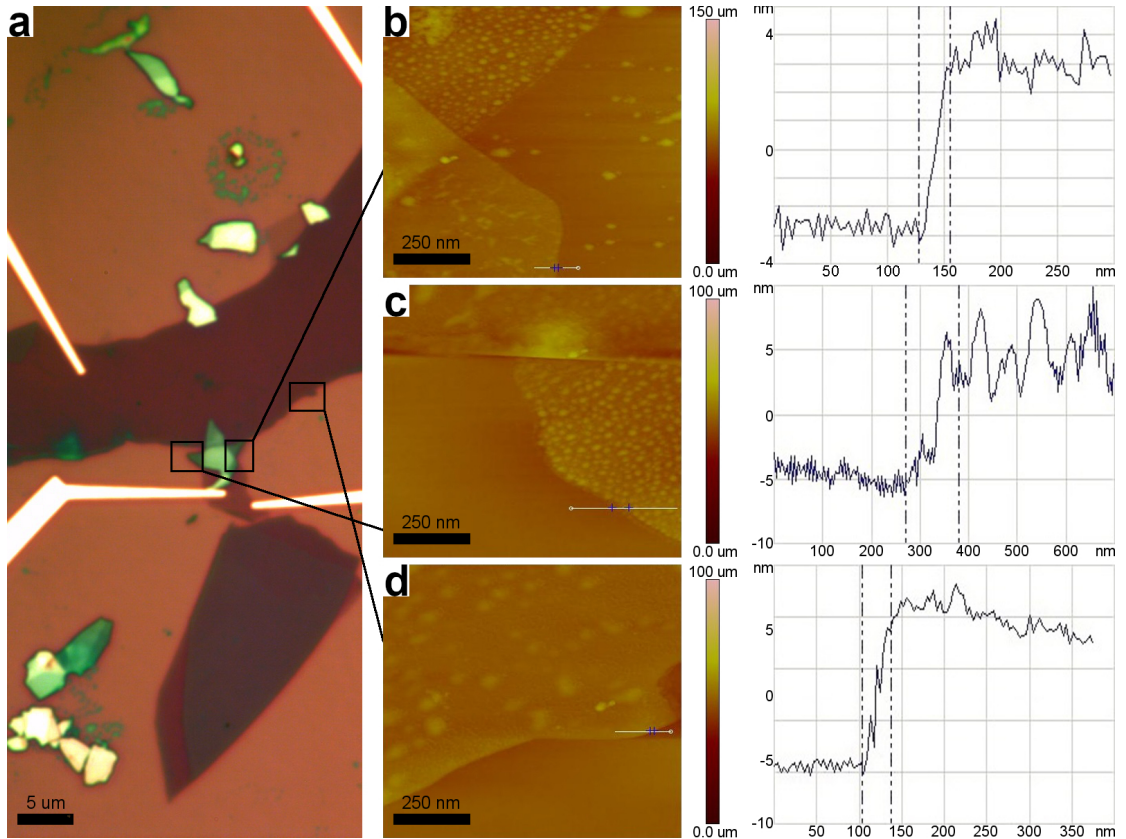


**Figure 4.1:** AFM of a graphene-MoTe<sub>2</sub>-graphene photocell. **(a)** Optical image of the device with boxes indicating areas where AFM scans were taken. **(b), (c), (d)** Left – AFM images of corresponding regions in **(a)**. White solid lines indicate regions where line traces were obtained, and blue crosses indicate the region over which the change in height was calculated. **(b), (c), (d)** Right – AFM line traces corresponding to images on the left.

sufficient light transmission to the MoTe<sub>2</sub> layer to probe highly interacting phenomenon. Contrastingly, the MoTe<sub>2</sub> and bottom graphene layers are substantially thicker, on the order of  $\approx 12$  and  $\approx 20$  layers thick, respectively.

The AFM images also show generally uniform thicknesses without substantial defects in each layer of the device, with a notable exception in the portions of the MoTe<sub>2</sub> layer not covered by the top graphene layer. These regions of the MoTe<sub>2</sub> appears to filled with irregular lumps that may be the result of degradation occurring during device fabrication, as described in Chapter 3. Since this device was fabricated using the standard fabrication method, it is likely that the solution processing steps affected the quality of the exposed MoTe<sub>2</sub>. However, the portion of the device where all three layers overlap displays excellent uniformity, suggesting that the top graphene layer shields the MoTe<sub>2</sub> directly underneath it from the effects of solution processing during the fabrication process. Thus, in the region of the heterostructure overlap where we expect the largest photoresponse, we observe highly uniform surfaces and desired layer thicknesses, confirming that our device is well suited for effectively investigating densely interacting electrons and holes.

### ***4.3 Raman Spectroscopy***

Along with AFM, we utilize Raman spectroscopy for material characterization of graphene-MoTe<sub>2</sub>-graphene photocells. We perform spectroscopic characterization using a Horiba LabRam Raman spectrometer in the backscattering configuration with 20 mW

of laser power at a wavelength of 532 nm, a 100x objective, and a grating with 1800 grooves/mm. Figure 4.2 displays the resulting Raman spectra for each layer of the

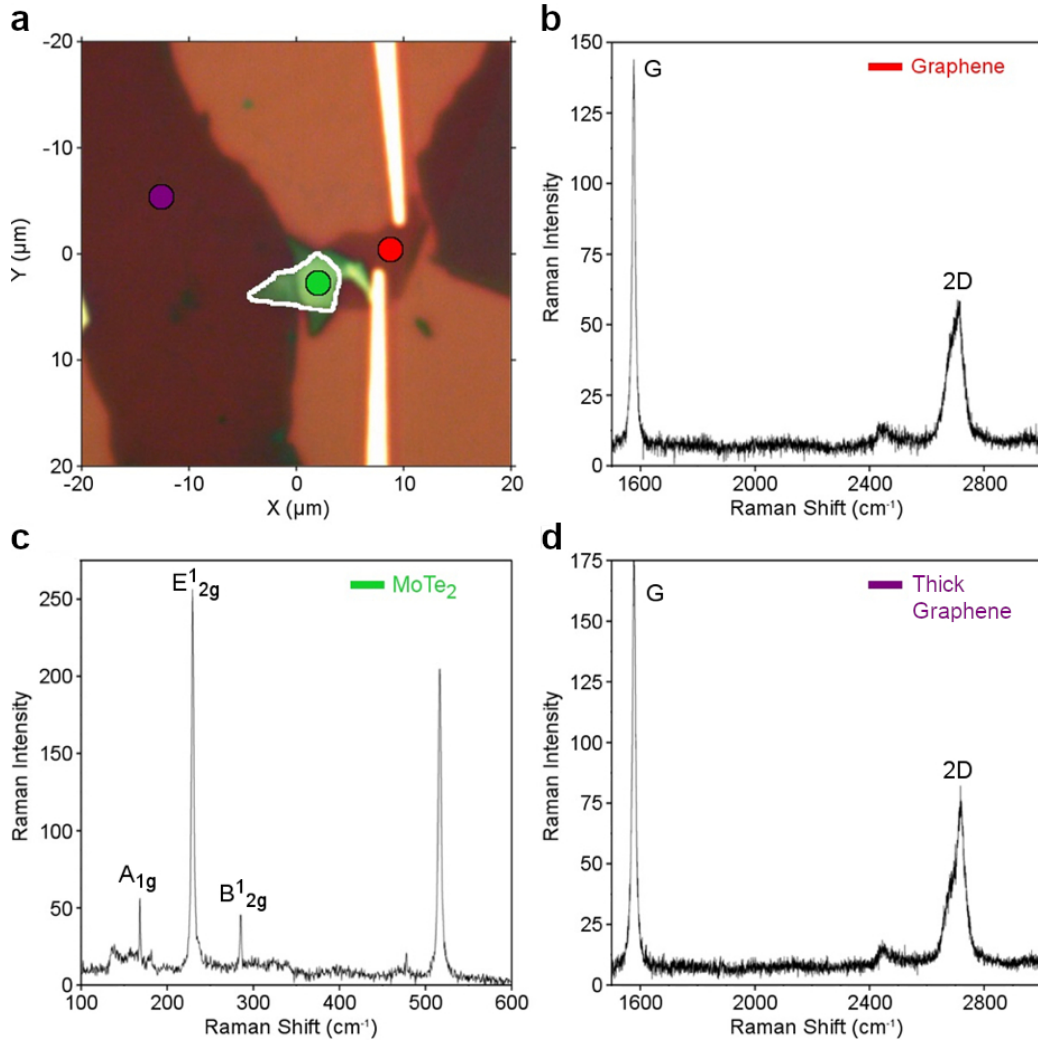


**Figure 4.2:** Raman spectroscopy of a graphene-MoTe<sub>2</sub>-graphene photocell. (a) Optical image of the device with top graphene, MoTe<sub>2</sub>, and bottom graphene layers indicated with color-coded markers. White outline indicates region of 3-layer overlap. (b), (c), (d) Raman spectra of the top graphene, middle MoTe<sub>2</sub>, and bottom graphene layers, respectively, taken at the position of the corresponding markers in (A).

device. For the top graphene layer (Figure 4.2b), we observe the characteristic G and 2D peaks at 1576 cm<sup>-1</sup> and 2716 cm<sup>-1</sup>, respectively. The ratio of the 2D peak to the G peak

can be used as a rough estimate the layer thickness, indicating a thickness of roughly 5-8 layers that is in good agreement with our AFM data<sup>34</sup>.

In Figure 4.2c, we identify the characteristic peaks associated with the MoTe<sub>2</sub> layer in the device<sup>20,22,35,36</sup>. We see the A<sub>1g</sub> peak at 168 cm<sup>-1</sup>, the E<sup>1</sup><sub>2g</sub> peak at 229 cm<sup>-1</sup>, the B<sup>1</sup><sub>2g</sub> peak at 285 cm<sup>-1</sup>, and the Si peak at 517 cm<sup>-1</sup>. In MoTe<sub>2</sub>, layer thickness can be roughly estimated from the ratio of the B<sup>1</sup><sub>2g</sub> to the E<sup>1</sup><sub>2g</sub> peaks<sup>20,22</sup>. With a distinct yet small B<sup>1</sup><sub>2g</sub> peak, we estimate the MoTe<sub>2</sub> layer to be ultrathin but not thin enough to approach the monolayer limit, which agrees qualitatively with the MoTe<sub>2</sub> thickness derived from our AFM results.

Lastly, Figure 4.2d shows the Raman peaks characteristic to the bottom graphene layer in the device. We observe characteristic G and 2D peaks at 1576 cm<sup>-1</sup> and 2717 cm<sup>-1</sup>, respectively, along with a shoulder at 2687 cm<sup>-1</sup>, indicative of thicker, bulk graphene<sup>34</sup>. As before, this result is consistent with our AFM data. Figure 4.2a shows an optical image of the device with color-coded dots designating the locations where Raman data was acquired. Overall, our Raman spectroscopy measurements provide detailed characterization of the Raman vibrational modes and approximate layer thicknesses in the graphene-MoTe<sub>2</sub>-graphene photocell, complementing the AFM results.

#### ***4.4 Power Dependent I-V Measurements***

Beyond examining the material properties of the graphene-MoTe<sub>2</sub>-graphene photocell, we measure the power dependent *I-V* characteristics to gain a basic understanding of the device performance. In order to examine the *I-V* behavior, we place

the photocell into our measurement apparatus and spatially scan the laser across the surface of the device, measuring the photocurrent at each point in space. Figure 4.3a displays a spatial map of the photocurrent corresponding to the region of the device

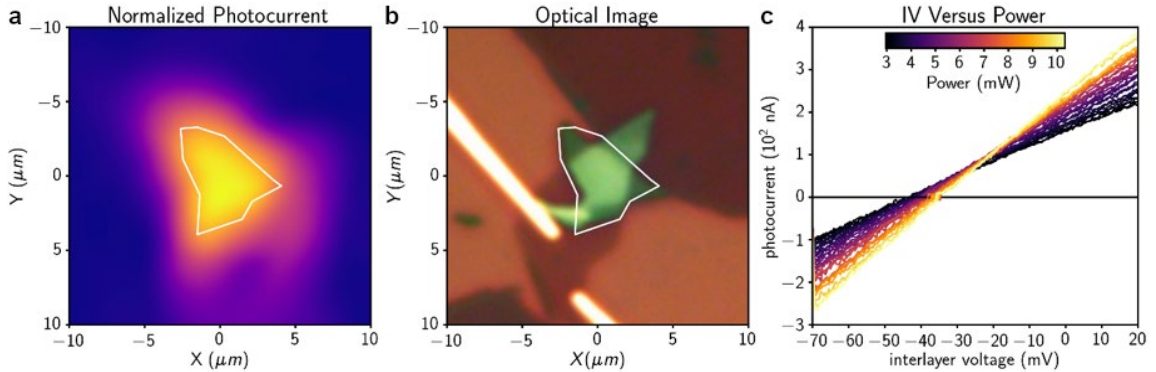


**Figure 4.3:** Optoelectronic  $I$ - $V$  characteristics of a graphene-MoTe<sub>2</sub>-graphene photocell. **(a)** Spatial photocurrent map of device with heterostructure region outlined in white. **(b)** Optical image of region shown in **a** with overlap region outlined in white. **(c)**  $I$ - $V$  curves as a function of laser power. Data taken at room temperature and a laser wavelength of 1200 nm.

shown in Figure 4.3b, with the heterostructure overlap region outlined in white in both images. As expected, the photocurrent is generated primarily in the heterostructure overlap region.

We examine a point in the center of this region and measure the change in photocurrent as we vary the interlayer bias voltage and incident laser power, generating the characteristics shown in Figure 4.3c. The interlayer photocurrent increases linearly with moderate bias voltages, corroborating the results of Pradhan *et al.*<sup>37</sup>. We observe an offset in the zero-crossing of the photocurrent that depends weakly on laser power, indicating the presence of an open-circuit voltage, which has also been reported previously in graphene-MoTe<sub>2</sub>-graphene photocells as well as in other TMDs<sup>29,38,39</sup>.

From Figure 4.3c, we extract an open circuit voltage of  $\phi_0 = -41$  mV for the device. In short, the optoelectronic  $I$ - $V$  measurements of the photocell demonstrate good agreement with previous studies of similar systems, providing a firm basis for our work in earlier reported literature.

#### 4.5 Temperature and Wavelength Dependent $I$ - $V$ Measurements

Additionally, we gain understanding of basic device performance through measuring the temperature and wavelength dependence of the  $I$ - $V$  characteristics. We observe that the photoresponse of the graphene-MoTe<sub>2</sub>-graphene photocell is strongly sensitive to sample temperature, and exhibits behavior consistent with a very lightly doped, indirect gap semiconductor. Figure 4.4a shows a series of  $I$ - $V$  characteristics as a function of temperature. Higher temperature yields significantly more photocurrent, as observed by Lin *et al.*<sup>40</sup>. The photocurrent diminishes with lower temperature since there

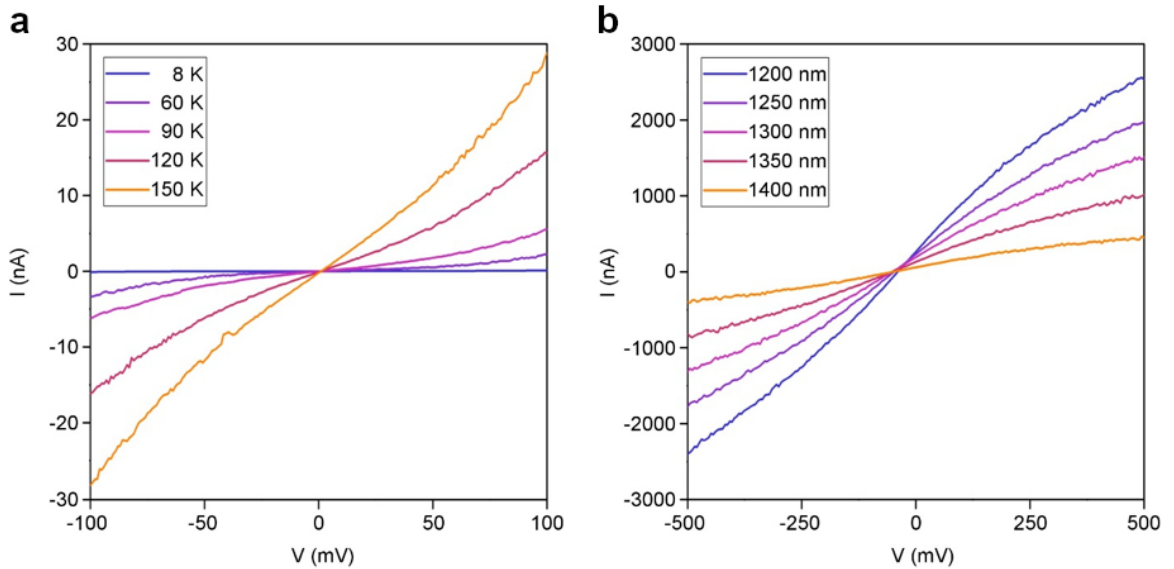


**Figure 4.4:** Temperature and wavelength dependence of  $I$ - $V$  characteristics of a graphene-MoTe<sub>2</sub>-graphene photocell. **(a)**  $I$ - $V$  curves as a function of temperature. Power

= 23.0 mW, Wavelength = 1200nm. **(b)**  $I$ - $V$  curves as a function of incident laser wavelength. Power = 4.80 mW, Temperature = 296 K.

is less thermal energy to excite carriers from the valence to the conduction bands. This behavior suggests that the MoTe<sub>2</sub> is nearly intrinsic, reaching strongly insulating behavior at low temperatures. At higher bias voltages, the photocurrent-voltage characteristics become nonlinear, which is also consistent with previous work<sup>41</sup>. The nonlinear photocurrent response may be due to the presence of Schottky barriers between the MoTe<sub>2</sub> and graphene layers, as reported by Zhang *et al.*<sup>29</sup>.

Wavelength dependent measurements indicate that the highly efficient photoresponse in the photocell occurs only when the incident photon energy  $E_{PH}$  matches the band gap energy of MoTe<sub>2</sub>. Figure 4.4b shows a series of photocurrent-voltage characteristics as a function of wavelength. The photocurrent increases as the wavelength decreases, reaching at maximum photoresponse at  $\lambda = 1200$  nm. As mentioned in Chapter 2, MoTe<sub>2</sub> exhibits a high valence band splitting of roughly 238 meV<sup>23</sup>. Also, MoTe<sub>2</sub> displays two primary absorption peaks corresponding to the A and B excitons at approximately 1.08 eV and 1.425 eV<sup>42</sup>. The strong photoresponse observed here is consistent with the onset of photon absorption at the A exciton band edge in MoTe<sub>2</sub>, which we observe at  $\lambda = 1200$  nm ( $E_{PH} = 1.03$  eV). The weaker photocurrent at longer wavelengths is expected, due to the fact that ultrafast pulsed lasers are far more spectrally broad than continuous wave lasers. Therefore, even significantly off resonance, the exponential tail of the laser spectrum may still overlap the exponential tail of the room temperature exciton absorption spectrum. In summary, the temperature and

wavelength dependence of the photocurrent-voltage characteristics in the graphene-MoTe<sub>2</sub>-graphene photocell exhibit behavior consistent with previous literature. Overall, the I-V characteristics of the device provide a foundation for our work in established literature from which we can confidently explore novel phenomena such as the behavior of highly interacting charge carriers.

#### **4.6 Conclusion**

In this chapter, we conducted a suite of characterization measurements to understand the fundamental material and device properties of a specific graphene-MoTe<sub>2</sub>-graphene photocell. We performed AFM measurements on the device, quantifying the relative thicknesses of each layer of the heterostructure. We verified a top layer of very thin graphene as well as thicker MoTe<sub>2</sub> and bottom graphene layers, confirming that this structure follows our original device design. In addition, AFM images of the heterostructure overlap region demonstrate relatively good surface uniformity, suggesting the device is of sufficient quality to effectively probe the properties of highly interacting electrons and holes. We utilized Raman spectroscopy for further material characterization and determined approximate thicknesses of each layer in the device, which qualitatively agreed with the AFM data. Also, we measured the *I-V* characteristics of the device as a function of incident laser power, temperature, and wavelength. We found that the photocurrent-voltage behavior was highly sensitive to temperature and wavelength, in particular. In general, the *I-V* characteristics corroborated previous findings in literature. As a result of this material and device characterization, we obtain a

thorough understanding of the graphene-MoTe<sub>2</sub>-graphene photocell that paves the way for investigating the effects of highly interacting charge carriers in this device.

## CHAPTER 5

### AUGER RECOMBINATION

#### IN THE EXTREME ELECTRON-HOLE DENSITY LIMIT OF A PHOTOCELL

##### **5.1 Introduction**

Photoexcited electrons and holes in semiconductors lose energy through rapid collisions. The details of such relaxation events - which may include electrons, phonons, or other quasi-particles - reflect the fundamental interactions underlying the electronic properties of solids. Auger recombination is a relaxation process in which an electron and hole recombine in order to transfer energy to a third particle<sup>43,44</sup>. When electrons and holes are unbound, Auger recombination is expected to be a three-particle process. This is the case in conventional electron transport: a free charge carrier collides with an electron-hole ( $e-h$ ) pair, and only one charge carrier escapes.

In low dimensional materials, Auger processes may occur as two-particle processes, and are strongly enhanced compared to bulk materials due to relaxation in momentum conservation and strong spatial confinement<sup>45</sup>. At sufficiently high  $e-h$  pair density, photo-excited  $e-h$  pairs can collide to form short-lived biexcitons - molecular-like complexes of two  $e-h$  pairs bound by the Coulomb force<sup>46-53</sup>. This is in strong contrast to conventional semiconductor materials (e.g., Si and Ge), in which biexcitons are highly unstable and exhibit very low binding energy<sup>54-57</sup>. In the limit that colliding  $e-h$  pairs are strongly bound, Auger recombination is a two-particle process: two  $e-h$  pairs collide, and only one  $e-h$  pair escapes.

Photoexcited electron transport in van der Waals (vdW) heterostructure devices is a powerful tool for the study of strongly interacting electrons and holes, yet the Auger process that is most relevant to optoelectronic transport remains unresolved. Although free electrons and holes mediate charge current (suggesting that 3-particle Auger processes should be important), optical measurements have shown that strong Coulomb interactions result in stable biexcitons<sup>52</sup> and efficient exciton-exciton annihilation<sup>6,8-12,58</sup> (a 2-particle Auger process).

In this chapter, we report on detailed photocurrent measurements of graphene-MoTe<sub>2</sub>-graphene (G-MoTe<sub>2</sub>-G) heterostructure photocells at room temperature and high vacuum (10<sup>-6</sup> Torr). Local infrared pulsed laser excitation ( $\lambda = 1200$  nm) allows us to explore the intricate interdependence of the photocurrent on optical power, interlayer voltage, and time delay between laser pulses. We develop a simple yet comprehensive framework that accounts for the complex photocurrent behavior resulting from ultrashort pulses, and complements strong experimental evidence that 2-particle Auger processes dominate the infrared photoresponse. Utilizing near infrared photoexcitation at low interlayer voltages ( $< 0.1$  V), we access  $e$ - $h$  pair densities reaching 0.1/nm<sup>3</sup> - densities at which the inter-pair spacing approaches the exciton Bohr radius. Our demonstration of vdW heterostructure infrared photocells in the extreme density limit reveals new details about Auger relaxation mechanisms in 2D materials, and heralds a new realm of high  $e$ - $h$  density optoelectronics with relevance to the search for strongly correlated  $e$ - $h$  phases. The main results of this chapter were published in Arp, Pleskot *et al.*<sup>33</sup>.

### 5.2 One-Pulse Measurement: Power Dependence

We consider a graphene-MoTe<sub>2</sub>-graphene photocell (Figure 4.3b) constructed from exfoliated crystals using a deterministic dry transfer heterolayer stacking method, described in Chapter 3. We utilize a near-infrared ultrafast pulsed laser to excite electrons and holes in the MoTe<sub>2</sub> layer and measure the interlayer photocurrent (Chapter 3). By spatially scanning the laser across the surface of the sample, we produce spatial

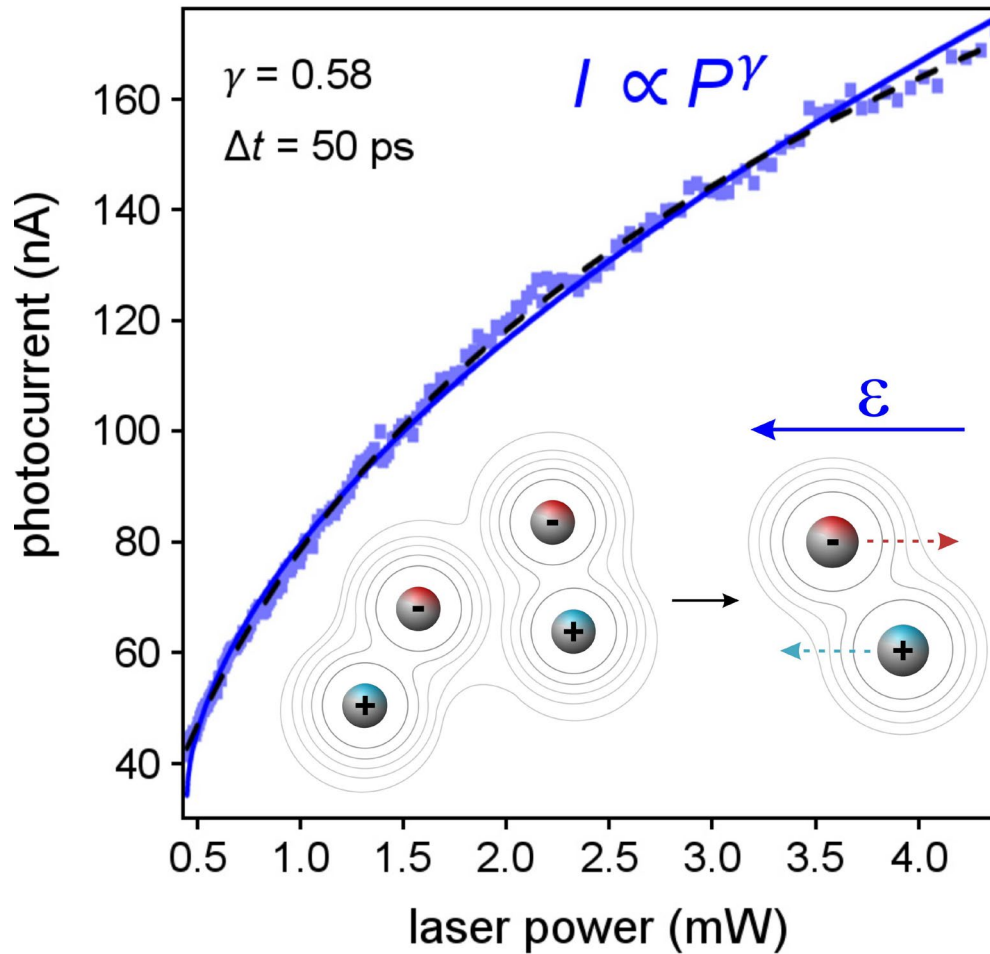


**Figure 5.1:** One-pulse photocurrent vs. optical power taken at a point in the center of the heterostructure (blue data). Solid blue line denotes the power law fit. Black dashed line

shows the predicted power dependence of the photocurrent from the model. Inset, 2-particle Auger recombination results in one electron and one hole, which are swept away in the electric field  $\varepsilon$ . photocurrent maps (Figure 4.3a) and observe that the center of the sample, where all three layers of the heterostructure overlap, generates the most photocurrent. We then fix the laser on the vdW heterostructure photocell and measure the one-pulse infrared photocurrent as a function of laser power (Figure 5.1). We observe sublinear power dependence for  $\Delta t = 50$  ps, consistent with previous measurements of G-TMD-G heterostructure photocells<sup>5,38,59</sup>. The power dependence is accurately described using a power law relationship,  $I \propto P^\gamma$ , where  $\gamma = 0.58$  quantifies the degree of nonlinearity of the laser power dependence.

Interestingly, a power law exponent  $\gamma \approx 1/2$  suggests straightforward dynamics of a non-thermalized  $e$ - $h$  density evolving according to the rate equation

$$\frac{dN}{dt} = -\frac{N}{\tau_{es}} - \alpha N^2 \quad (7)$$

where  $N$  is the  $e$ - $h$  pair density,  $\tau_{es}$  is the carrier escape time, and  $\alpha$  is the rate of 2-particle ( $N^2$ ) electron-hole pair interactions<sup>6,8-12,52-53,58</sup>. By including a constant generation rate, and counting both the electrons and holes that escape the device in an electric field, the steady state ( $dN/dt = 0$ ) solution to Equation (7) results in photocurrent  $I \propto P^{1/2}$ , in good agreement with the observed  $I \propto P^{0.58}$ . The details of this calculation are described in the supplementary materials of Arp, Pleskot *et al.*<sup>33</sup>.

### ***5.3 Two-Pulse Measurement: Temporal Dependence***

Importantly, two-pulse photocurrent measurements reveal that the nonlinearity  $\gamma$  depends strongly on  $\Delta t$  and approaches  $\gamma = 1/2$  only at long time delay. Figure 5.2a shows several example traces of the two-pulse photocurrent vs.  $\Delta t$  for increasing laser power.

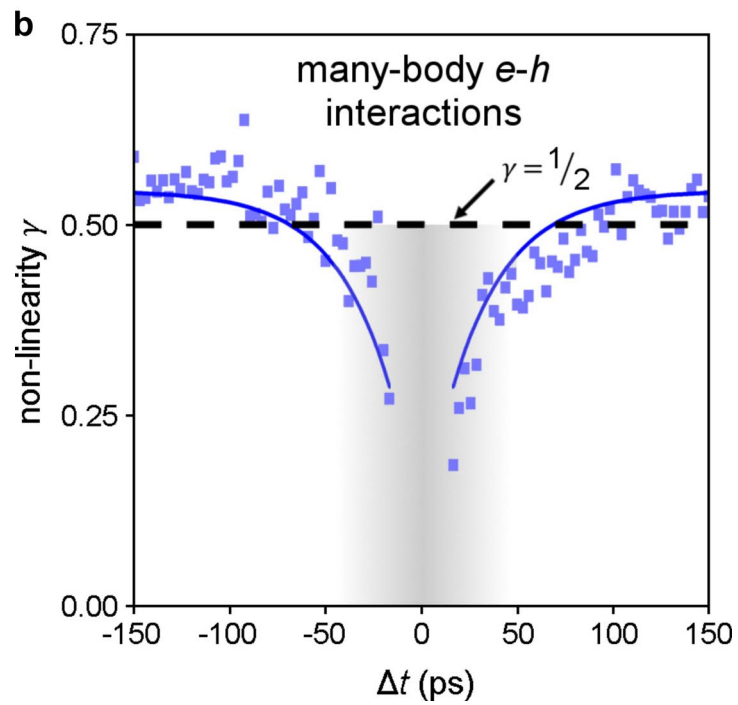
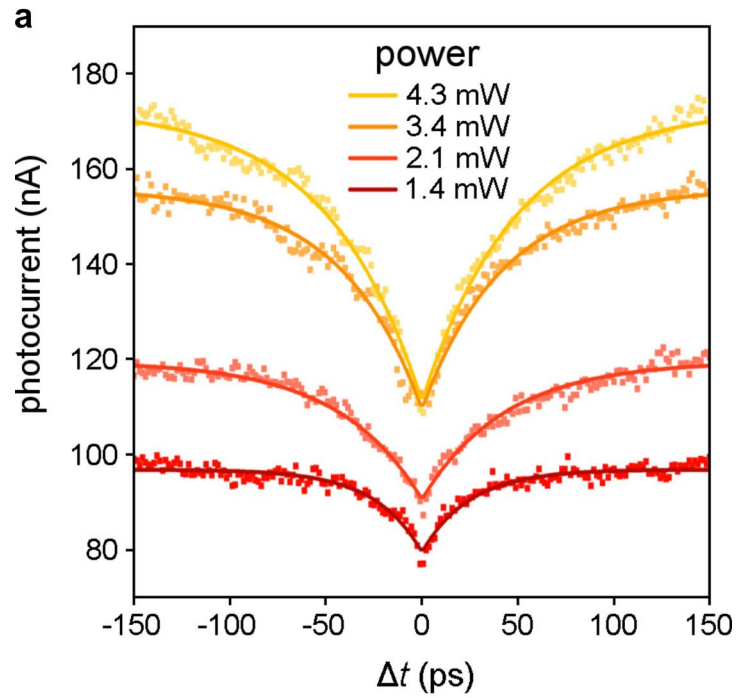


**Figure 5.2:** Dynamic photoresponse measurements of the vdW heterostructure photocell. **(a)** Example two-pulse photocurrent vs. time delay as a function of total (two-pulse) power. Solid lines represent exponential fits to the data. **(b)** Non-linearity  $\gamma$  vs. time delay (blue data). Solid blue lines represent an exponential fit to the data with a characteristic time constant of  $\tau = 29.8$  ps. Black dashed line highlights  $\gamma = 0.5$ . The two-pulse photocurrent is strongly suppressed near  $\Delta t = 0$  ps, where the two pulses overlap, but increases rapidly as the pulses become well separated ( $\Delta t > 50$  ps). As the optical power is increased, the photocurrent vs.  $\Delta t$  characteristics increase in magnitude, yet exhibit exponential decay (solid lines in Figure 5.2a) over comparable time scales ( $\sim 40$  ps).

From a dense data set of two-pulse photocurrent measurements, we are able to extract  $\gamma$  for each value of  $\Delta t$  by fitting the photocurrent vs. power to  $I \propto P^\gamma$  (Figure 5.2b). We find that  $\gamma$  vs.  $\Delta t$  exhibits two distinct regimes of behavior. At short time delay,  $|\Delta t| < 50$  ps,  $\gamma$  decreases significantly and the photocurrent power dependence is no longer described by a simple power law. In this regime (grey region in Figure 5.2b), strong sublinear photoresponse ( $\gamma \ll 1$ ) is a signature of highly interacting electrons and holes<sup>60</sup>. At long time delay, photocurrent increases sublinearly with power and exhibits a characteristic exponent  $\gamma = 0.54$ .

#### **5.4 Model: 2-Particle Auger Recombination**

We attribute the power law behavior  $I \propto P^{1/2}$  in the G-MoTe<sub>2</sub>-G photocells to 2-particle Auger annihilation: nonradiative decay of one  $e$ - $h$  pair provides excess kinetic energy to the second  $e$ - $h$  pair (Figure 5.1 inset). After optical excitation by an ultrashort pulse, electron-hole pairs in MoTe<sub>2</sub> form a high-density gas of interacting charge carriers<sup>52</sup>. In the absence of an electric field, photoexcited electrons and holes dwell

within the junction sufficiently long ( $< \tau_{es}$ ) to allow for two-body electron-hole annihilation. At finite electric field  $|\mathcal{E}| > 0$ , dissociated electrons and holes transit the device and are collected at the graphene contacts<sup>5,38,59</sup>. Due to Coulomb and phonon-

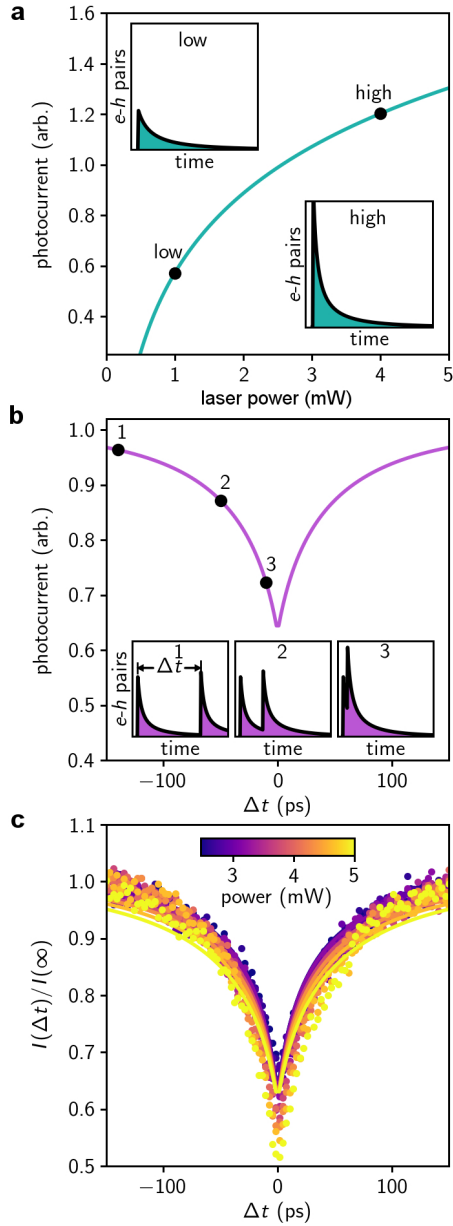


**Figure 5.3:** Two-particle electron-hole recombination model and comparison to infrared photocurrent in the G-MoTe<sub>2</sub>-G photocell. The solution of Eqn. 7 for a single laser pulse as a function of laser power (Eqn. 9) (a) and for two pulses as a function of two pulse

time delay,  $\Delta t$  (Eqn. 8) **(b)**. The photocurrent is proportional to the integral of the number of  $e$ - $h$  pairs versus time, shown in the insets, which is initially driven to a maximum value proportional to laser power, then exponentially decays. **(c)** Normalized photocurrent vs.  $\Delta t$  as a function of power (data) fitted to the model (solid lines), values for model parameters are extracted from these fits (supplementary materials of Arp, Pleskot *et al.*<sup>33</sup>). All calculations in **a** and **b** use these values.

mediated scattering, free electrons and holes escape with velocity  $v = \mu E = \mu \frac{2(V_i - \phi_0)}{L}$ , where  $\mu$  is the mobility,  $L$  is the MoTe<sub>2</sub> thickness, and  $\phi_0$  is the built-in potential ( $\phi_0 = -41$  mV for device shown in Figures 5.1 and 5.2). The time required for liberated charge carriers to escape the photocell junction  $\tau_{es}$  can be tuned by the interlayer voltage<sup>5</sup>  $\tau_{es} = L^2/4\mu(V_i - \phi_0)$ .

In our measurements, the dynamic competition between two-body electron-hole annihilation and charge carrier escape in the vdW heterostructure photocell is revealed in the infrared photocurrent - the average number of charge carriers collected per unit time. The number of  $e$ - $h$  pairs generated by the first laser pulse  $N_1$  increases with optical power (Figure 5.3a). The time dependent  $e$ - $h$  density  $N(N_1, t)$  then decays rapidly (Figure 5.3a insets) according to the integrated Equation (7):  $N(N_1, t) = N_1 e^{-t/\tau_{es}}/[1 + N_1 \alpha \tau_{es}(1 - e^{-t/\tau_{es}})]$ . When a second pulse arrives - delayed by  $\Delta t$  - newly excited  $e$ - $h$  pairs combine with those excited by the first pulse (Figure 5.3b). The photocurrent counts the number of carriers that escape the photocell on a timescale much slower than  $\tau_{es}$ , and is determined by the time-integrated dynamics of both pulses (Figure 5.3b inset) (supplementary materials of Arp, Pleskot *et al.*<sup>33</sup>). The two-pulse photocurrent  $I_{II}(\Delta t)$  is then written as:

$$I_{II}(\Delta t) \propto \frac{1}{\alpha\tau_{es}} \ln[1 + N_1\alpha\tau_{es}(1 - e^{-\Delta t/\tau_{es}})] + \frac{1}{\alpha\tau_{es}} \ln(1 + N_2\alpha\tau_{es}) \quad (8)$$

where the  $e$ - $h$  population following the second pulse is  $N_2 = N_1 + N(N_1, \Delta t)$  (shown in Figure 5.3b). When the delay time is much longer than the escape time ( $\Delta t \gg \tau_{es}$ ),

Equation (8) reduces to the one-pulse photocurrent  $I_I$ :

$$I_I \propto \frac{1}{\alpha\tau_{es}} \ln(1 + N_1\alpha\tau_{es}) \quad (9)$$

as shown in **Figure 3a**.

The 2-particle electron-hole recombination model exhibits excellent qualitative and quantitative agreement with the time-resolved photoresponse of the G-MoTe<sub>2</sub>-G photocell. At long  $\Delta t$ , Equation (8) indicates that the two-pulse photocurrent is twice that of a single ultrafast pulse  $I_{II} \approx 2I_I$ . By normalizing  $I_{II}(\Delta t)/2I_I$ , the two-pulse photocurrent should collapse at long time delays and be nearly independent of laser power. Figure 5.3c shows that the measured interlayer photocurrent indeed collapses when normalized by the photocurrent at  $\Delta t \rightarrow \infty$  (obtained through fitting to exponential decay). Moreover, by fitting Equation (8) to the data (solid lines Figure 5.3c), we determine  $\alpha = (5.62 \pm 0.52) \times 10^{-5} \text{ cm}^2/\text{s}$  and the escape time at zero applied voltage  $\tau_{es}^0 = 86 \pm 2 \text{ ps}$  (supplementary materials of Arp, Pleskot *et al.*<sup>33</sup>).

This model also makes a number of predictions that can be compared to experiment. Under photo-excitation, the interlayer voltage balances the build-up of strongly interacting  $e$ - $h$  pairs with the escape of liberated charge carriers. At low  $V_i$ , electrons and holes dwell in the junction sufficiently long to establish extremely high  $e$ - $h$

pair densities. At sufficiently high interlayer voltage, charge carriers may escape faster than the delay time between pulses  $\Delta t > \tau_{es}$ .

### ***5.5 Testing the Model: Bias Dependent Measurements***

We conducted detailed voltage dependent measurements to test these conjectures. Figures 5.4a and 5.4b show the infrared photocurrent vs.  $V_i$  and laser power  $P$ , taken as snapshots (fixed  $\Delta t$ ) from a sequence of time-resolved photocurrent measurements. At short time delay  $\Delta t = 5$  ps (Figure 5.4a), photocurrent increases with increasing power and voltage (horizontal line traces Figure 5.4c). At  $\Delta t = 50$  ps (Figure 5.4b), the photocurrent behaves similarly, yet with larger magnitude at high interlayer voltage (horizontal line traces Figure 5.4d). Over the entire measured range of  $V_i$  and  $\Delta t$ , photocurrent increases sublinearly ( $\gamma < 1$ ) with increasing optical power.

The effects of applied interlayer voltage become clearer when examining the nonlinearity  $\gamma$  at several values of  $\Delta t$  (Figure 5.4e). The  $\gamma$  vs.  $V_i$  characteristics increase monotonically with voltage at all time delays. As  $\Delta t$  increases,  $\gamma$  increases less steeply with interlayer voltage, and is bounded from above by  $\gamma \approx 1/2$ , (grey bar Figure 5.4e). Importantly, the  $\gamma$  vs.  $V_i$  characteristics extrapolate to an approximately fixed value at  $V_i^* - \phi_0 = 160$  mV, where the nonlinear photoresponse  $I \propto P^{1/2}$  is independent of  $\Delta t$ .

The convergence of the photocurrent power dependence toward a simple behavior  $I \propto P^{1/2}$  highlights a key feature of 2-particle Auger photoresponse: Coulomb interactions in atomically thin MoTe<sub>2</sub> are sufficiently strong to form short-lived bound biexciton states even in the presence of an electric field. By expanding Equation (9) in small order, we find that  $I_1$  reproduces the steady state form  $I \propto P^{1/2}$  (supplementary

materials in Arp, Pleskot *et al.*<sup>33</sup>). Moreover, the analytic expression for  $I_I$  (black dashed line Figure 5.1) exhibits excellent agreement with the one-pulse photocurrent power dependence at  $\Delta t = 50$  ps (blue data) and the power law fit (solid blue line). When  $\Delta t >$

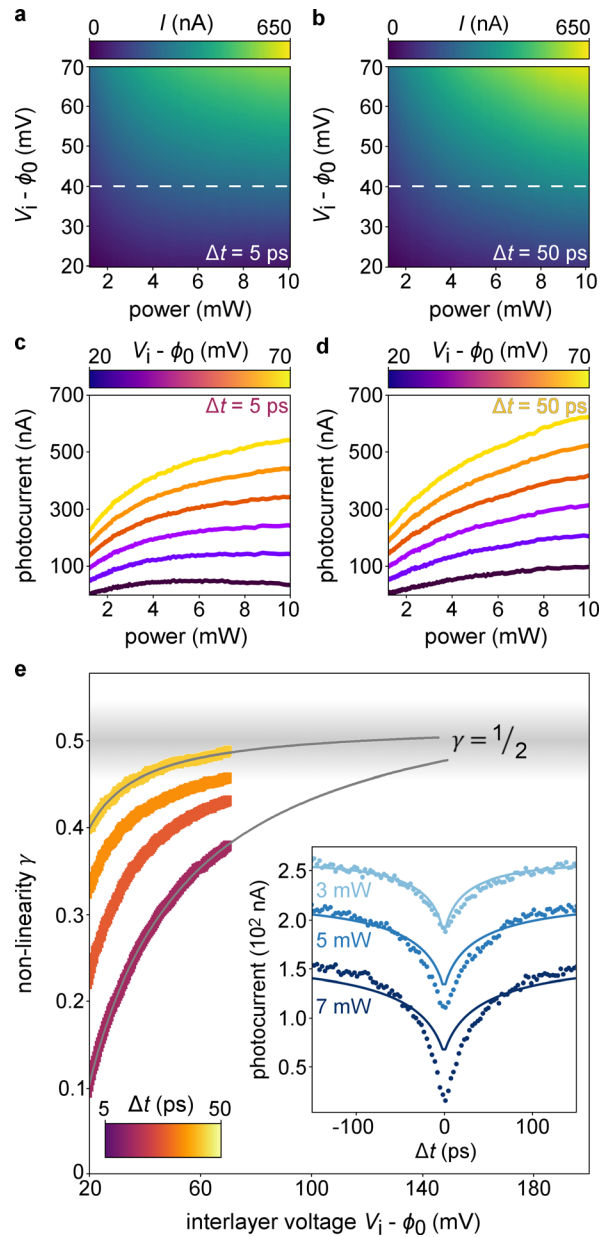


**Figure 5.4:** Interlayer voltage control of the competition between Auger recombination and charge carrier escape in the vdW heterostructure photocell. Photocurrent vs. optical power and interlayer voltage for time delay,  $\Delta t = 5$  ps (a) and 50 ps (b). White dashed lines represent line traces of photocurrent vs. power taken at a specific voltage from these

datasets. Photocurrent vs. power as a function of interlayer voltage for time delay = 5 ps **(c)** and 50 ps **(d)**. **(e)** Non-linearity  $\gamma$  vs. interlayer voltage as a function of time delay. Solid grey lines denote rational fits of the data extended to 160 mV. Inset, photocurrent vs. time delay as a function of power, offset for clarity. Solid lines indicate fits from the model used to extract parameters  $\alpha$  and  $\tau_{es}$ .

$\tau_{es}$ , the G-MoTe<sub>2</sub>-G photoresponse exhibits highly nonlinear power dependence due to biexciton formation, and is described by 2-particle Auger recombination photoresponse Equation (9).

The interlayer voltage in the vdW heterostructure photocell gives precise control over the rate of charge carrier escape, thus allowing us to infer the 2-particle  $e$ - $h$  pair Auger rate  $\tau_{XX}^{-1}$ . When the interlayer voltage  $V_i = V_i^*$ , the internal electric field is sufficient to dissociate electron-hole pairs into free charge carriers. The charge carrier escape rate  $\tau_{es}^{-1}$  then becomes comparable to the rate of 2-particle Auger recombination in the junction. The 2-particle electron-hole annihilation model gives the dissociation rate  $\tau_{XX}^{-1} = (V_i^* - \phi_0)/(\tau_{es}^0 \phi_0)$  in terms of the escape time  $\tau_{es}^0$ . The inferred rate  $\tau_{XX} \approx 20$  ps indicates that, at low electric fields, 2-particle Auger recombination can occur before electrons and holes are able to escape the MoTe<sub>2</sub>. The resulting interlayer photocurrent Equation (9) then accounts for the  $e$ - $h$  pairs lost through annihilation.

By decreasing the interlayer voltage, the infrared G-MoTe<sub>2</sub>-G photoresponse provides access to short-lived, yet extremely high electron-hole density. At very high power ( $P > 5$  mW), the photocurrent vs  $\Delta t$  characteristics begin to deviate from 2-particle Auger photoresponse (Figure 5.4e inset), particularly at short  $\Delta t$ . This behavior is not a permanent change of device response. Instead, we observe this deviation only at short time delay, while the ordinary photoresponse is recovered as soon as the laser intensity is

reduced. At the breakdown of 2-particle Auger photoresponse ( $P = 5$  mW), as  $\Delta t \rightarrow 0$  we estimate that the average spacing between  $e$ - $h$  pairs in MoTe<sub>2</sub> is  $a_{xx} \approx 1$  nm (supplementary materials in Arp, Pleskot *et al.*<sup>33</sup>). When the two laser pulses overlap with sufficient power,  $a_{xx}$  approaches the exciton Bohr radius  $a_B = 2.3$  nm<sup>61</sup>, and the density reaches  $> 0.5$   $e$ - $h$  pairs/nm<sup>3</sup> (supplementary materials in Arp, Pleskot *et al.*<sup>33</sup>). The very high  $e$ - $h$  pair density estimated here - which represents the upper limit of  $e$ - $h$  density - agrees well with that at the onset to giant band gap renormalization and population inversion in WS<sub>2</sub><sup>13</sup>.

## 5.6 Conclusion

The results of this chapter suggest that infrared vdW photoresponse in the presence of extremely high  $e$ - $h$  density may make possible quantum optoelectronic nanotechnologies that harness strongly interacting  $e$ - $h$  pairs, yet differs from traditional semiconductor photoresponse in several important ways. First, in the G-MoTe<sub>2</sub>-G photocell, we observed 2-particle Auger recombination at room temperature. In conventional semiconductors such as Si and Ge, the biexciton binding energy is much less than the thermal energy at room temperature ( $k_B T_{300K} \sim 26$  meV). In standard optoelectronic devices, biexcitons are thus stable only at very low temperatures<sup>54-57</sup> and do not affect the photoresponse. Second, the prevalence of 2-particle Auger recombination in the photoresponse of ultrathin MoTe<sub>2</sub> reflects the unusually large Coulomb field strength in TMDs. As  $a_{xx}$  approaches  $a_B$ , excitons and biexcitons may become unstable due to strong electron-electron interactions between closely packed

electrons and holes. Such interactions may give rise to many-body electronic phases like the exciton condensate or electron-hole liquid<sup>15,60</sup>. Extremely high  $e$ - $h$  pair densities, when combined with strong Coulomb interactions, suggest that vdW heterostructures are highly favorable candidates for room temperature devices that employ collective electronic phases.

## CHAPTER 6

### ELECTRON-HOLE LIQUID IN A VAN DER WAALS HETEROSTRUCTURE PHOTOCELL AT ROOM TEMPERATURE

#### **6.1 Introduction**

In semiconductors, photoexcited charge carriers exist as a gas of free electrons and holes, bound electron-hole pairs (excitons), biexcitons, and trions (charged excitons)<sup>24,62-64</sup>. Remarkably, at sufficiently high electron-hole ( $e-h$ ) densities or low temperatures, the non-equilibrium  $e-h$  system may undergo condensation into an electron-hole droplet<sup>15,17,60,65-67</sup>. Negatively charged electrons ( $e^-$ ) and positively charged holes ( $h^+$ ) merge to become an electronic liquid. In this chapter, we report on the gas-to-liquid phase transition of electrons and holes in ultrathin molybdenum ditelluride photocells revealed through ultrafast photocurrent measurements. By combining rich visualization with comprehensive analysis of very large data sets acquired through these measurements, we find that ultrafast laser excitation at a graphene-MoTe<sub>2</sub>-graphene interface leads to the abrupt formation of ring-like spatial patterns in the photocurrent response as a function of increasing optical power at  $T = 297$  K. The sudden onset to these patterns, together with extreme sublinear power dependence and picosecond-scale photocurrent dynamics, provide strong evidence for the formation of a two-dimensional electron-hole liquid droplet. The electron-hole liquid, which features a macroscopic population of correlated electrons and holes, may offer a path to room temperature

optoelectronic devices that harness collective electronic phenomena. The main results of this work were published in Arp, Pleskot *et al.*<sup>33</sup>.

### 6.2 Multi-Parameter Photocurrent Imaging

We probe the optoelectronic response of a fabricated graphene-MoTe<sub>2</sub>-graphene photocell (Figure 4.3b) using an ultrafast pulsed laser system (Chapter 3). By spatially scanning the laser across the surface of the sample and measuring the interlayer photocurrent at each point, we generate spatial photocurrent maps used to analyze the photoresponse of the device (Figure 4.3a). Through tuning other parameters in this measurement apparatus, we acquire a multi-dimensional data set of interlayer photocurrent  $I$  vs. two spatial dimensions, laser power  $P$ , time delay  $\Delta t$ , and interlayer voltage  $V_i$ . Using this measurement system, we gain a comprehensive understanding of

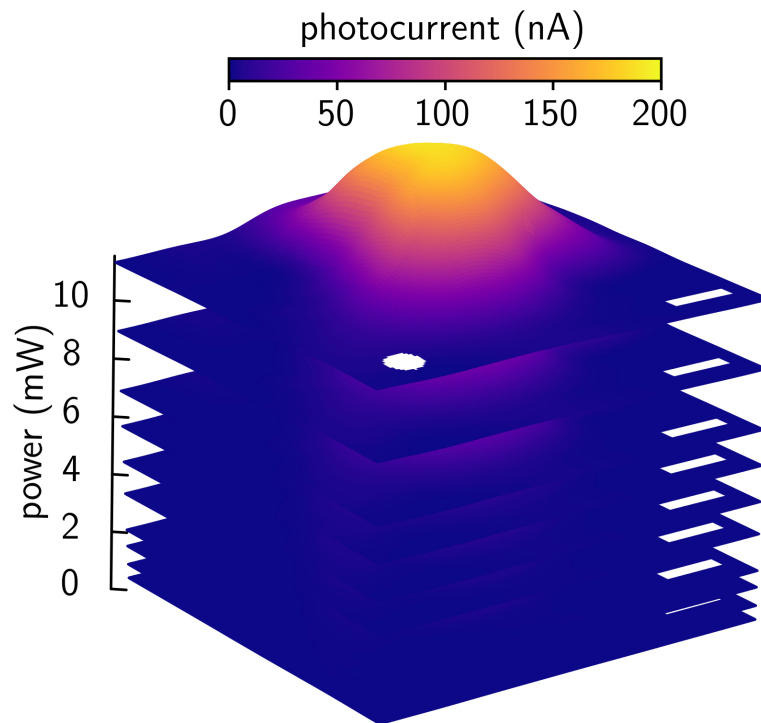


**Figure 6.1:** Spatial photocurrent maps for increasing laser power. Wavelength  $\lambda = 1200$  nm,  $T = 297$  K, and time delay  $\Delta t = 120$  ps. Scale bars  $3 \mu\text{m}$ . White circle indicates the full width at half maximum of the diffraction-limited beamspot.

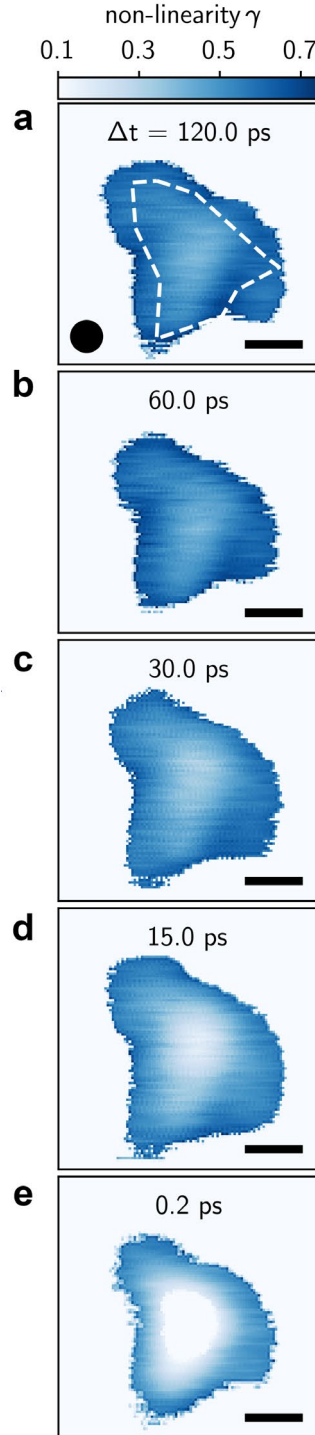


**Figure 6.2:** Spatial maps of nonlinearity  $\gamma(x, y)$  as a function of **(a-e)** two-pulse time delay  $\Delta t$  (labeled). Dashed line in **a** outlines the graphene-MoTe<sub>2</sub>-graphene heterostructure. Scale bars 3  $\mu\text{m}$ . Black circle indicates the full width at half maximum of the diffraction-limited beamspot. the ordinary MoTe<sub>2</sub> heterostructure photoresponse, which is dominated by 2-particle Auger recombination (Chapter 5).

To further investigate interacting charge carriers in this device, we produce a large set of photocurrent images (Figure 6.1) and fit the interlayer photocurrent vs. optical power to  $I \propto P^\gamma$  at each point in space. This large data set is condensed into an image of the photocurrent nonlinearity  $\gamma(x, y)$ , which we then measure as a function of  $\Delta t$ . A snapshot from the spatio-temporal dynamics at  $\Delta t = 120$  ps (Figure 6.2a) shows that the nonlinearity  $\gamma(x, y)$  is nearly uniform over the active area of the MoTe<sub>2</sub> heterostructure (dashed outline Figure 6.2a), exhibiting a narrow range  $\gamma = 0.45 - 0.60$ . The spatially uniform photoresponse with  $I \propto P^{1/2}$  at long time delay is fully consistent with ordinary photoresponse due to exciton-exciton interactions (Chapter 5).

Strikingly, when the time delay between laser pulses is very short, we observe highly anomalous photoresponse. At  $\Delta t = 0.2$  ps (Figure 6.2e), the power law behavior collapses near the center, resulting in a pronounced ring of sublinear photoresponse ( $\gamma \sim 0.5$ ). Figures 6.2b,c,d show that the sudden collapse near  $\Delta t = 0.2$  ps is preceded by a gradual suppression of  $\gamma$  at longer time delays. The area of power law suppression significantly exceeds the beam spot size, indicating a global change in photoresponse. This behavior is not a permanent change of device response. Instead, we observe  $\gamma$  suppression only at short time delay, while the ordinary photoresponse is recovered as soon as the laser intensity is reduced.

### 6.3 Critical Onset of Ring-Like Photoresponse

In the following, we examine the space-time evolution of the MoTe<sub>2</sub> photoresponse, and extract detailed dependence of the spatial photocurrent features on optical power, interlayer voltage, and time delay. We first decompose the spatial  $\gamma$  map measured at  $\Delta t = 0.2$  ps (Figure 6.2e) and examine the constituent photocurrent maps (Figure 6.3). At low optical powers, the photocurrent magnitude increases rapidly and monotonically (Figure 6.3a). For  $P > 5$  mW, however, the photocurrent at the center of the device suddenly decreases, forming a photocurrent ring of bright photoresponse. The photocurrent ring grows rapidly with increasing optical power. To see the ring expansion more clearly, Figure 6.3b shows the magnitude of the spatial gradient of the photocurrent maps  $|\nabla I|$ , which we use to visualize the local slope of the spatially resolved photocurrent landscape. At an optical power  $P = 5$  mW, a clear edge begins to emerge and grows into a well-formed ring.

Remarkably, the anomalous photocurrent ring appears abruptly with increasing optical power. Using the gradient maps (Figure 6.3b), we quantify the ring area by algorithmically identifying the contour  $|\nabla I| \approx 0$  (supplementary materials of Arp, Pleskot *et al.*<sup>33</sup>). Figure 6.3c shows the power dependence of the ring volume (product of area and sample thickness) as a fraction of the total heterostructure volume. At a critical power  $P_C = 5$  mW, we observe a nearly discontinuous growth rate of the volume fraction. Above

the transition  $P > P_C$ , the photocurrent ring, and thus volume fraction, expands linearly with optical power.

The sharp transition at  $P_C$  also manifests as a sudden deviation from power law behavior. Figure 6.3c lower right inset shows the spatially integrated photocurrent vs.

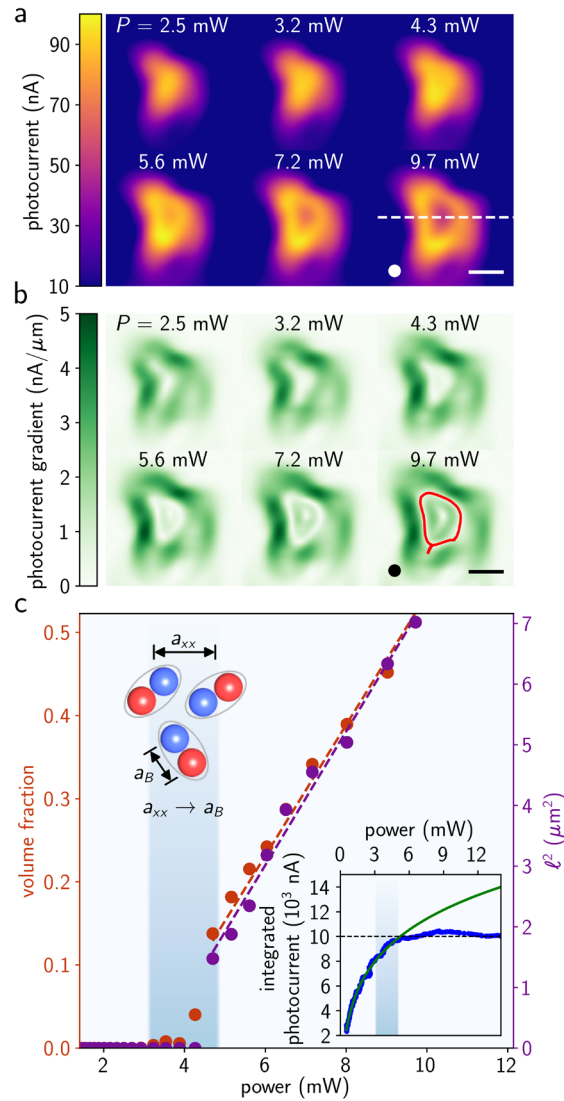


**Figure 6.3:** Critical onset of ring-like photoresponse revealed in analysis of spatial photocurrent maps. **(a)** Spatially resolved photocurrent measured at various powers (labeled) and  $\Delta t = 0.2$  ps. Dashed line indicates location of photocurrent line profiles. **(b)** Photocurrent gradient  $|\nabla I|$  calculated from photocurrent maps in **a**. The contour  $|\nabla I| \approx 0$  encloses the photocurrent ring (red contour in the image at  $P = 9.7$  mW). Scale bars 5

$\mu\text{m}$ , circles indicate the beamspot FWHM. (c) Photocurrent ring volume fraction (red data) vs. laser power. Volume fraction is the ratio of the volume enclosed by the  $|\nabla I| \approx 0$  contours to the active photocell volume (area). Peak-to-valley distance  $\ell$  (purple data) vs. optical power extracted from photocurrent line cuts in a. Red (purple) dashed lines are linear fits to volume fraction ( $\ell^2$ ) vs. optical power above  $P = 6$  mW. Inset top, inter-exciton spacing  $a_{\text{xx}}$  approaches the exciton Bohr radius  $a_B$ . Inset bottom, spatially integrated photocurrent vs. power (blue data) and power law fit below 6 mW (solid green line).

power measured along the dashed line in Figure 6.3a. The photocurrent increases rapidly at low power and exhibits ordinary power law growth (solid green line Fig. 6.3c lower right inset). Above  $P = P_C$ , however, the data falls significantly below the power law fit, and the spatially integrated photocurrent remains nearly constant as power increases.

Thus, the abrupt formation and expansion of the photocurrent ring corresponds directly to the collapse of power law behavior observed in Figure 6.2e. For  $\Delta t > 0.2$  ps the same behavior occurs at higher  $P_C$  (as shown in the supplementary materials of Arp, Pleskot *et al.*<sup>33</sup>) since the pulses become separated in time and the effect of each individual pulse is weaker than when they are combined.

#### **6.4 Model: 2D Electron-Hole Condensate**

We attribute the anomalous photoresponse at room temperature to a gas-to-liquid phase transition of  $e$ - $h$  pairs, reminiscent of similar phenomena observed at low temperatures in conventional semiconductors such as Si, Ge, GaAs, and CdS<sup>15,60,65</sup>. At low laser power, photo-excitation generates a gas of electrons and holes (Figure 6.4). Enhanced Coulomb interactions bind electrons and holes into excitons with nanometer-scale Bohr radius  $a_B$ <sup>15,17,60,65</sup>. The  $e$ - $h$  pair density increases with laser power until exciton-exciton interactions become comparable to interactions within an individual

bound  $e-h$  pair. Below the power threshold for the phase transition  $P_c$ , ordinary two-body exciton-exciton annihilation processes dominate the optoelectronic properties.

At the critical laser power  $P_c$ , the electron-hole population merges into a non-equilibrium many-body phase (Figure 6.4). The  $e-h$  pair density  $N$  becomes so large that the average spacing between pairs is nearly equal to the exciton radius (Fig. 6.3c upper

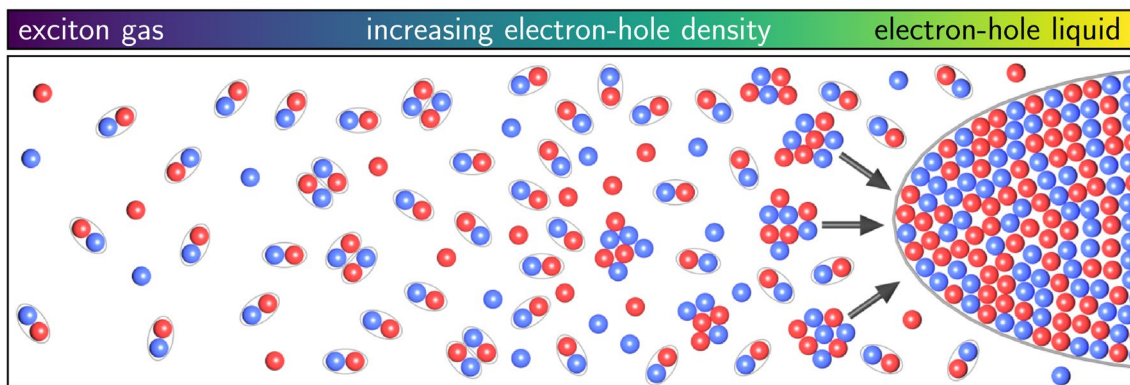


**Figure 6.4:** Evolution of electron-hole interactions with increasing  $e-h$  density. As density increases, the non-interacting gas of excitons gives rise to exciton-exciton interactions, eventually leading to condensation into a 2D electron-hole liquid.

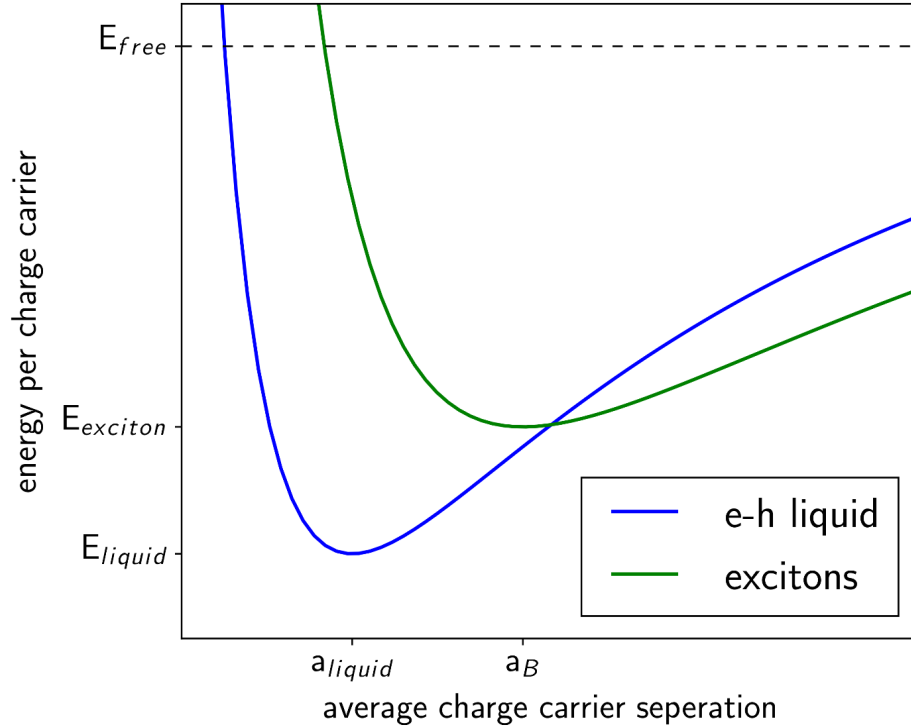


**Figure 6.5:** Schematic energy diagram for photoexcited carriers in MoTe<sub>2</sub> showing the energy curves for the *e-h* liquid and standard excitons.

left inset). As mentioned in Chapter 5, at  $P_C = 5$  mW, the mean exciton-exciton separation, which we estimate to be  $a_{xx} = 1-3$  nm in MoTe<sub>2</sub> (supplementary materials in Arp, Pleskot *et al.*<sup>33</sup>), is very close to the Bohr radius  $a_B = 2.3$  nm extracted from magneto-optical measurements<sup>61</sup>. Once  $a_{xx} \sim a_B$ , the *e-h* population reaches the critical density  $N_C \sim 0.5/nm^3$  *e-h* pairs. This density  $N_C$ , which is determined by the renormalized minimum energy per electron-hole pair (Figure 6.5), remains constant in the liquid phase. Above the phase transition, the renormalization of the energy per *e-h* pair results in a suppression of photon absorption within the *e-h* liquid<sup>13,68</sup>.

### 6.5 Evidence for the 2D Condensate

We confirm the  $e-h$  liquid by showing that it exhibits a fixed electron-hole pair density  $N_C$ , is highly polarizable in an applied electric field, and forms a sharp, stable boundary that separates it from the gas phase<sup>15,17,65</sup>. First, the liquid phase is characterized by highly unusual ring-like interlayer photoresponse, which results from fast interlayer transit of liberated electrons and holes near the edge of the droplet. At the surface of the photocell device, the excitation laser forms a diffraction-limited Gaussian beam spot with a full width at half maximum of 1.67 microns. When the local maximum power of the Gaussian beam exceeds the critical power threshold  $P_C$ , an electron-hole liquid droplet forms near the center of the beam spot. The observed photocurrent results from electrons and holes at the edges of the electron-hole liquid. The characteristic ring shape then arises from the convolution of the beam spot with a sharply bound region of suppressed absorption. Figure 6.6 compares the  $e-h$  liquid model to interlayer photocurrent line traces as a function of increasing power (measured along the dashed

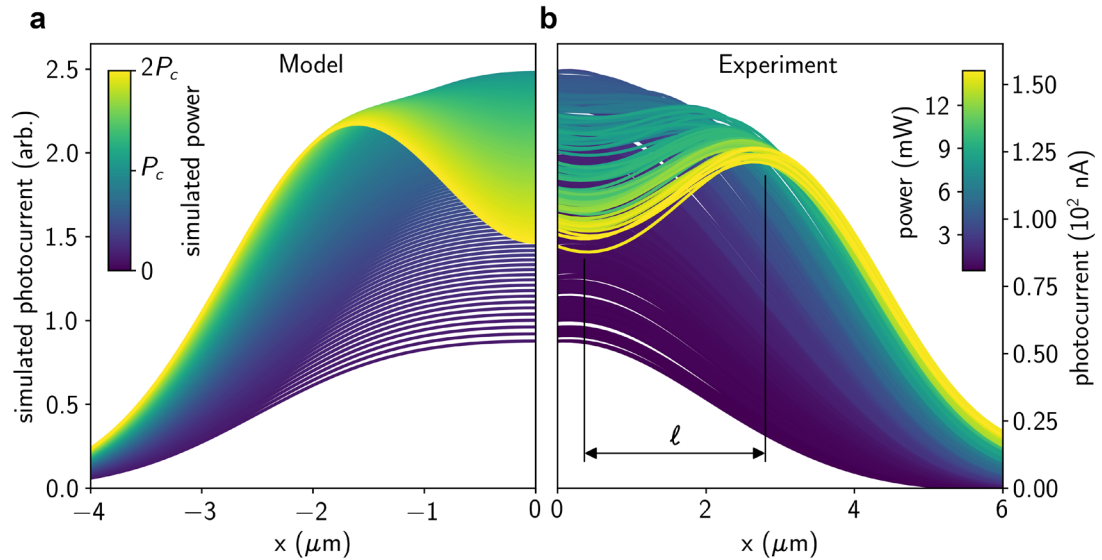


**Figure 6.6:** Room temperature 2D electron-hole liquid and comparison to spatial photocurrent imaging in the MoTe<sub>2</sub> photocells. **(a)** Calculated spatially resolved photoresponse of the electron-hole condensate showing the suppression of photocurrent in the center of the sample above the critical power  $P_C$ . **(b)** Photocurrent line profiles measured across the center of the sample for increasing power;  $T = 297$  K,  $\Delta t = 0.2$  ps.

line in Figure 6.3a). The  $e$ - $h$  liquid model (Figure 6.6a) shows excellent agreement with the photocurrent line profiles, indicating that the interlayer photocurrent is suppressed in the region of the anomalous phase.

Once the critical density  $N_C$  is reached, energy added to the  $e$ - $h$  liquid contributes exclusively to expansion. To see this, we first extract the squared center-to-edge distance of the photocurrent ring  $\ell^2$  from the photocurrent profiles of the photocurrent images shown in Figure 6.3a, and plot  $\ell^2$  vs. power in Figure 6.3c. As expected from the linear growth of the 2D volume,  $\ell^2$  increases linearly above the critical threshold (purple data in Figure 6.3c), exhibiting nearly identical growth to the volume fraction. From the data, we conclude that the state leading to suppressed photoresponse exhibits a well-defined volume that is highly localized, which increases as the number of electron-hole pairs (proportional to the photon fluence) increases. We thus deduce that, similar to a conventional incompressible liquid, the condensate density  $N_C$  remains fixed, and thus linear increase of  $e$ - $h$  pair density yields corresponding linear increase in liquid volume.

The electron-hole liquid phase can be dissociated with small interlayer voltage. Figure 6.7a shows spatial photocurrent line cuts as a function of voltage, where the side

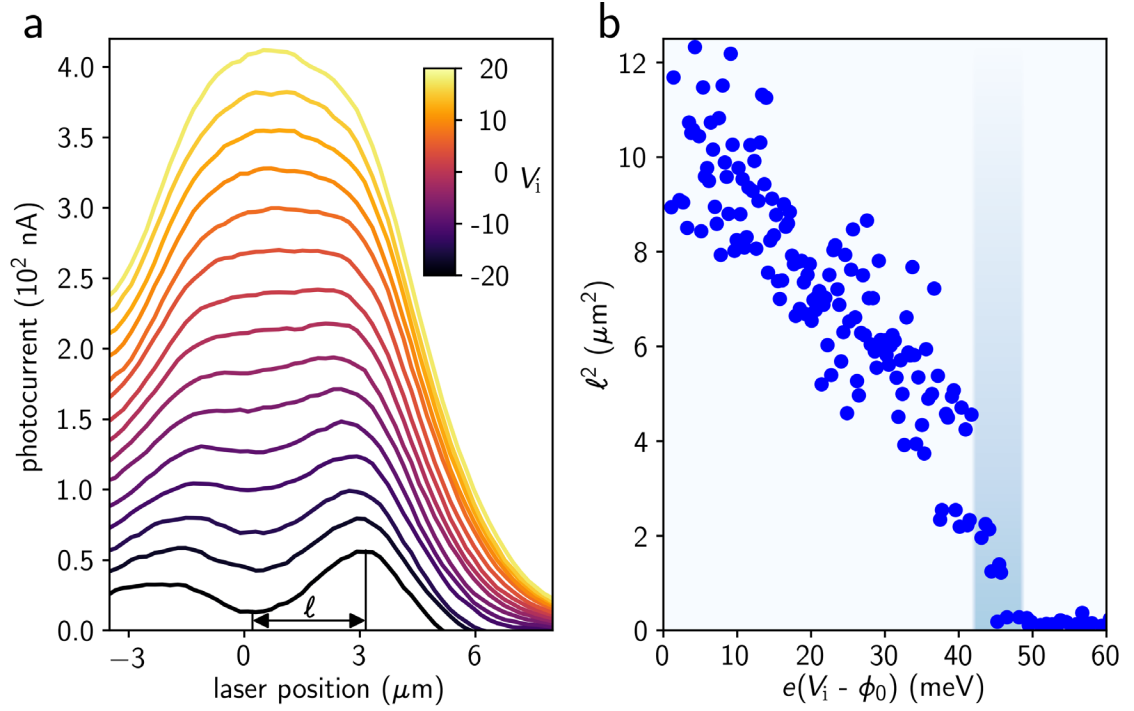


**Figure 6.7:** Interlayer voltage dependence of the 2D electron-hole liquid. **(a)** Spatial line cuts of the photocurrent as a function of interlayer voltage  $V_i$ ;  $\Delta t = 0.2$  ps. **(b)** Photocurrent ring peak-to-valley distance  $\ell^2$  vs. interlayer voltage.  $\phi_0$  is the built-in potential of the graphene-MoTe<sub>2</sub>-graphene photocell.

of the  $e$ - $h$  liquid droplet can be tracked via the center-to-edge distance  $\ell$ . For interlayer voltages  $V_i$  above the built-in potential  $\phi_0 = -41$  mV (supplementary materials in Arp, Pleskot *et al.*<sup>33</sup>),  $\ell^2$  decreases approximately linearly as voltage increases (Figure 6.7b). When the total interlayer voltage exceeds the critical voltage  $eV_C = e(V_i - \phi_0) > 45$  meV, electrons and holes become ordinary  $e$ - $h$  pairs. Above the critical interlayer voltage  $V_C$ , spatially uniform photocurrent re-emerges as the 2D liquid dissociates in the electric field.

Though a single pulse at high enough power could form the  $e$ - $h$  liquid, two-pulse measurements can also reveal the rich dynamic transition between the electron-hole

liquid and gas phases. Figure 6.8a,b shows the time-resolved photocurrent and photocurrent nonlinearity  $\gamma$ , similar to Figure 5.2 in Chapter 5 but including power values greater than  $P_C$  to reveal the behavior of the  $e$ - $h$  liquid. When the laser is fixed at the center of the device, the photocurrent vs.  $\Delta t$  exhibits remarkably different power dependence between short and long time delay. At short  $\Delta t$ , the photocurrent at the center of the device decreases with increasing power above  $P_C$  (supplementary materials in Arp, Pleskot *et al.*<sup>33</sup>). This extreme sublinear photoresponse is fully consistent with power law collapse associated with the liquid phase onset (Figure 6.3c lower right inset). At long time delay, the photocurrent exhibits ordinary behavior  $I \propto P^{1/2}$ , described in detail in Chapter 5 (Figure 6.8b). We fit  $\gamma$  vs.  $\Delta t$  to an exponential decay (black line Figure 6.8b) to extract the charge density persistence time  $\tau = 22$  ps.

Also, as shown in Figure 5.4e in Chapter 5, below the 5 mW threshold the data is fully consistent with the subcritical exciton-exciton annihilation model as a function of power and  $\Delta t$ . At and above the 5 mW threshold, for  $\Delta t > \tau$  the pulses are independent and each is insufficient to drive the phase transition producing only a gas of ordinary  $e$ - $h$  pairs. For  $\Delta t < \tau$  the combined charge density produced by the two pulses is sufficient to

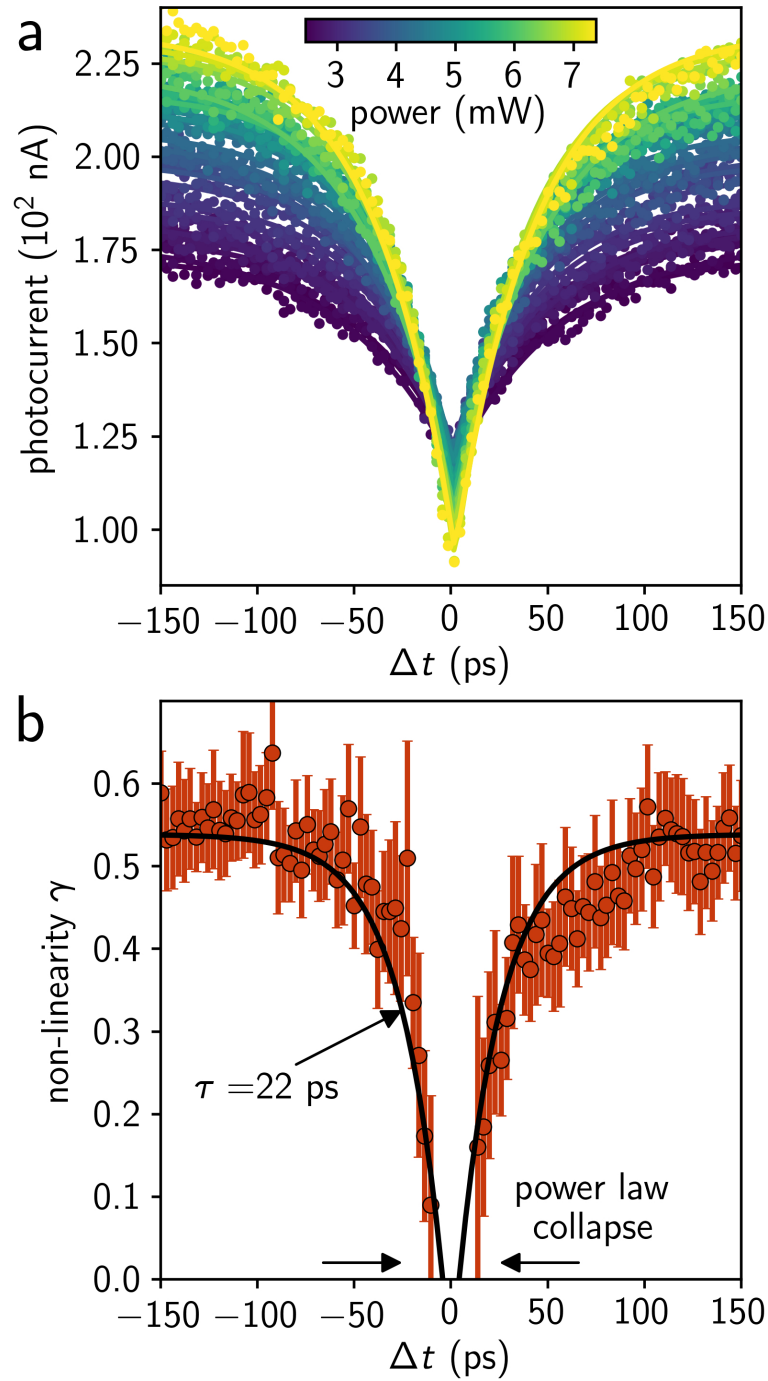


**Figure 6.8:** Dynamic photoresponse of the 2D electron-hole liquid. **(a)** Photocurrent vs.  $\Delta t$  for increasing optical power. The laser is fixed at the center of the device. Solid lines are exponential fits to the data at each power. **(b)** Power law exponent  $\gamma$  as a function of  $\Delta t$ , extracted by fitting the data in **a** to  $I \propto P^\gamma$ . Solid black line is an exponential fit with a characteristic time-scale  $\tau = 22$  ps.

cause the gas-to-liquid transition (see supplementary materials in Arp, Pleskot *et al.*<sup>33</sup>) causing a suppression of the photocurrent relative to the subcritical model (Figure 5.4e).

## 6.6 Conclusion

In this chapter we demonstrated that in quasi-2D TMDs, the large binding energy and strong Coulomb interactions combine to allow for an exotic  $e$ - $h$  liquid phase diagram at room temperature<sup>60</sup>, suggesting new device applications that harness electronic fluids at room temperature. The gas-to-liquid phase transition is set by the energy difference  $\Delta E$  between the average energy per  $e$ - $h$  pair in the gas phase and the reduced energy per  $e$ - $h$  pair in the liquid phase<sup>60</sup> (supplementary materials in Arp, Pleskot *et al.*<sup>33</sup>). When  $\Delta E$  is large compared to thermal energy at room temperature ( $K_B T_{300K} = 26$  meV), the liquid is stable against thermal fluctuations. From the interlayer voltage dependence (Figure 6.7a), we estimate that  $\Delta E \sim eV_C \sim 45$  meV, approximately twice the thermal energy at room temperature. While this renormalization is comparable to conventional 2D electron systems, the  $e$ - $h$  pair binding energy ( $\sim 10^2$  meV) in TMDs is several orders of magnitude larger<sup>2,13,68,69</sup>. Electrons and holes in the liquid phase move independently from another within the confined liquid volume, yet they are not able to escape without sufficient excess energy. Such stable collective excitations, potentially exhibiting very high mobility, could have applications in very high-power, high frequency Terahertz sources and detectors that can be manipulated with both electronic and optical control.

## CHAPTER 7

### CONCLUSION

In this dissertation, we presented a novel 2D optoelectronic device capable of revealing striking new forms of charge carrier interactions at room temperature. We fabricated graphene-MoTe<sub>2</sub>-graphene heterostructures and measured the interlayer photocurrent using an ultrafast pulsed laser system (Chapter 3). By performing basic material and optoelectronic characterization measurements, we gained a thorough understanding of the device performance and confirmed that our devices are of high quality (Chapter 4). We then probed the interlayer photocurrent as a function of numerous experimental parameters, and discovered that charge carriers in the device are sufficiently dense even at low incident laser power for the photoresponse to be dominated by 2-particle Auger recombination (Chapter 5). As we pushed the system to higher power, we induced a phase change from an electron-hole gas phase to a highly interacting electron-hole liquid droplet phase (Chapter 6). By examining the dynamics of the system, we found that 2-particle Auger recombination, an exciton-exciton annihilation process, precedes the formation of the liquid phase in TMDs. The work of this dissertation demonstrates the creation of highly interacting charge carriers stable at room temperature and achieved through moderate operating conditions, opening wide the door for additional research to further understand the properties of such systems as well as novel applications to harness their potential.

## REFERENCES

1. T. Edvinsson, Optical quantum confinement and photocatalytic properties in two-, one- and zero-dimensional nanostructures. *Royal Society Open Science* **5**, 180387 (2018).
2. A. Chernikov, T. C. Berkelbach, H. M. Hill, A. Rigosi, Y. Li, O. B. Aslan, D. R. Reichman, M. S. Hybertsen, T. F. Heinz, Exciton binding energy and nonhydrogenic rydberg series in monolayer WS<sub>2</sub>. *Phys. Rev. Lett.* **113**, 076802 (2014).
3. L. V. Keldysh, Coulomb interaction in thin semiconductor and semimetal films. *Soviet Journal of Experimental and Theoretical Physics Letters* **29**, 658 (1979).
4. A. Splendiani, L. Sun, Y. Zhang, T. Li, J. Kim, C. Y. Chim, G. Galli, F. Wang, Emerging photoluminescence in monolayer MoS<sub>2</sub>. *Nano Letters* **10**, 1271-1275 (2010).
5. M. Massicotte, P. Schmidt, F. Violla, K. G. Schidler, A. Reserbat-Plantey, K. Watanabe, T. Taniguchi, K. J. Tielrooij, F. H. L. Koppens, Picosecond photoresponse in van der Waals heterostructures. *Nature Nanotechnology* **11**, 42-46 (2016).
6. D. Sun, Y. Rao, G. A. Reider, G. Chen, Y. You, L. Brézin, A. R. Harutyunyan, T. F. Heinz, Observation of rapid exciton–exciton annihilation in monolayer molybdenum disulfide. *Nano Lett.* **14**, 5625-5629 (2014).
7. G. Froehlicher, E. Lorchat, S. Berciaud, Direct versus indirect band gap emission and exciton-exciton annihilation in atomically thin molybdenum ditelluride MoTe<sub>2</sub>. *Phys. Rev. B* **94**, 085429 (2016).
8. S. Mouri, Y. Miyauchi, M. Toh, W. Zhao, G. Eda, K. Matsuda, Nonlinear photoluminescence in atomically thin layered WSe<sub>2</sub> arising from diffusion-assisted exciton-exciton annihilation. *Phys. Rev. B* **90**, 155449 (2014).
9. N. Kumar, Q. Cui, F. Ceballos, D. He, Y. Wang, H. Zhao, Exciton-exciton annihilation in MoSe<sub>2</sub> monolayers. *Phys. Rev. B* **89**, 125427 (2014).
10. Y. Yu, Y. Yu, C. Xu, A. Barrette, K. Gundogdu, L. Cao, Fundamental limits of exciton-exciton annihilation for light emission in transition metal dichalcogenide monolayers. *Phys. Rev. B* **93**, 201111 (2016).
11. A. Surrente, A. A. Mitioglu, K. Galkowski, L. Klotkowski, W. Tabis, B. Vignolle, D. K. Maude, P. Plochocka, Onset of exciton-exciton annihilation in single-layer black phosphorus. *Phys. Rev. B* **94**, 075425 (2016).

12. M. Kulig, J. Zipfel, P. Nagler, S. Blanter, C. Schüller, T. Korn, N. Paradiso, M. M. Glazov, A. Chernikov, Exciton diffusion and halo effects in monolayer semiconductors. *Physical Review Letters* **120**, 207401 (2018).
13. A. Chernikov, C. Ruppert, H. M. Hill, A. F. Rigosi, T. F. Heinz, Population inversion and giant bandgap renormalization in atomically thin WS<sub>2</sub> layers. *Nature Photonics* **9**, 466-470 (2015).
14. G. Aivazian, H. Yu, S. Wu, J. Yan, D. G. Mandrus, D. Cobden, W. Yao, X. Xu, Many-body effects in nonlinear optical responses of 2D layered semiconductors. *2D Materials* **4**, 025024 (2017).
15. C. D. Jeffries, Electron-hole condensation in semiconductors. *Science* **189**, 955-964 (1975).
16. V. M. Asnine, A. A. Rogachev, S. M. Ryvkin, Transition to metallic conduction at high exciton concentrations. *Sov. Phys. Semicond.* **1**, 1447 (1968).
17. L. V. Keldysh, in *Proceedings of the 9<sup>th</sup> International Conference on Physics of Semiconductors*, (Nauka Leningrad, 1968) 1303.
18. T. K. Lo, Spectroscopic determination of condensation energy and density of electron-hole droplets in pure Ge. *Solid State Commun.* **15**, 1231 (1974).
19. M. Kan, J. Y. Wang, X. W. Li, S. H. Zhang, Y. W. Li, Y. Kawazoe, Q. Sun, P. Jena, Structures and phase transition of a MoS<sub>2</sub> monolayer. *J. Phys. Chem. C* **118**, 1515-1522 (2014).
20. M. Yamamoto, S. T. Wang, M. Ni, Y. F. Lin, S. L. Li, S. Aikawa, W. B. Jian, K. Ueno, K. Wakabayashi, K. Tsukagoshi, Strong enhancement of Raman scattering from a bulk-inactive vibrational mode in few-layer MoTe<sub>2</sub>. *ACS Nano* **8**, 3895–3903 (2014).
21. Y. Zhang, T. R. Chang, B. Zhou, Y. T. Cui, H. Yan, Z. Liu, F. Schmitt, J. Lee, R. Moore, Y. Chen, H. Lin, H. T. Jeng, S. K. Mo, Z. Hussain, A. Bansil, Z. X. Shen, Direct observation of the transition from indirect to direct bandgap in atomically thin epitaxial MoSe<sub>2</sub>. *Nat. Nanotechnology* **9**, 111–115 (2014).
22. C. Ruppert, O. B. Aslan, T. F. Heinz, Optical properties and band gap of single and few-layer MoTe<sub>2</sub> crystals. *Nano Letters* **14**, 6231-6236 (2014).
23. T. Boker, R. Severin, A. Müller, C. Janowitz, R. Manzke, D. Voß, P. Krüger, A. Mazur, J. Pollmann, Band structure of MoS<sub>2</sub>, MoSe<sub>2</sub>, and  $\alpha$ -MoTe<sub>2</sub>: angle-resolved

- photoelectron spectroscopy and ab initio calculations. *Physical Review B* **64**, 235305 (2001).
24. K. F. Mak, K. He, C. Lee, G. H. Lee, J. Hone, T. F. Heinz, J. Shan, Tightly bound trions in monolayer MoS<sub>2</sub>. *Nature Materials* **12**, 207–211 (2013).
  25. A. K. Geim, I. V. Grigorieva, Van der Waals heterostructures. *Nature* **499**, 419-425 (2013).
  26. P. J. Zomer, S. P. Dash, N. Tombros, B. J. van Wees, A transfer technique for high mobility graphene devices on commercially available hexagonal boron nitride. *Appl. Phys. Lett.* **99**, 232104 (2011).
  27. S. J. Haigh, A. Gholinia, R. Jalil, S. Romani, L. Britnell, D. C. Elias, K. S. Novoselov, L. A. Ponomarenko, A. K. Geim, R. Gorbachev, Cross-sectional imaging of individual layers and buried interfaces of graphene-based heterostructures and superlattices. *Nature Mater.* **11**, 764–767 (2012).
  28. P. Steinleitner, P. Merkl, A. Graf, P. Nagler, K. Watanabe, T. Taniguchi, J. Zipfel, C. Schüller, T. Korn, A. Chernikov, S. Brem, M. Selig, G. Berghauser, E. Malic, Rupert Huber, Dielectric engineering of electronic correlations in a van der Waals heterostructure. *Nano Letters* **18**, 1402-1409 (2018).
  29. K. Zhang, X. Fang, Y. Wang, Y. Wan, Q. Song, W. Zhai, Y. Li, G. Ran, Y. Ye, L. Dai, Ultrasensitive near-infrared photodetectors based on a graphene-MoTe<sub>2</sub>-graphene vertical van der Waals heterostructure. *ACS Applied Materials and Interfaces* **9**, 5392-5398 (2017).
  30. K. S. Novoselov, A. K. Geim, S. V. Morozov, D. Jiang, Y. Zhang, S. V. Dubonos, I. V. Grigorieva, A. A. Firsov, Electric field effect in atomically thin carbon films. *Science* **306**, 666-669 (2004).
  31. S. B. Desai, S. R. Madhvapathy, M. Amani, D. Kiriya, M. Hettick, M. Tosun, Y. Zhou, M. Dubey, J. W. Ager III, D. Chrzan, A. Javey, Gold-mediated exfoliation of ultralarge optoelectronically-perfect monolayers. *Advanced Materials* **28**, 4053-4058 (2016).
  32. A. Castellanos-Gomez, M. Buscema, R. Molenaar, V. Singh, L. Janssen, H. S. J. van der Zant, G. A. Steele, Deterministic transfer of two-dimensional materials by all-dry viscoelastic stamping. *2D Mater. Lett.* **1**, 1-8 (2014).
  33. T. B. Arp, D. Pleskot, V. Aji, N. M. Gabor, Electron-hole liquid in a van der Waals heterostructure photocell at room temperature. *Nature Photonics* advanced online publication 04 02 2019 (DOI 10.1038/s41566-019-0349-y).

34. A. C. Ferrari, J. C. Meyer, V. Scardaci, C. Casiraghi, M. Lazzeri, F. Mauri, S. Piscanec, D. Jiang, K. S. Novoselov, S. Roth, A. K. Geim, Raman spectrum of graphene and graphene layers. *Phy. Rev. Lett.* **97**, 187401 (2006).
35. O. P. Agnihotri, H. K. Sehgal, A. K. Garg, Laser excited Raman spectra of gr. VI semiconducting compounds. *Solid State Commun.* **12**, 135-138 (1973).
36. G. Cunningham, M. Lotya, C. S. Cucinotta, S. Sanvito, S. D. Bergin, R. Menzel, M. S. P. Shaffer, J. N. Coleman, Solvent exfoliation of transition metal dichalcogenides: dispersibility of exfoliated nanosheets varies only weakly between compounds. *ACS Nano* **6**, 3468-3480 (2012).
37. N. R. Pradhan, D. Rhodes, S. Feng, Y. Xin, S. Memaran, B. Moon, H. Terrones, M. Terrones, L. Balicas, Field-effect transistors based on few-layered  $\alpha$ -MoTe<sub>2</sub>. *ACS Nano* **8**, 5911-5920 (2014).
38. M. Kuri, B. Chakraborty, A. Paul, S. Das, A. K. Sood, A. Das, Enhancing photoresponsivity using MoTe<sub>2</sub>-graphene vertical heterostructures. *Appl. Phys. Lett.* **108**, 063506 (2016).
39. W. J. Yu, Y. Liu, H. Zhou, A. Yin, Z. Li, Y. Huang, X. Duan, Highly efficient gate-tunable photocurrent generation in vertical heterostructures of layered materials. *Nature Nanotechnology* **8**, 952-958 (2013).
40. Y. Lin, Y. Xu, S. Wang, S. Li, M. Yamamoto, A. Aparecido-Ferreira, W. Li, H. Sun, S. Nakaharai, W. Jian, K. Ueno, K. Tsukagoshi, Ambipolar MoTe<sub>2</sub> transistors and their applications in logic circuits. *Advanced Materials* **26**, 3263-3269 (2014).
41. T. J. Octon, V. K. Nagareddy, S. Russo, M. F. Craciun, C. D. Wright, Fast high-responsivity few-layer MoTe<sub>2</sub> photodetectors. *Advanced Optical Materials* **4**, 1750-1754 (2016).
42. G. P. Kekelidzet, B. L. Evans, The photovoltage in single crystals of  $\alpha$ -MoTe<sub>2</sub>. *Brit. J. Appl. Phys.* **2**, 855-861 (1969).
43. M. Sze, K. K. Ng, *Physics of Semiconductor Devices*. (Wiley-Interscience publications, United States, 1963).
44. P. Landsberg, *Recombination in Semiconductors*. (Cambridge University Press, Cambridge, 1991).

45. D. I. Chepic, A. L. Efros, A. I. Ekimov, M. G. Ivanov, V. A. Kharchenko, I. A. Kudriavtsev, T. V. Yazeva, Auger ionization of semiconductor quantum dots in a glass matrix. *J. Lumin.* **47**, 113 (1990).
46. Y. Z. Hu, S. W. Koch, M. Linderg, N. Peyghambarian, E. L. Pollock, F. F. Abraham, Biexcitons in semiconducting quantum dots. *Physical Review Letters* **64**, 1805-1807 (1990).
47. R. T. Phillips, D. J. Lovering, G. J. Denton, Biexciton creation and recombination in a GaAs quantum well. *Phys. Rev. B* **45**, 4308-4311 (1992).
48. J. C. Kim, D. R. Wake, J. P. Wolfe, Thermodynamics of biexcitons in a GaAs quantum well. *Phy. Rev. B* **50**, 15099-15107 (1994).
49. L. Colombier, J. Selles, E. Rousseau, J. S. Lauret, F. Vialla, C. Voisin, G. Cassabois, Detection of a biexciton in semiconducting carbon nanotubes using nonlinear optical spectroscopy. *Physical Review Letters* **109**, 197402 (2012).
50. B. Yuma, S. Berciaud, J. Besbas, J. Shaver, S. Santos, S. Ghosh, R. B. Weisman, L. Cagnet, M. Gallart, M. Ziegler, B. Hönerlage, B. Lounis, P. Gilliot, Biexciton, single carrier, and trion generation dynamics in single-walled carbon nanotubes. *Phys. Rev. B* **87**, 205412 (2013).
51. F. Thouin, S. Neutzner, D. Cortecchia, V. A. Dragomir, C. Soci, T. Salim, Y. M. Lam, R. Leonelli, A. Petrozza, A. R. S. Kandada, C. Silva, Stable biexcitons in two-dimensional metal-halide perovskites with strong dynamic lattice disorder. *Phys. Rev. Mat.* **2**, 034001 (2018).
52. Y. You, X. X. Zhang, T. C. Berkelbach, M. S. Hybertsen, D. R. Reichman, T. F. Heinz, Observation of biexcitons in monolayer WSe<sub>2</sub>. *Nature Physics* **11**, 477-482 (2015).
53. K. Hao, J. F. Specht, P. Nagler, L. Xu, K. Tran, A. Singh, C. K. Dass, C. Schüller, T. Korn, M. Richter, A. Knorr, X. Li, G. Moody, Neutral and charged inter-valley biexcitons in monolayer MoSe<sub>2</sub>. *Nature Communications* **8**, 15552 (2017).
54. V. D. Kulakovskii, V. S. Timofeev, Biexcitons in the emission spectrum of uniaxially deformed silicon. *JETP* **25**, 487-491 (1977).
55. M. L. W. Thewalt, W. G. McMullan, Green and near-infrared luminescence due to the biexcitons in unperturbed silicon. *Phys. Rev. B* **30**, 6232-6234 (1984).

56. M. L. W. Thewalt, J. A. Rostworowski, Biexcitons in Si. *Solid State Communications* **25**, 991-993 (1978).
57. V. M. Asnin, B. V. Zurov, T. M. Murina, A. M. Prokhorov, A. A. Rogachev, N. I. Salina, Radiative recombination of biexcitons in Germanium. *JETP* **62**, 735-745 (1972).
58. L. Yuan, T. Wang, T. Zhu, M. Zhou, L. Huang, Exciton dynamics, transport, and annihilation in atomically thin two-dimensional semiconductors. *J. Phys. Chem. Lett.* **8**, 3371-3379 (2017).
59. W. J. Yu, Q. A. Yu, H. Oh, H. G. Nam, H. Zhou, S. Cha, J. Y. Kim, A. Carvalho, M. Jeong, H. Choi, A. H. C. Neto, Y. H. Lee, X. Duan, Unusually efficient photocurrent extraction in monolayer van der Waals heterostructure by tunneling through discretized barriers. *Nature Communications* **7**, 13278 (2016).
60. A. Rustagi, A. F. Kemper, Theoretical phase diagram for the room-temperature electron-hole liquid in photoexcited quasi-two-dimensional monolayer MoS<sub>2</sub>. *Nano Letters* **18**, 455-459 (2017).
61. Y. Sun, J. Zhang, Z. Ma, C. Chen, J. Han, F. Chen, X. Luo, Y. Sun, Z. Sheng, The Zeeman splitting of bulk 2H-MoTe<sub>2</sub> single crystal in high magnetic field. *Appl. Phys. Lett.* **110**, 102102 (2017).
62. M. A. Lampert, Mobile and immobile effective-mass-particle complexes in nonmetallic solids. *Phys. Rev. Lett.* **1**, 450-453 (1958).
63. K. Kheng, R. Cox, M. D'Aubigné, Observation of negatively charged excitons X<sup>-</sup> in semiconductor quantum wells. *Phys. Rev. Lett.* **71**, 1752-1755 (1993).
64. G. D. Scholes, G. Rumbles, Excitons in nanoscale systems. *Nat. Mater.* **5**, 683-696 (2006).
65. L. V. Keldysh, The electron-hole liquid in semiconductors. *Contemp. Phys.* **27**, 395-428 (1986).
66. R. A. Kaindl, M. A. Carnahan, D. Hägele, R. Lövenich, D. S. Chemla, Ultrafast terahertz probes of transient conducting and insulating phases in an electron-hole gas. *Nature* **423**, 734-738 (2003).
67. A. E. Almand-Hunter, H. Li, S. T. Cundiff, M. Mootz, M. Kira, S. W. Koch, Quantum droplets of electrons and holes. *Nature* **506**, 471-475 (2014).

68. M. M. Ugeda, A. J. Bradley, S. Shi, F. H. da Jornada, Y. Zhang, D. Y. Qiu, W. Ruan, S. Mo, Z. Hussain, Z. Shen, F. Wang, S. G. Louie, M. F. Crommie, Giant bandgap renormalization and excitonic effects in a monolayer transition metal dichalcogenide semiconductor. *Nature Materials* **13**, 1091-1095 (2014).
69. A. Arora, R. Schmidt, R. Schneider, M. R. Molas, I. Breslavetz, M. Potemski, R. Bratschitsch, Valley Zeeman splitting and valley polarization of neutral and charged excitons in monolayer MoTe<sub>2</sub> at high magnetic fields. *Nano Letters* **16**, 3624–3629 (2016).